博 士 学 位 論 文

Doctoral Thesis

論文題目

Thesis Title

軟磁性センダスト合金薄膜の開発と
それを電極としたトンネル磁気抵抗効果に関する研究

Development of Sendust Film with Soft Magnetic Property
and Tunnel Magnetoresistance Effect Using its Electrode

東北大学大学院工学研究科

Graduate School of Engineering,

TOHOKU UNIVERSITY

専攻/Department： 応用物理学専攻

学籍番号/ ID No： C1TD3001

氏 名 /Ｎａｍｅ： 赤松 昇馬

OUTLINE

I. Introduction....4
1. Spintronics....4
2. TMR effect....5
3. MTJ using crystalized (001)-MgO barrier....6
4. Magnetic sensor....9
5. TMR sensor....10
6. MEG detection and TMR sensor....12
7. Conventional approach to improve the performance of TMR sensor....16
① MTJ Structure Using NiFe Free Layer....16
② MTJ Structure Using CoFeSiB Free Layer....17
③ MTJ Structure Using Heusler Alloy Free Layer....18
8. Approach of This Study....22
① Sendust alloy....22
② The Origin of Soft Magnetism in Sendust....23
③ Potential of Sendust as a Novel Free Layer Material....23
9. Purpose in this study....27
II. Experimental methods....28
1. Film fabrication....28
2. Micro-fabrication process....30
① Photolithography....30
② Ar Ion Milling....32
③ Interlayer Insulating Film Deposition....32
④ Contact Hole Formation....32
⑤ Top Electrode Formation....32
3. Annealing process....35
4. X-ray diffraction – XRD....36
5. Atomic force microscope – AFM....37
6. Vibrating sample magnetometer – VSM....38
7. Ferromagnetic resonance – FMR....39
8. Optical lever method....40
9. Magneto-optic Kerr effect – MOKE....41
10. Brillouin Light Scattering – BLS....41
11. Four probe method....42
12. Physical Properties Measurement System – PPMS....42

III. Magnetic property of FeAlSi film 43
1. Sample preparation 43
2. Structural analysis 44
① Crystal structure 44
② Surface structure 48
3. Static magnetic property 50
① Magnetization curve 50
② Magnetic anisotropy by FMR 53
③ Magnetostriction 54
4. Discussion of soft magnetic property 57
① The origin of soft magnetic property 57
② Magnetic domain by MOKE 62
5. Dynamic magnetic property – Exchange stiffness constant by BLS 64
6. Short summary 69
IV. Magnetoresistance property of MTJ using FeAlSi electrode 70
1. Sample preparation 70
2. Tunnel magnetoresistance property 71
① TMR ratio and RA 71
② Exchange coupling in pinned layer 74
3. Discussion of TMR property 76
① Oxidation of FeAlSi/MgO interface 76
② Temperature dependence 77
③ Bias voltage dependence of TMR ratio and R_{AP} 79
④ Bias voltage dependence of R_P 82
⑤ Tunnel anisotropic magnetoresistance property 84
4. Short summary 86
V. Summary 87
VI. Publications & Talks 89
VII. References 91
VIII. Acknowledgement – 謝辞 100

I. Introduction

1. Spintronics

Electrons possess two degrees of freedom: charge and spin. While conventional electronics have utilized only the information of charge, in recent decades, the field of "spintronics", which develops devices with new functions by controlling the information of spin, has been actively researched[1]. The concept of spintronics developed from research on the magnetic resistance (MR) effect in metallic artificial lattices using magnetic materials. MR effect refers to the phenomenon where the electrical resistance of a material changes due to an external magnetic field. The MR effect is classified into several types.

In spintronics, particularly important research on MR effects dates back to the discovery of anisotropic magnetoresistance (AMR) by W. Thomson in 1857[2]. The AMR effect is a phenomenon where the electrical resistance of a ferromagnetic thin film changes depending on the relative angle between the direction of magnetization and the direction of the electric current flowing through the film. This can be explained by considering the effects of spin-orbit interaction in the two-current model[3]. Although the change in electrical resistance due to the AMR effect is at most about 3% at room temperature[4], it has been applied to magnetic sensors (AMR sensor), including the early read magnetic heads for HDDs.

Following this, the giant magnetoresistance (GMR) effect was independently discovered in 1988 by the groups of A. Fert and P. Grünberg[5,6]. Both A. Fert and P. Grünberg were awarded the Nobel Prize in Physics in 2007 for their discovery of the GMR effect. The GMR effect occurs in metallic artificial lattices of ferromagnetic/non-magnetic/ferromagnetic layers, where the electrical resistance changes depending on the relative angle of magnetization of each ferromagnetic layer when an electric current is passed in-plane or perpendicular to the film. This effect is attributed to spin-dependent scattering, where the potential experienced by electrons moving through the artificial lattice varies depending on the spin orientation. The GMR effect is named after following: the change in electrical resistance due to the GMR effect is "giant" compared to the AMR effect, ranging from several percent to several tens of percent at room temperature. This significant change in resistance enabled the creation of more advanced devices than before. For example, read magnetic heads for HDDs were transitioned from those based on the AMR effect to those based on the GMR effect, which is called GMR sensor.

And in recent years, the most highlighted phenomenon among the various MR effects is the tunnel magnetoresistance (TMR) effect.

2. TMR effect

Magnetic Tunnel Junction (MTJ) is the element consisting of three film layers: Ferromagnetic layer (FM1) / Insulator (I) / Ferromagnetic layer (FM2), where all layers are nm-order films. If bias voltage (V_{Bias}) is applied along out-of-plane direction, electrons tunnel from FM1 to FM2 with the "Tunnel effect", which is a famous phenomenon in Quantum Physics. In this case, the resistance of MTJ change according to the relative angle of FM1 and FM2 as shown in Figure I-1. This is called Tunnel magnetoresistance (TMR) effect. The degree of resistance change is evaluated with TMR ratio as defined below.

$$\boldsymbol{TMR\ ratio} = \frac{\boldsymbol{R_{AP} - R_P}}{\boldsymbol{R_P}} \times \mathbf{100}\ [\%] \tag{1}$$

R_P denotes the resistance of parallel (P) configuration, which is the lowest resistance. On the other hand, R_{AP} denotes the resistance of anti-parallel (AP) configuration, which is the highest resistance. The first study of the TMR effect was conducted by Julliere in 1975[7], where a TMR ratio of 14% was observed in a Fe/GeO/Co structure at the low temperature (LT) of 4.2K, but it was not observed at room temperature (RT). TMR effect at RT was firstly reported by T. Miyazaki at Tohoku University (TMR = 18% with Fe/Al-Ox/Fe @ RT)[8] and J. S. Moodera at MIT (TMR = 11% with CoFe/Al-O_x/Co @ RT)[9] at the same time in 1995.

TMR effect can be described using Julliere model (Figure I-2)[7]. All spins are divided into up-spin and down-spin, where the quantities of up-spin and down-spin are different (= polarized) in ferromagnetic materials. Up-spin and down-spin in FM1 at Fermi energy (E_F) tunnel into up-spin state and down-spin state in FM2 respectively if we suppose that tunneling spins conserve their spin states (not flipped). Here, we can understand that the conductance in P state is clearly larger than AP state because P state has the big tunneling path from Majority of FM1 to Majority of FM2. We can describe the tunneling conductance for P (G_P) and AP (G_{AP}) as below:

$$\begin{aligned} \boldsymbol{G_P} &\propto \boldsymbol{D_{1M}(E_F)D_{2M}(E_F) + D_{1m}(E_F)D_{2m}(E_F)} \\ \boldsymbol{G_{AP}} &\propto \boldsymbol{D_{1M}(E_F)D_{2m}(E_F) + D_{1m}(E_F)D_{2M}(E_F)} \end{aligned} \tag{2}$$

Where, $D_{1M}(E_F)$ denotes the density of Majority states of FM1 at E_F for example. Then, we can define spin polarization (P) as below:

$$\begin{aligned} \boldsymbol{P_1} &= \frac{\boldsymbol{D_{1M}(E_F) - D_{1m}(E_F)}}{\boldsymbol{D_{1M}(E_F) + D_{1m}(E_F)}} \\ \boldsymbol{P_2} &= \frac{\boldsymbol{D_{2M}(E_F) - D_{2m}(E_F)}}{\boldsymbol{D_{2M}(E_F) + D_{2m}(E_F)}} \end{aligned} \tag{3}$$

Therefore, TMR ratio is also defined using P_1 and P_2:

$$\boldsymbol{TMR\ ratio} = \frac{\boldsymbol{2P_1P_2}}{\boldsymbol{1 - P_1P_2}} \times \mathbf{100}[\%] \tag{4}$$

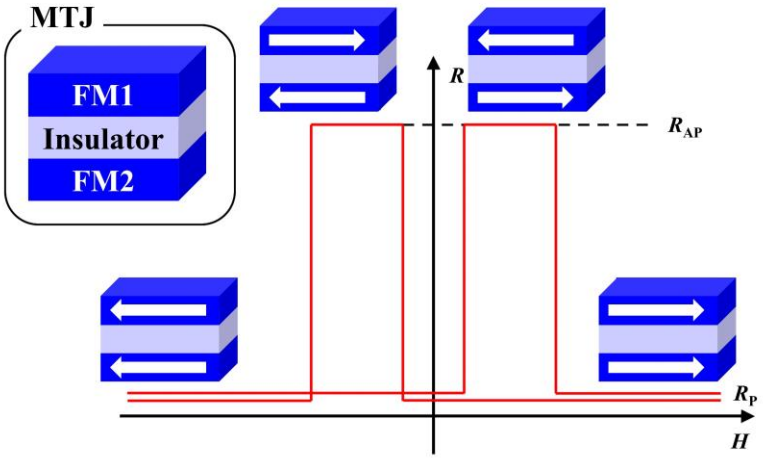

Figure I-1 Magnetic tunnel junction and tunnel magnetoresistance effect

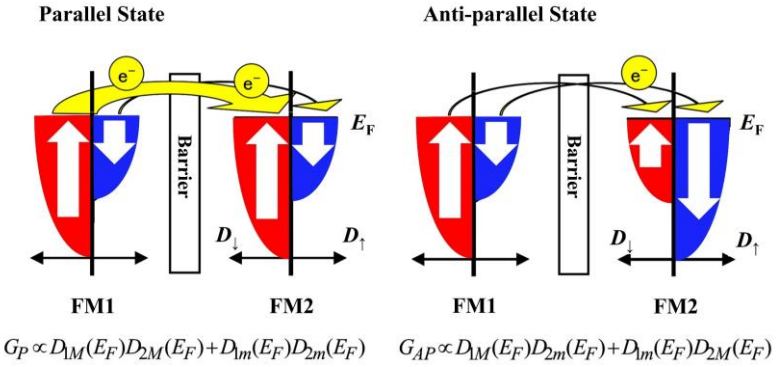

Figure I-2 Julliere model

3. MTJ using crystalized (001)-MgO barrier

Conventionally, amorphous Al-Ox materials have been used as the insulating layer. In amorphous materials, due to the random arrangement of atoms, electrons undergo random scattering during the tunneling process, and information related to the in-plane wave vector k// of the tunneling electrons is lost. On the other hand, in 2001, first-principle calculations were conducted on a crystallized Fe(001)/MgO(001)/Fe(001) MTJ, both in terms of the ferromagnetic layer and insulating layer, and a very high TMR ratio of 1000% was theoretically predicted by Butler et al[10]. The mechanism is explained below.

In an MTJ using a crystallized insulating layer with a regular in-plane arrangement, electrons tunnel without undergoing random scattering, preserving their symmetry (Bloch states). Figure I-3 shows the band dispersion diagram for Fe [001] (k//=0). Near the Fermi level, which contributes to conduction, there are Bloch states of Δ_1, $\Delta_{2'}$, Δ_5 in the Majority, and Δ_5, Δ_2, $\Delta_{2'}$ in the Minority. Figure I-4 shows the state density of tunneling electrons with each of these Bloch states in MgO(001). At this time, in the parallel state Majority→Majority tunneling process (a), it is evident that only Δ_1 electrons occupy the majority of the conductance. In other tunneling processes (b)(c)(d), all Bloch states significantly attenuate during the tunneling process. Although the above discussion pertains to k//=0, the situation is different for k//≠0. Figure 1-1-5 shows calculated tunneling probabilities for parallel and antiparallel states in the k// in-plane. The results in the parallel state are consistent with the Δ_1 electron dominant tunneling observed in Figure I-4. However, in the parallel state Minority and antiparallel state, conductance peaks are observed at k//≠0. The presence of conductance in the antiparallel state limits the TMR ratio.

Although high TMR ratios were theoretically predicted for MgO insulating layer MTJs, they were experimentally confirmed by Yuasa et al. in 2004[11]. Using molecular beam epitaxy, Yuasa et al. fabricated fully epitaxial Fe(001)/MgO(001)/Fe(001) MTJs and reported TMR ratios exceeding the theoretical limits of the Julliere model: 88% at room temperature and 146% at low temperatures. Following this report, research on MgO insulating layer MTJs accelerated, and Yuasa's group optimized the fabrication conditions to achieve a TMR ratio of 180% at room temperature[12]. In the same year, 2004, Parkin et al. reported a TMR ratio of 220% at room temperature in CoFe/MgO/CoFe MTJs fabricated by sputtering[13]. These MTJs have epitaxial relations only in the in-plane direction and are (001) oriented, which is considered to be the reason for such high TMR ratios.

In 2005, Djayaprawira et al. reported a TMR ratio of 230% at room temperature in CoFeB/MgO/CoFeB MTJs using amorphous CoFeB as the ferromagnetic layer[14]. In this report, the polycrystalline MgO film sputtered on amorphous CoFeB grow with (001) orientation, and the top CoFeB ferromagnetic layer also grow amorphously. To achieve high TMR ratios, crystallization at the ferromagnetic layer/insulating layer interface is necessary, but in this MTJ, it was confirmed that the amorphous CoFeB grows as an in-plane polycrystalline film on (001) oriented MgO after annealing process (Figure I-6)[15]. Furthermore, in 2008, Ikeda et al. optimized the fabrication conditions of this CoFeB/MgO/CoFeB MTJ, reporting TMR ratios of 604% at room temperature and 1144% at low temperatures, approaching the theoretical predictive limits[16].

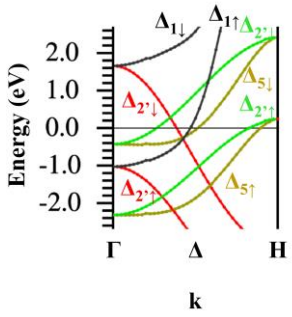

Figure I-3 Fe band structure

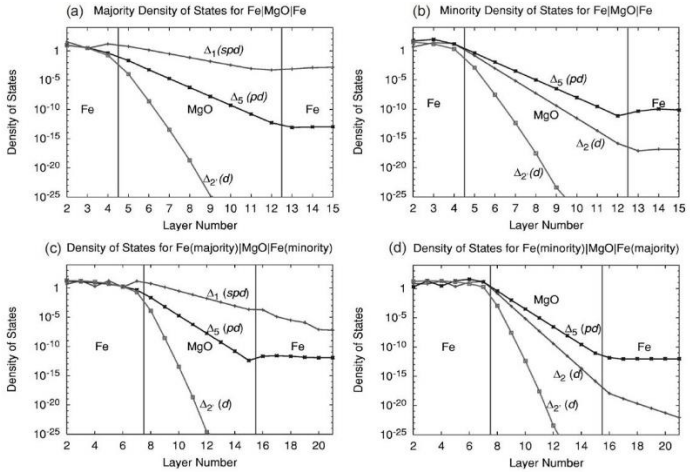

Figure I-4 Tunneling rates for various spins

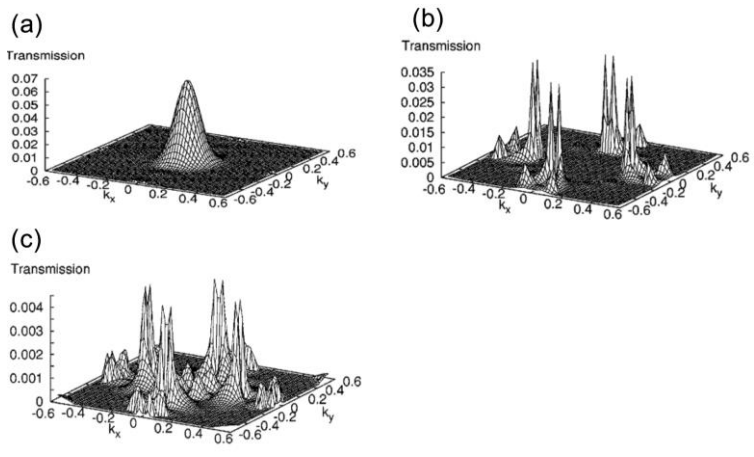

Figure I-5 Calculated results of the tunneling probability in the k// in-plane. (a) Parallel state, Majority, (b) Parallel state, Minority, (c) Antiparallel state.

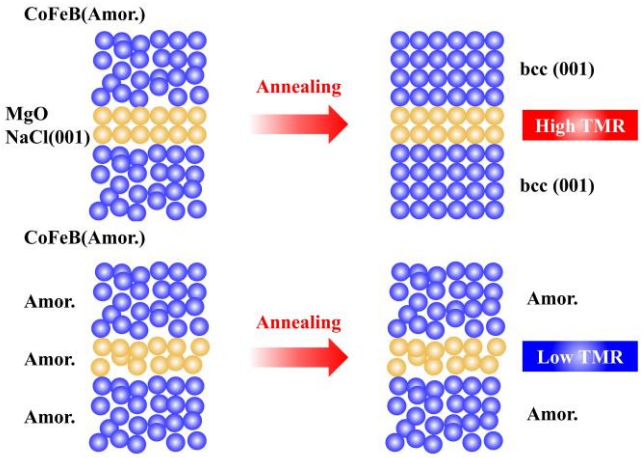

Figure I-6 Mechanism of high TMR with CoFeB/MgO/CoFeB-MTJ

4. Magnetic sensor

Magnetic sensor is a good application using TMR effect, which is called TMR sensor[17]. There are AMR sensor and GMR sensor using AMR effect and GMR effect respectively as well among the sensors that utilize spintronics[18]. There are various applications for magnetic sensors, including read magnetic heads for HDDs, electric compasses detecting geomagnetic fields, automotive acceleration sensors, non-destructive sensors for detecting defects inside objects, and the bio-magnetic sensor which is the focus of this research.

Figure I-7 compares various magnetic sensors with the perspectives of Detectivity and Dynamic range[18–29]. Hall elements, which use the Hall effect (a current magnetic effect), offer the advantage of linear output but have the disadvantage of significant temperature dependency due to being semiconductors[30]. Fluxgate (FG) elements, utilizing electromagnetic induction, can sensitively detect static magnetic fields or low-frequency magnetic fields, but their disadvantages include high power consumption and detectivity reduction with miniaturization[31,32]. Magneto Impedance Sensors (MI Sensors), which apply the magneto-impedance effect[33,34], are highly sensitive[35] but require alternating current power and output correction, and exhibit detectivity dependent on sensor unit size, decreasing with miniaturization[36]. SQUIDs (Superconducting Quantum Interference Devices) represent ultra-high sensitivity magnetic sensors, reading external magnetic fields through the change in resonance conditions of Josephson junctions made from superconducting rings, and have an extremely low detectivity of 100 fT[37,38]. However, they require elaborate equipment due to the need for low-temperature operation using liquid helium, making their running costs substantial[39]. Optical pumping devices, recently achieving sensitivities comparable to SQUIDs, are limited to use in shielded rooms due to

their small dynamic range. Furthermore, the Zeeman effect coefficient, a critical factor for practical application, is not yet well understood[40,41]. In recent years, the development of diamond NV (Nitrogen-Vacancy) sensors as a new type of magnetic sensor has been progressing[42]. These sensors potentially have a high detectivity, but their complexity in principle and cost issues present challenges.

Here, we can clearly confirm that TMR sensor has both merits of good detectivity and wide dynamic range. In following sections, I'll explain the basic principle and promising application of TMR sensor in detail.

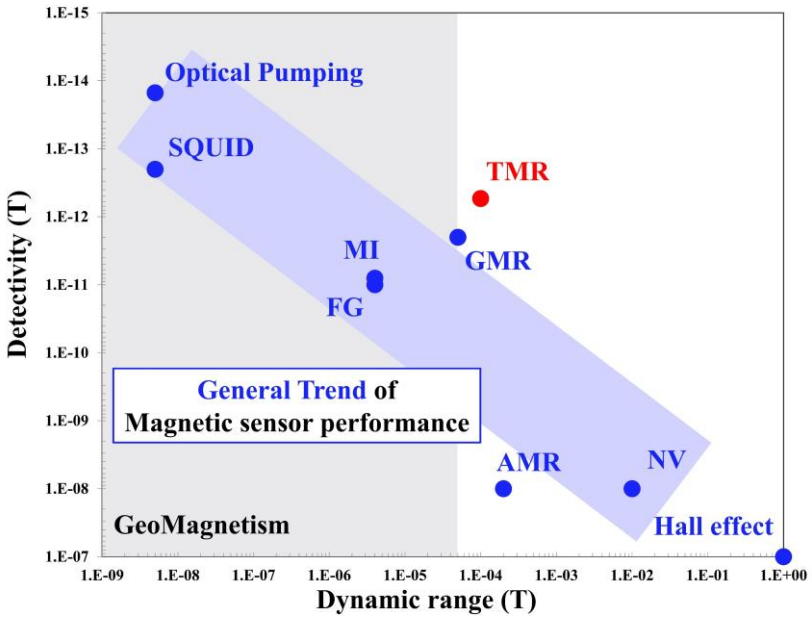

Figure I-7 Magnetic sensor comparison

5. TMR sensor

TMR sensor is a simple magnetic resistance effect-based sensor, operable at RT. It can work with just a direct current power source and a voltmeter, making them inexpensive to manufacture with low running costs. Also, the junction area of TMR elements is very small, less than tens of μm², allowing for considerable miniaturization of the sensor size. This enables high spatial resolution by placing sensors at high density. Furthermore, TMR sensors use an insulating barrier layer, allowing for low power consumption as the current required to obtain detectable voltage values is small.

Figure I-8 shows an ideal TMR curve for the application of magnetic sensor. The sensitivity of TMR sensor is defined below:

$$\boldsymbol{Sensitivity} = \frac{\boldsymbol{TMR\ ratio}}{\boldsymbol{2H_k}}\ [\%/\boldsymbol{Oe}] \tag{5}$$

In addition, the detectivity of TMR sensor is defined below using S_v (noise level) and bias voltage (V_{Bias}):

$$\boldsymbol{Detectivity} = \frac{\mathbf{1}}{\boldsymbol{Sensitivity}} \sqrt{\frac{\boldsymbol{Sv^2}}{\boldsymbol{V_{Bias}}^2}} \left[\boldsymbol{T/\sqrt{Hz}}\right] \tag{6}$$

There are two important points to realize the ideal TMR curve.

The first point is that the magnetization of pinned layer has to be pinned literally. Previous work already discovered the spin-valve structure, where an anti-ferromagnetic material contacted with the pinned layer ferromagnet pins its magnetization with the annealing process under magnetic field[43].

The second point is the linear response around zero field. Here, our group has previously suggested the method of performing two annealing process on the sample[44]. The concept diagram is shown in Figure I-9. When an annealing under magnetic field is applied to an MTJ, an exchange bias is added to the pinned layer, and induced magnetic anisotropy is added to the free layer. The induced magnetic anisotropy in the free layer occurs due to a slight shift in atomic positions caused by the magnetic field annealing, altering the magnetic anisotropy. Initially, the MTJ deposited in a magnetic field possesses uniaxial anisotropy. The first annealing is conducted while applying a magnetic field along the easy axis of both the free layer and the pinned layer. This first annealing is performed at a temperature higher than both the temperature at which exchange bias is applied to the pinned layer and the temperature at which induced magnetic anisotropy is added to the free layer. Subsequently, the MTJ undergoes a second annealing at a lower temperature than the first, with the direction of the magnetic field rotated by 90 degrees. The temperature of this second annealing is set lower than the temperature at which exchange bias is added to the pinned layer but higher than the temperature at which induced magnetic anisotropy is applied to the free layer. This second annealing allows for the rotation of the direction of the induced magnetic anisotropy in the free layer by 90 degrees, while the direction of uniaxial anisotropy and exchange bias in the pinned layer remains unchanged. Through this process, the easy axes of the pinned and free layers become orthogonal to each other, and the magnetoresistance curve reflects the magnetization curve in the hard axis direction of the free layer. Consequently, it is believed that the magnetoresistance curve become linearly around zero magnetic field.

In the next section, I'll explain the detection of Magneto-Encephalo-Graphy (MEG), which is the promising application of TMR sensors.

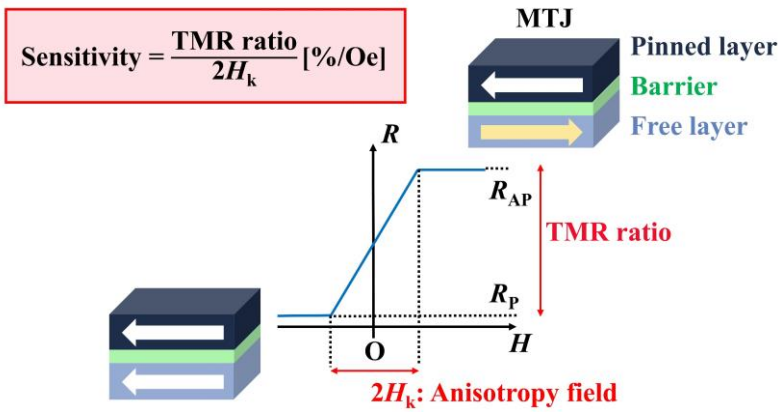

Figure I-8 TMR sensor principle.

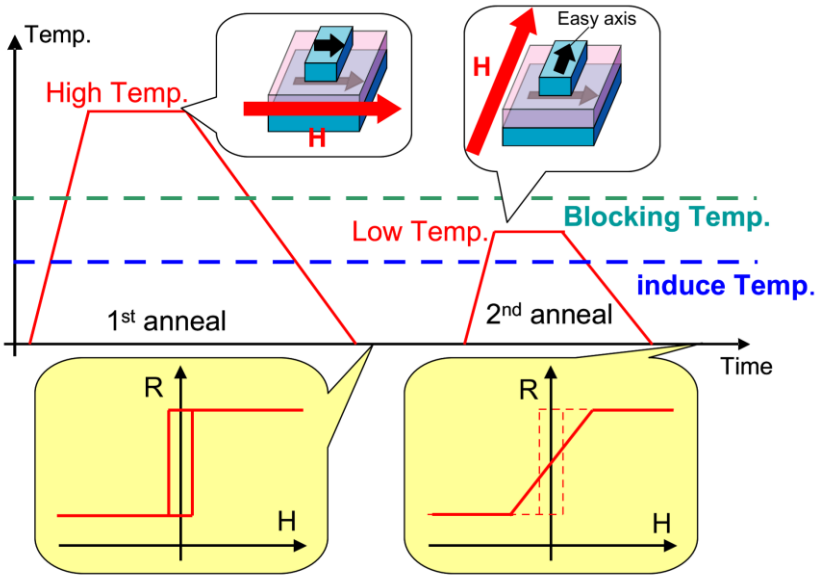

Figure I-9 Orthogonalization of Easy Axes and Linear Magnetoresistance Curve Achieved by Two-step annealing process

6. MEG detection and TMR sensor

In recent years, the advancement of Artificial Intelligence (AI) has been remarkable, and we are encountering a significant change of the world as various aspects of our daily lives are being replaced by AI. While the evolution of AI represents an innovation in the software side, on the hardware side, the evolution of electronics has led to the miniaturization of devices and a dramatical improvement in measurement and signal processing technologies. Currently, there is a growing trend of integrating AI with these measurement technologies to advance neuroscience. This technology, blending the Brain with Technology, is called as 'Braintech' (or Neurotech), and it is believed that its market size could expand to several

trillion to tens of trillions of yen by around 2040 (Figure I-10) [45]. The founding of Neuralink by Elon Musk in 2017 marked the beginning of Braintech as a globally highly expected next-generation technology[46]. The applications of Braintech are incredibly diverse, including medical uses, BMI (Brain-Machine Interface: a technology that connects the brain and machines, interpreting human thoughts to control machines and robots), and neuromarketing, among others (Figure I-11).

Various techniques for measuring brain activity have been considered, but the most common method involves placing electrodes on the brain to measure Electro-Encephalo-Graphy (EEG). However, this method only allows for the collection of information from the surface of the brain. To access deeper brain information, invasive devices with electrodes inserted deep into the brain are necessary. Therefore, a new method of measuring brain information is collecting attention: the detection of Magneto-Encephalo-Graphy (MEG). Magnetic fields have the property of penetrating the brain, making it theoretically possible to read deep brain information even when sensors are placed on the brain's surface. Traditionally, SQUIDs have been the mainstream for measuring brain magnetic fields. However, the detectivity of TMR sensors has dramatically improved in recent years. These sensors are gaining attention as an overwhelmingly simpler method than SQUIDs for detecting brain magnetic fields at RT (Figure I-12).

Recently, our group has achieved the lowest detectivity of TMR sensor in the world approaching SQUID as shown in Figure I-13[47], where we used CoFeSiB free layer which would be explained later. Then, we demonstrated the measurement of cerebral field as shown in Figure I-14, where we successfully observed the cerebral field signal similar to SQUID with very compact TMR sensor. Moreover, TMR sensor can potentially obtain this result outside of a magnetic shield room as a benefit of its wide dynamic range. However, the TMR signal is still noisy compared to SQUID, which means that we need to more improve the detectivity of TMR sensor.

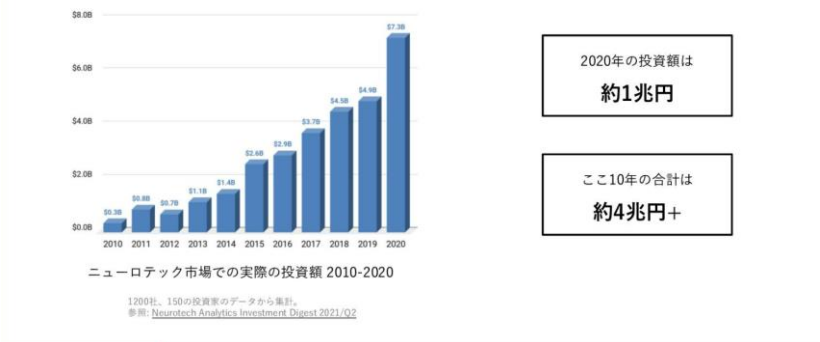

Figure I-10 Investment Scale of the Braintech (Neurotech) Market (Global)

Figure I-11 Examples of Applications of Braintech

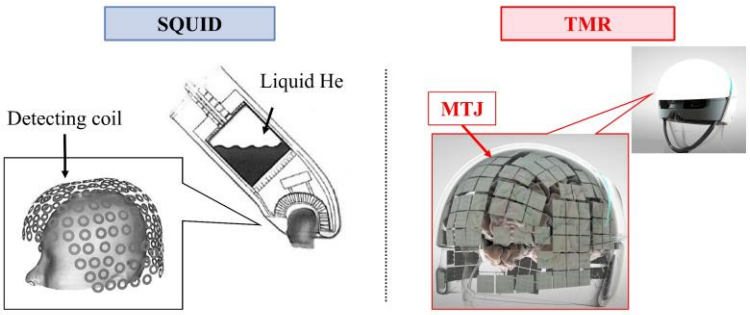

	SQUID	TMR
Sensitivity	○	○
Operating temperature	Low temeperature	Room temperature
Size	Large	Compact
Cost	High (several hundred million yen)	Low (several million yen)
Power consumption	High	Low
Spatial resolution	Low	High
Wearability	×	○

Figure I-12 Comparison between SQUID and TMR Sensors

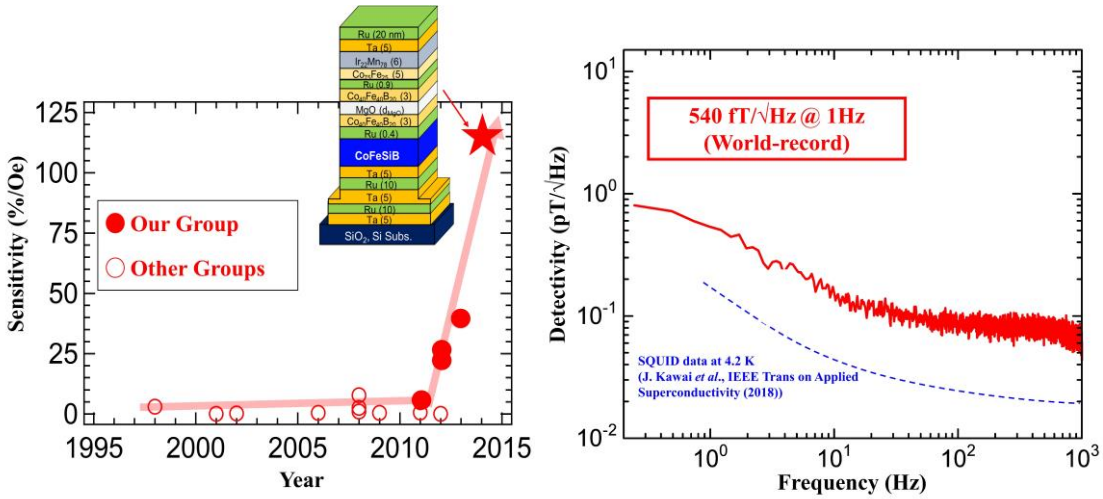

Figure I-13 TMR sensor development in our group

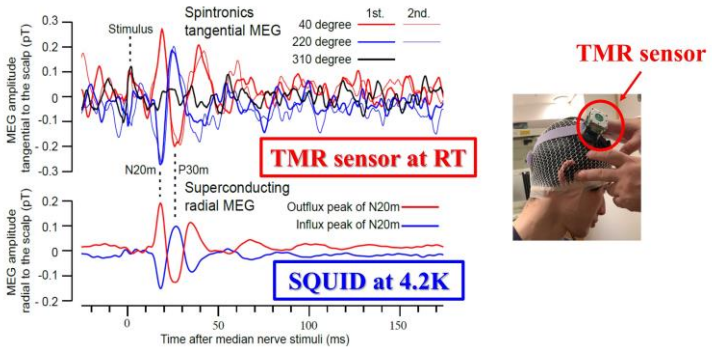

Figure I-14 Demonstration for measurement of cerebral field using TMR sensor

7. Conventional approach to improve the performance of TMR sensor

To date, numerous studies have been conducted to improve the detectivity of TMR sensors aimed at detecting bio-magnetic fields. Particularly, various materials have been examined for the free layer material, which significantly affects both the improvement of TMR ratio and the reduction of H_k. To reduce H_k, soft magnetic materials with low magnetic anisotropy are required, and this section summarizes the soft magnetic materials examined so far, including their implementation in MTJ structures.

① MTJ Structure Using NiFe Free Layer

NiFe (Permalloy) refers to a binary alloy of NiFe containing about 80% Ni, as well as multicomponent alloys with additions of Mo, Cu, Cr, etc. It is an excellent soft magnetic material derived from "permeability + alloy." NiFe with 35-100% Ni forms a metal solid solution and has an fcc structure. Figure I-15 shows the composition dependence of NiFe's magnetic anisotropy constant K_1 and magnetostriction constant λ_s [48]. When Ni and Fe are randomly arranged in an irregular structure due to rapid cooling, K_1 becomes zero at around 75% Ni composition, and λ_s also becomes zero at a similar composition, exhibiting excellent soft magnetic properties. However, if Ni_3Fe becomes ordered due to slow cooling, the composition at which K_1 becomes zero shifts significantly, and K_1 and λ_s do not simultaneously reach zero, failing to exhibit soft magnetic properties. Therefore, it is necessary to inhibit the growth of Ni_3Fe ordered structure in bulk NiFe through rapid cooling. Although the compositions at which K_1 and λ_s of NiFe alloy become zero are not exactly the same, attempts have been made to add small amounts of Mo, Cu, Cr, or Si to simultaneously bring K_1 and λ_s to zero and to suppress the growth of the Ni_3Fe phase. For example, Egelhoff, Jr. et al. have reported a low H_k of 0.8 Oe by depositing $Ni_{77}Fe_{14}Cu_5Mo_4$ using ion beam deposition[49].

Despite being an excellent soft magnetic material, the crystal structure of NiFe is fcc, which poses a problem when creating structures like CoFeB/MgO/NiFe or CoFeB/MgO/CoFeB/NiFe[50]. The coherent tunneling of Δ_1 electrons is not realized, leading to a significant reduction in TMR ratio compared to MTJs using only CoFeB as the free layer. In our lab, we designed an MgO barrier MTJ using a CoFeB/Ru/NiFe synthetic structure for the free layer and achieved high magnetic field sensitivity of 25%/Oe at RT (Figure I-16) [51]. When the thickness of the intermediate layer Ru is 0.4~1.0nm, the magnetizations of the CoFeB layer and the NiFe layer oscillate between parallel and antiparallel coupling depending on the thickness of the Ru layer[52]. Particularly, an antiparallel coupling is utilized when the thickness of Ru is 0.85nm. This choice is based on a balance between coupling strength (about 200 Oe) and thermal resistance (about 325°C). Under this structure, the magnetizations of the CoFeB and NiFe layers are antiparallel near zero magnetic field, and if the NiFe layer is sufficiently thicker than the CoFeB layer, the CoFeB layer reflects the soft magnetic reversal of the NiFe layer. Furthermore, the intermediate Ru layer structurally disconnects the NiFe and CoFeB layers, minimizing the change in the structure of bcc-CoFeB due to the fcc structure of the NiFe layer. Therefore, it is possible to realize soft magnetic reversal while maintaining a high TMR ratio. However, considering the sensitivity of 100%/Oe required for MEG detection, a further few times improvement in sensitivity is required. Additionally, the complexity of the film structure due to the synthetic structure leads to increased production costs.

② MTJ Structure Using CoFeSiB Free Layer

CoFeSiB is an amorphous material, and ideally, its K_1 becomes zero. Additionally, when the composition is $Co_{70.5}Fe_{4.5}Si_{15}B_{10}$, the magnetostriction, or λ_s, becomes zero (Figure I-17) [48]. This implies that it is an exceptionally soft magnetic material. The magnetoresistance curve of an MTJ using a CoFeSiB free layer is shown in Figure I-18[53]. Like the NiFe free layer MTJ shown in Figure I-16, a synthetic structure using Ru is adopted for the free layer. A very high magnetic field sensitivity exceeding 100%/Oe was observed, making it a standard structure for TMR sensor. However, simplification of the film structure is also needed as the MTJ using a NiFe free layer. The complexity of the film structure of the MTJ using a CoFeSiB free layer arises not only from the use of the synthetic structure but also from the high electrical resistivity of the CoFeSiB layer, making it unsuitable as a lower electrode. Therefore, a lower electrode layer of Ru is inserted as an underlayer.

③ MTJ Structure Using Heusler Alloy Free Layer

Heusler alloys are a type of half-metal material. I'll explain half-metal materials and Heusler alloys here. As mentioned earlier, for improving sensor sensitivity, ferromagnetic materials with high TMR ratio are required, and high spin polarization half-metal materials have attracted attention. Figure I-19 shows the DOS concept diagram of half-metal materials. Half-metal materials are those in which one spin at the Fermi level exhibits metallic properties, while the other spin exhibits insulating properties. At this time, the spin polarization rate becomes 1, so if such half-metal materials are used in an MTJ, the TMR ratio theoretically diverges to infinity. Although in reality, the TMR ratio does not diverge infinitely due to the effects of bias voltage and spin flip during electron tunneling, these materials are expected to yield a larger TMR ratio compared to general 3d electron system materials (such as Co, Fe).

Heusler alloys are ordered alloys with a molecular formula of X_2YZ and were confirmed to exhibit ferromagnetism in a Cu-Mn-Al composition by F. Heusler in 1903 [54]. Recently, several compositions of Co-based Heusler alloys with the composition Co_2YZ have been reported to exhibit half-metallicity through first-principle calculations[55]. Because of this background, research on MTJs using Heusler alloys as ferromagnetic layers, such as Co_2MnSi and Co_2MnGe, has accelerated[56,57].

The results of previous studies on MTJs using Heusler alloys as free layers in our lab are summarized below. Figure I-20 shows a prior study on the composition dependence of TMR ratio in MTJs with $Co_2Fe_xMn_{1-x}Si$/Al-O/$Co_{75}Fe_{25}$ structure[58]. $Co_2Fe_xMn_{1-x}Si$ is reported to exhibit half-metallicity in the case of $x = 0.0 \sim 0.6$, and compared to Co_2MnSi, it possesses characteristics such as low H_c and low H_k, making it a material expected to achieve both high TMR ratio and good soft magnetic properties[59]. Figure I-21 shows the film structure and magnetoresistance curve of an MTJ using $Co_2Fe_{0.4}Mn_{0.6}Si$ as the free layer and MgO as the insulating layer[60]. The feature of this structure is that $Co_2Fe_{0.4}Mn_{0.6}Si$ has a bcc structure, hence has an epitaxial relationship with MgO, eliminating the need for an insertion layer to promote Δ_1 electron coherent tunneling between $Co_2Fe_{0.4}Mn_{0.6}Si$ and MgO. However, the result was an almost linear magnetoresistance curve with lower sensitivity compared to MTJs using NiFe or CoFeSiB as the free layer.

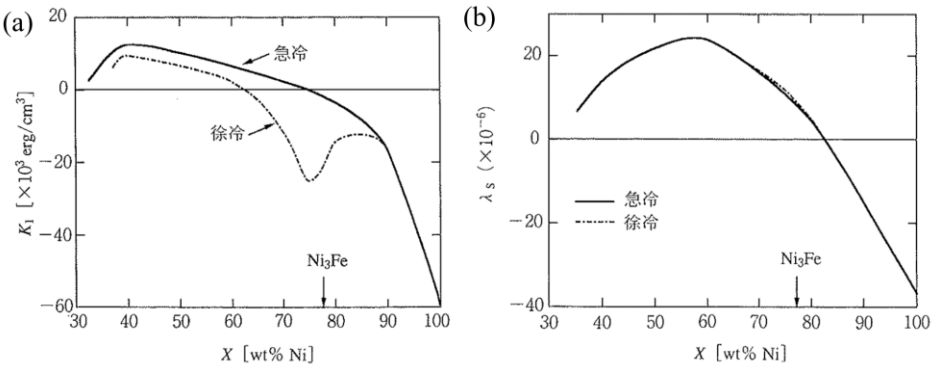

Figure I-15 Composition dependence of (a) crystal magnetic anisotropy constant K_1 and (b) magnetostriction constant λ_s of NiFe

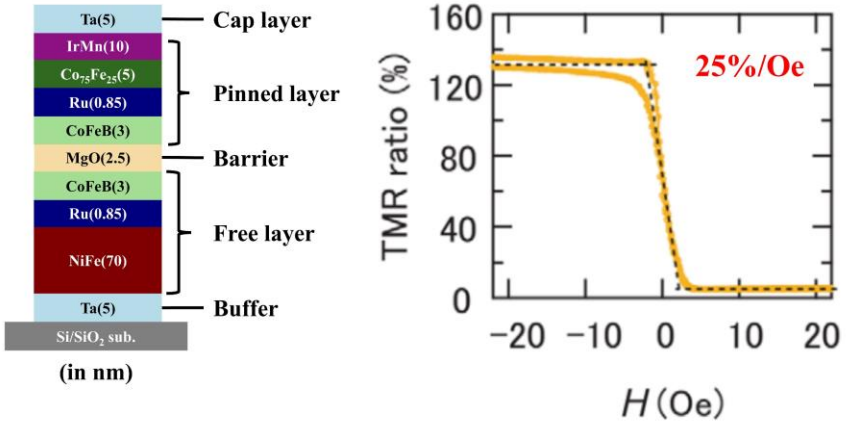

Figure I-16 Sracking structure and magnetoresistance curve of MTJ structure using NiFe free layer

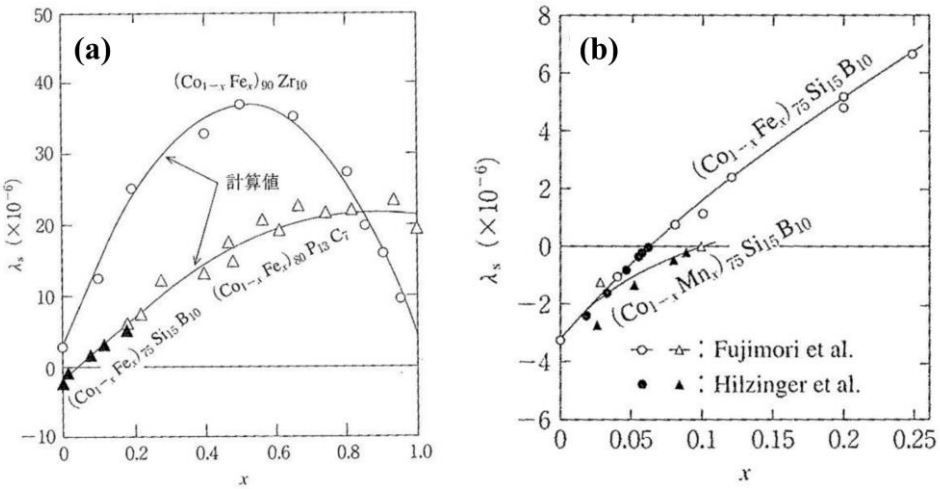

Figure I-17 Composition dependence of λ_s of CoFeSiB

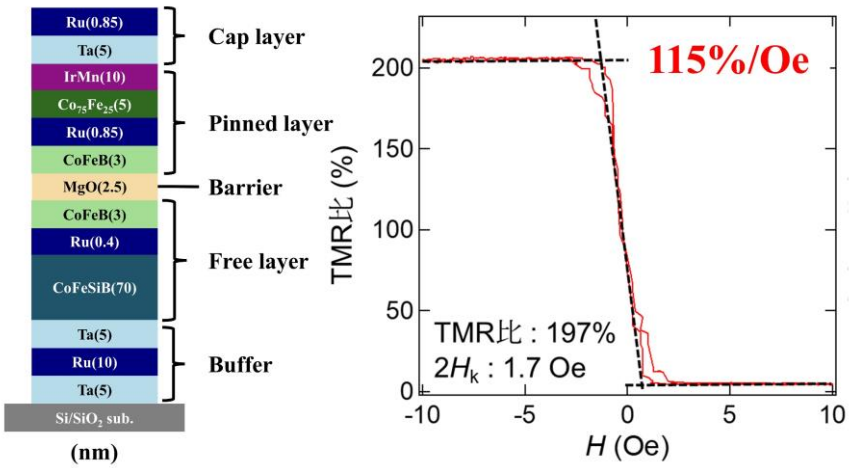

Figure I-18 Film structure and magnetoresistance curve of MTJ structure using CoFeSiB free layer

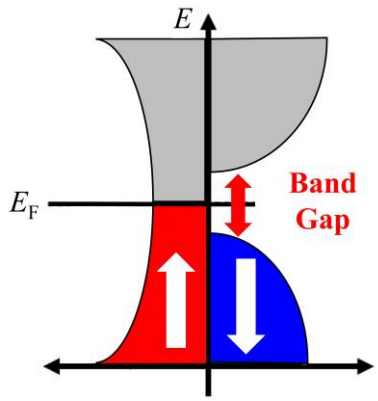

Figure I-19 DOS concept diagram of ferromagnetic materials with half-metallic properties

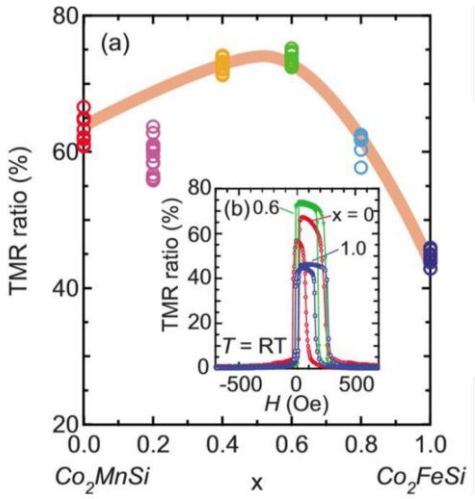

Figure I-20 In MTJ structure with $Co_2Fe_xMn_{1-x}Si$/ Al-O/ $Co_{75}Fe_{25}$: (a) Composition dependence of TMR ratio, (b) Composition dependence of TMR curve

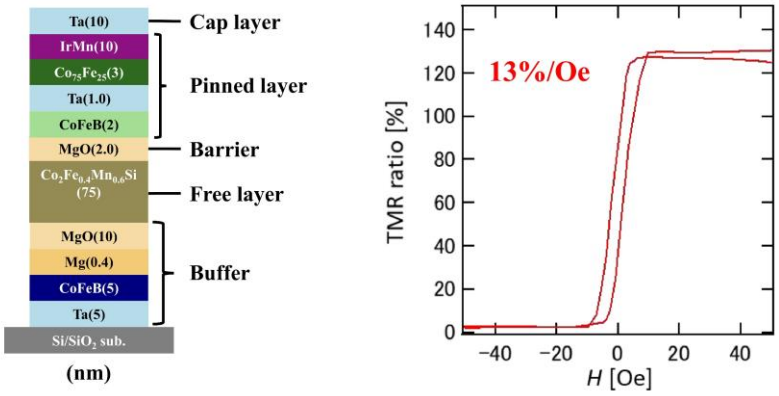

Figure I-21 Film structure and magnetoresistance curve of MTJ using Heusler alloy as free layer

8. Approach of This Study

In the previous section, I summarized the free layer materials previously considered for improving the performance of TMR sensors and their sensor characteristics. Figure I-22 summarizes sensitivity potentials of free layer materials, where none have yet reached the target sensitivity of SQUID level. In the context where the sensitivity of TMR sensors seems to be saturating, exploring novel free layer materials as alternatives to traditionally used NiFe or CoFeSiB can potentially lead to a significant improvement in sensitivity, making it a highly meaningful approach.

In this study, I focused on the Sendust alloy ($Fe_{73.7}Al_{9.7}Si_{16.6}$ at.%, hereafter Sendust or FeAlSi) discovered by the Institute for Materials Research at Tohoku University. FeAlSi with a bulk form has various applications, such as magnetic heads[61–63]. However, there is no prior research on nm-film fabrication of Sendust, which would be applicable to MTJs, while only thicker than μm order FeAlSi are investigated[64–67]. Therefore, this study's approach is highly original, which includes verifying the feasibility of thin-film fabrication and exploring the potential application to TMR sensors from scratch.

① Sendust alloy

Sendust is a soft magnetic material discovered in 1937 by Hakaru Masumoto and Tatsuji Yamamoto at the Institute for Materials Research, Tohoku University[68]. Sendust exhibits exceptional soft magnetic properties, showing characteristics equal to or better than the conventional soft magnetic material NiFe.

Table I-1 compares various properties of NiFe and Sendust[69]. Its DC permeability is higher than that of NiFe, and despite having a coercivity (H_c) value equivalent to that of NiFe, the production cost of Sendust, made from Fe, Al, and Si, is significantly cheaper compared to NiFe, which uses expensive Ni. Figure I-23 shows the composition dependence of the initial permeability of Sendust. It can be observed that the permeability increases sharply only near what is called the Sendust central composition, $Fe_{85}Al_{5.4}Si_{9.6}$ wt.%. This indicates that the soft magnetic properties of Sendust are exhibited only in a limited composition range. Masumoto and others made hundreds of different composition samples and repeated experiments many times, finally leading to the discovery of Sendust.

② The Origin of Soft Magnetism in Sendust

Sendust exhibits soft magnetic property only when its composition is near the central composition. Masumoto and others discovered Sendust by investigating compositions near where the magnetostriction constant was expected to become zero[70,43,44]. However, Wakiyama and others have thoroughly investigated the crystal magnetic anisotropy constant K_1 and saturation magnetostriction constant λ_s near the central composition of Sendust, analyzing that both K_1 and λ_s becoming zero simultaneously at the central composition is the key to its soft magnetic property (Figure I-24) [71]. In other words, the intersection of the $K_1 = 0$ line and the $\lambda_s = 0$ line on the Fe, Al, Si composition diagram corresponds to the central composition of Sendust. However, results from other research groups have reported that the $K_1 = 0$ line significantly differs from what Wakiyama and others have determined[72]. Wakiyama and others considered that the method of sample preparation could be the cause of this difference. Additionally, Takahashi and others have thoroughly investigated the K_1 and λ_s of Sendust in μm-order thick sputtered films[73], reporting that the intersection of the $K_1 = 0$ line and the $\lambda_s = 0$ line is the central composition of Sendust.

The crystal structure of Sendust is a $D0_3$ ordered structure, and it is believed that achieving the $D0_3$ ordered structure is also necessary for the achievement of its soft magnetic property[61]. Therefore, according to prior research on bulk materials, the soft magnetic property of Sendust is considered to be achieved through the combination of the central composition and the $D0_3$ ordered structure.

③ Potential of Sendust as a Novel Free Layer Material

Using Sendust as a free layer is considered to have several merits.

First, a high TMR ratio can be expected. The FeAlSi crystal structure is a $D0_3$-ordered structure, an ordered arrangement of bcc(A2)[74]. Figure I-26 shows the estimated epitaxial relationship between Sendust and MgO, with a lattice mismatch of 4.7%. While there is no prior research on epitaxial films of Sendust, and it is unknown if Sendust can epitaxially grow on MgO, the Heusler alloy $Co_2Fe_{0.4}Mn_{0.6}Si$ has been confirmed to epitaxially grow on MgO with a lattice mismatch of 5.3%. This suggests that an epitaxial relationship between Sendust and MgO is quite possible. If an epitaxial relationship exists between Sendust and MgO, the MTJ structure using Sendust as a free layer would be very simple, as shown in Figure I-27. Like the Heusler alloy, the feature of this MTJ is that Sendust has a bcc structure, enabling an epitaxial relationship with MgO, and the entire MTJ is manufactured in the (001) orientation. Therefore, high TMR ratios can potentially be realized without the need for insertion layers such as CoFeB, as suggested by theoretical calculations from previous research[10].

Second, it is possible to reduce H_k. As shown in this section, Sendust exhibits excellent soft magnetic properties in bulk state, equivalent or superior to free layer materials like NiFe. If Sendust is successfully thinned into films and maintains good soft magnetic properties in film state, it might exhibit lower H_k than other MTJ free layer materials.

Third, the film structure can be simplified. As shown in Figure I-27, the MTJ using Sendust (single-crystal) as a free layer has a much simpler film structure compared to conventional MTJs. Simplification of the film structure leads to reduced production costs, and if high sensitivity is achieved with the MTJ structure using Sendust as a free layer, Sendust has the potential to become the standard material for TMR sensor free layers.

From the above, using Sendust as a free layer could potentially realize both high TMR ratio and low H_k with just a single layer of Sendust, and further simplify the film structure compared to conventional methods, making Sendust a highly promising material as a novel free layer material.

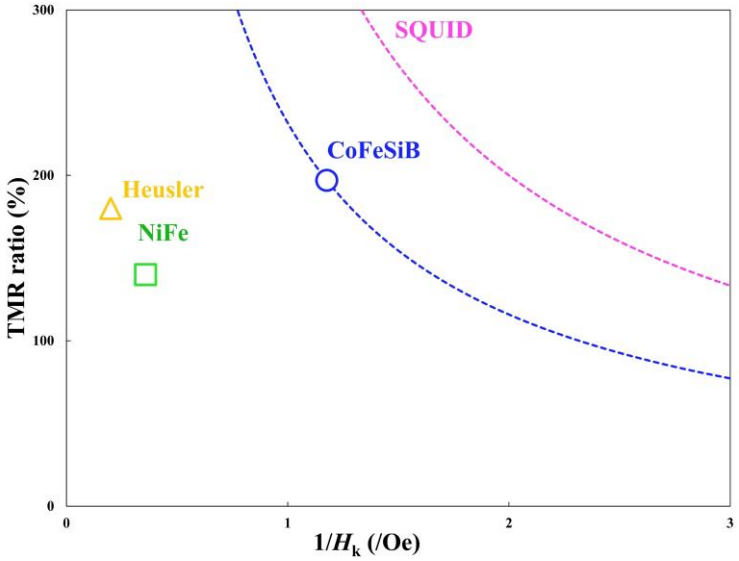

Figure I-22 Conventional sensor materials comparison[51,75,76]

Table I-1 Comparison of Characteristics between NiFe and Sendust

Soft Magnetic Material	μ_a (DC)	μ_a (4MHz)	B_s (G)	H_c (Oe)	ρ (Ω cm)	T_c (℃)
NiFe	20000	40	8700	0.05	55×10^{-6}	460
Sendust	30000	30	11000	0.05	80×10^{-6}	500

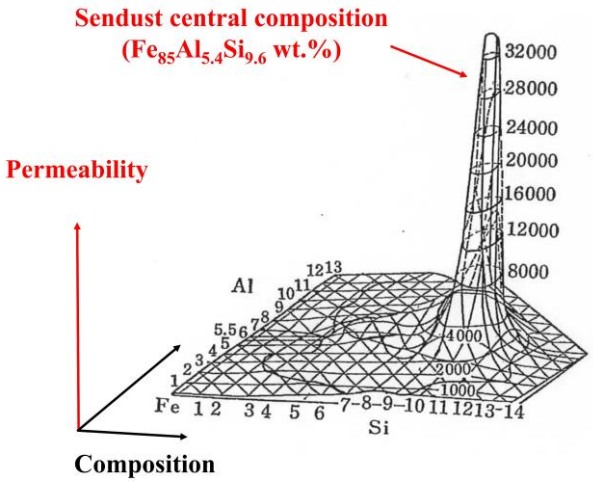

Figure I-23 Composition dependence of the initial permeability of Sendust

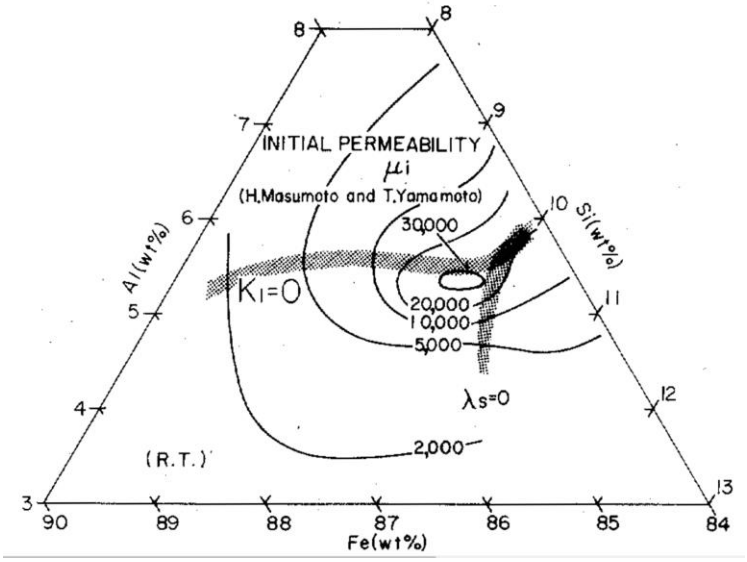

Figure I-24 Composition dependence of K_1 and λ_s near the central composition of Sendust

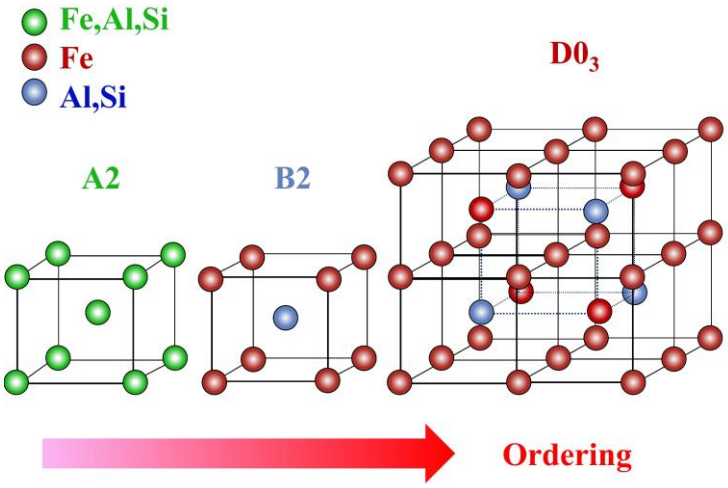

Figure I-25 Crystal structure of Sendust

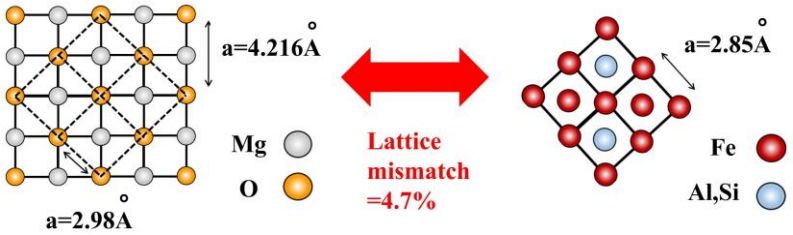

Figure I-26 Estimated epitaxial relationship between Sendust and MgO

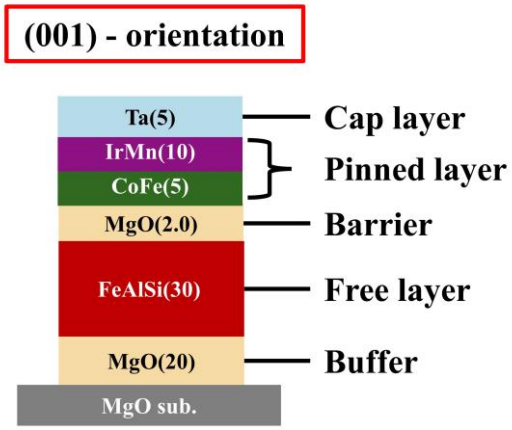

Figure I-27 MTJ structure using Sendust as the free layer

9. Purpose in this study

In this study, I firstly investigate the film property of FeAlSi alloy and its potential as a new free layer material in TMR sensor.

The purpose of this study is below.

Fabricate FeAlSi film of nm-order which has both of low magnetic anisotropy and high TMR ratio to show the potential sensitivity to apply for TMR sensor.

For proving the possibility of applying FeAlSi as a new free layer material, I set the target of the potential sensitivity as 100%/Oe, which is comparable to the conventional material of CoFeSiB as shown in Figure I-28. Additionally, I'll explore the strategy to achieve the performance comparable to SQUID.

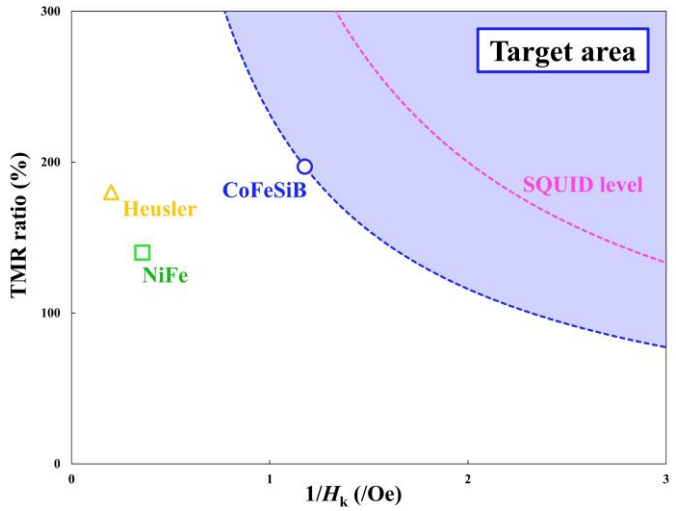

Figure I-28 Target of this study

II. Experimental methods

1. Film fabrication

In this study, I utilized a ULVAC-manufactured 10+3+1 element sputter device (commonly known as Helicon3) capable of depositing high-quality TMR multilayers. A schematic diagram is shown in Figure II-1. The device consists of four chambers: a preparation chamber (準備室), a transport chamber (搬送室), a deposition chamber (成膜室), and a sputtering chamber (スパッタ室), with their respective vacuum levels as shown in the figure. The samples are first transported to the transport chamber by a robotic arm and transferred to the deposition or sputtering chamber for deposition. The transport and deposition processes are fully automated and controlled by an integrated computer. In the deposition chamber, cathodes (CA) are numbered counterclockwise, starting from the one closest to the transport chamber. The sample holder in the deposition chamber includes a holder A capable of deposition in a magnetic field and a holder B capable of substrate heating and chamber thermal processing. Permanent magnets are attached at both ends of holder A, applying a magnetic field of approximately 100 Oe to the samples, inducing magnetic anisotropy in the deposited ferromagnetic thin films. Detailed heating mechanisms of holder B will be described later. The deposition chamber houses ten 2-inch target cathodes, the transport chamber has three 2-inch target cathodes (not used in this study), and the sputtering chamber contains one 4-inch target cathode. In this study, magnetic and non-magnetic metals were mainly deposited in the deposition chambers, while MgO was deposited as an insulating layer in MTJ in the sputtering chamber. The deposition method involved DC magnetron sputtering in the deposition and transport chambers, and RF magnetron sputtering in the sputtering chamber. Helicon sputtering was used in the deposition and transport chambers, where high-frequency voltage (13.56 MHz) is applied to a coil mounted directly above the cathode to generate inductively coupled plasma. This allows for concentrated, high-density plasma near the target even under low gas pressure, minimizing damage to the substrate. The distance between substrate and sample is approximately 30 cm in the deposition and transport chambers, and about 20 cm in the sputtering chamber. Pure 6N Ar gas was used as the process gas. Chamber pressures were monitored using diaphragm gauges attached to each chamber and controlled during deposition by mass flow controllers. The deposition conditions for each target material are summarized in Table II-1. For some ferromagnetic materials, the Ar flow and target power were increased to ensure plasma generation.

Regarding the substrates used for deposition, I used 10 mm square MgO(001) single crystal substrates. The substrates were ultrasonically cleaned with high-purity acetone and ethanol for 10 minutes each, then stirred in pure water, followed by N2 blow-drying. However, due to the hygroscopic nature of MgO substrates, surface moisture might not be completely removed by N2 blow-drying alone. Therefore, MgO substrates were flushed in the chamber at 600°C for one hour before deposition.

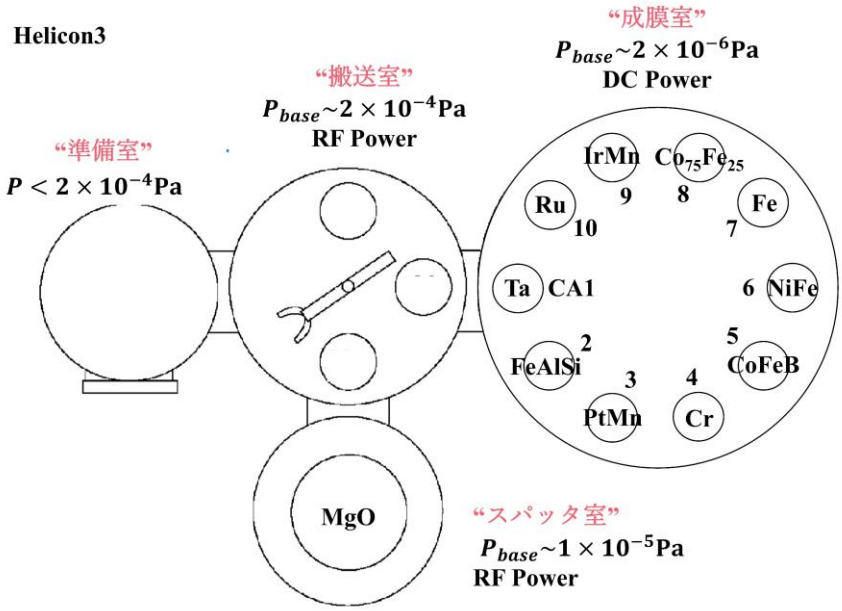

Figure II-1 Overview of Helicon 3 sputtering machine

Table II-1 Sputtering condition for each target

Target	Target Power (W)	Coil Power (W)	Ar flow (sccm)	Ar pressure (Pa)	Sputtering rate (Å/sec)
Ta	30	20	22.0	0.1	0.342
FeAlSi	150	20	22.0	0.1	1.009
Cr	30	20	35.0	0.1	0.171
CoFeB	100	20	22.0	0.1	0.568
$Co_{75}Fe_{25}$	30	20	35.0	0.15	0.255
IrMn	30	20	22.0	0.1	0.478
Ru	30	20	22.0	0.1	0.295
MgO	200	-	25.6	2.00	0.0757

2. Micro-fabrication process

For the measurement of the magnetoresistance curve of the deposited MTJ multilayer film, a microfabrication process using photolithography was conducted. The specific process flow is summarized in Figure II-2. In this study, after creating the Junction, an insulating film (SiO_2) was deposited, and a contact-hole process was adopted to form contact-holes. The sizes of the Junctions are three types: 80×40, 40×20, and 20×10 (μm²). The details of each process are summarized below.

① Photolithography

Photolithography is a method of microfabrication that involves applying photoresist to a substrate, transferring the pattern of a Cr mask onto the resist by ultraviolet exposure, and then developing it to create the resist pattern. For the resist, a positive-negative photoresist (AZ Electronic Materials' AZ5214E) was used. Cr masks for Junction formation (LOP JUNCTION), contact hole formation (LOP CONTACT), and top electrode formation (LOP ELECTRODE) were all manufactured by EQUA Corporation. For the exposure device, Mikasa's Aligner MA-20 was used, and the light source was a g-line mercury lamp (USH-500D). The following describes each step of the photolithography process.

■ Substrate Cleaning

The MTJ multilayer film sample was ultrasonically cleaned with acetone for 10 minutes, followed by N_2 blow-drying.

■ Dry Bake

After cleaning, to remove water adhered to the substrate, a substrate bake was performed on a 110°C hot plate for one minute.

■ Adhesion Promoter and Resist Application and Bake

To enhance the adhesion between the substrate and the resist, HMDS (AZ AD Promoter, commonly known as primer) was dropped, followed by spinning the substrate at 3000 rpm for 30 seconds using a spin coater to flatten the primer, and then dry baking for one minute. The resist was similarly dropped and spun at 4000 rpm for 30 seconds, then leveled for three minutes and dry baked for one minute.

■ Exposure

The substrate and Cr mask were attached to the aligner, brought into close contact, and then exposed at 30 EC.

■ Positive-Negative Reversal Bake

With the AZ5214E positive-negative reversal resist, a 120°C bake and overall exposure are performed after pattern exposure, turning it into a negative type of resist. The bake temperature requires control to the degree of 1°C, which was strictly managed using a hot plate.

■ Overall Exposure

Positive-negative reversal was performed by exposing at 120 EC using the aligner.

■ Development and Post Bake

The substrate was developed by immersing it in a developer solution (AZ MIF Developer). After soaking for two minutes, the substrate was stirred for 30 seconds and then rinsed with pure water for one minute. Finally, N_2 blow-drying was performed to remove water from the substrate surface, followed by dry baking for one minute.

② Ar Ion Milling

Junction formation was carried out by Ar ion milling. Ar ions were accelerated to ~1 keV and irradiated on the MTJ multilayer film, physically removing the surface based on the sputtering principle. In this study, an Electron Cyclotron Resonance Etching System (ULVAC's IBE-3000, commonly known as ECR2) was used. In this device, rough pumping is performed by a rotary pump, and the vacuum level reaches the 10^{-4} Pa range with a cryopump. The detailed milling conditions are shown in Table II-2. Atoms emitted from the substrate during etching were monitored with an endpoint monitor by Hiden Corporation, and the midpoint of the MgO insulating layer was used as the etching endpoint.

③ Interlayer Insulating Film Deposition

To insulate the Junction and electrodes, as well as the top and bottom electrodes, SiO_2 insulating film deposition was carried out using a Plasma CVD system by SAMCO. The deposition conditions are shown in Table II-3.

④ Contact Hole Formation

For the etching required to form contact holes, a Reactive Ion Etching System (ANELVA's EVP-39198, commonly known as RIE equipment) was used. The etching conditions of the RIE equipment are shown in Table II-4. Since ions and Ru do not react, using Ru as the cap layer of the MTJ automatically stops the etching at the cap layer.

⑤ Top Electrode Formation

For the deposition of the top electrode, ULVAC's four-element sputter system QAM-4-ST (commonly known as QAM) was used, and deposition was carried out by DC magnetron sputtering. QAM has two vacuum chambers, a preparation chamber, and a deposition chamber, each equipped with a two-inch cathode for four-element targets. Both chambers are vacuum-exhausted by rotary and turbo molecular pumps. The vacuum levels reached are below 5×10^{-3} Pa in the preparation chamber and below 2×10^{-5} Pa in the deposition chamber. In this study, Ta(5)/Al(200) (in nm) was deposited as the top electrode. The deposition conditions for each target are shown in Table II-5.

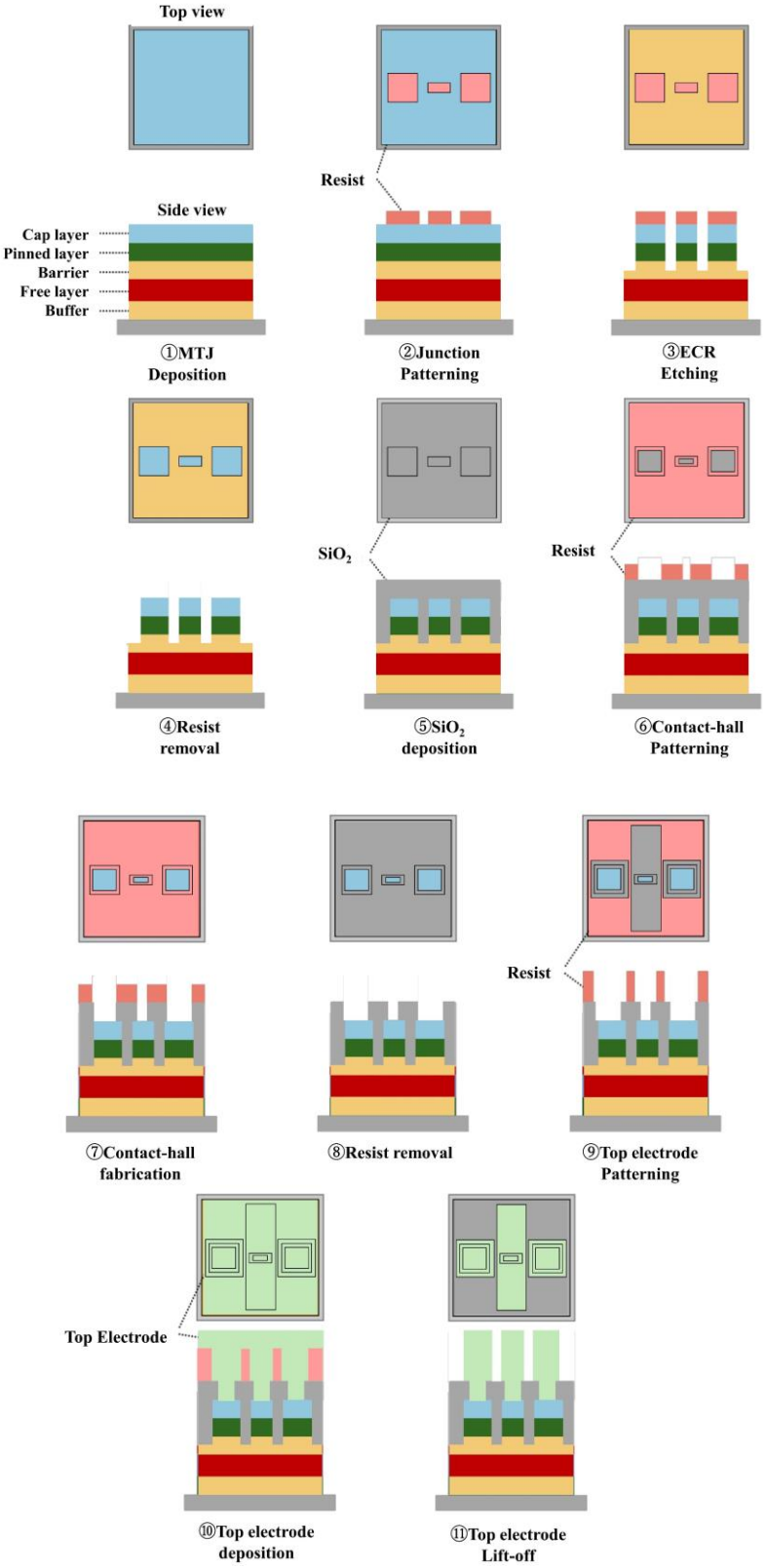

Figure II-2 Microfabrication process

Table II-2 ECR Milling Conditions

Anode current (mA)	A/D Voltage (V)	Acceleration Voltage (V)	Ar gas flow (sccm)	Ar gas pressure (Pa)	Etching angle (deg.)
100	500	400	4.2	0.2	15

Table II-3 CVD Deposition Conditions

Input Power (W)	Top Electrode (℃)	Bottom Electrode (℃)	TEOS Flow (sccm)	O_2 Flow (sccm)	Gas pressure (Pa)	Deposition time (sec)
60	200	280	3	237	45	100

Table II-4 RIE Etching conditions

RF Power (W)	CHF_3 gas flow (sccm)	O_2 gas flow (sccm)	Process gas Pressure (Pa)	Etching time (min)
20	44	1	10	30

Table II-5 QAM Deposition conditions

Target	Input Power (W)	Ar gas flow (sccm)	Ar gas pressure (Pa)	Deposition rate (Å/s)
Ta	100	12.0	0.20	0.718
Al	100	12.0	0.20	0.48

3. Annealing process

Annealing process is the heat treatment for the sample after deposition to achieve crystallization or ordering of the sample. In this study, there were two types of Annealing process: Annealing in a magnetic field, where a magnetic field is applied during the process, and Annealing process without a magnetic field, where no magnetic field is applied. A comparison of the devices used for annealing process is summarized in Table II-6.

Annealing without a magnetic field was conducted for the purpose of crystallizing and ordering the FeAlSi film. This was carried out using the thermal treatment mechanism equipped in the Helicon3 deposition chamber mentioned earlier. After the annealing process, the substrate was moved to CA1 for three hours of natural cooling.

Annealing in a magnetic field was conducted to promote crystallization at the interface between the MgO insulating layer and the ferromagnetic layer in the MTJ multilayers, and for pinning the pinned layer with an antiferromagnetic material. For this purpose, a custom-made device (commonly known as 東栄アニール) was ordered from TOEI Scientific Industrial corporation. The annealing was conducted under favorable conditions with an applied magnetic field of 1T and a vacuum level in the 10^{-5} Pa range. The sample was heated with the magnetic field applied in one direction, and once the target temperature was reached, it was maintained for 1 hour. Then, it was cooled at a rate of about 1°C/min, and the magnetic field application was terminated once the temperature inside the device dropped below 100°C.

Table II-6 Comparison of annealing system

Methods	**Magnetic field (T)**	***T* rising speed (℃/h)**	**Keeping time (h)**	**Pressure (Pa)**	**Cooling**
Helicon 3 Chamber	-	100	1	10^{-6}	3h Natural cooling
TOEI	1	300	1	10^{-5}	1℃/min. cooling

4. X-ray diffraction – XRD

I conducted X-ray diffraction (XRD) using D8-μHR by Bruker for evaluating crystal structure. The degree of $D0_3$ order (S_{D03}) and the degree of B2 order (S_{B2}) were calculated by using the intensity ratio between superlattice peaks (I_{111}-$D0_3$ and I_{222}-B2) and fundamental peaks (I_{444}-A2) observed in the (111)-plane / scan XRD patterns, with the following formulas as a Ref. [77]:

$$\boldsymbol{S} = \sqrt{\frac{\boldsymbol{I}^{\boldsymbol{obs.}}_{\boldsymbol{superlattice}} / \boldsymbol{I}^{\boldsymbol{obs.}}_{\boldsymbol{fundamental}}}{\boldsymbol{I}^{\boldsymbol{cal.}}_{\boldsymbol{superlattice}} / \boldsymbol{I}^{\boldsymbol{cal.}}_{\boldsymbol{fundamental}}}} \tag{7}$$

$$\boldsymbol{I}^{\boldsymbol{cal}}_{\boldsymbol{hkl}} = \boldsymbol{LP} \cdot \boldsymbol{\psi} \cdot \boldsymbol{F}^{\boldsymbol{2}}_{\boldsymbol{hkl}} \cdot \mathbf{exp}\left(-\boldsymbol{2B}\frac{\boldsymbol{sin^2\theta}}{\boldsymbol{\lambda^2}}\right) \tag{8}$$

LP is the Lorentz-Polarization factor of single crystals[78], ψ is the powder ring distribution factor[79], and F_{hkl} is the structure factor of the $D0_3$-FeAlSi unit cell for (hkl) diffraction. The factor expressed as an exponential function is a Debye-Waller factor.

The following is the calculation details. For example, the degree of $D0_3$ order is calculated by following equation.

$$\boldsymbol{S_{D03}} = \sqrt{\frac{\boldsymbol{I}^{\boldsymbol{obs.}}_{\boldsymbol{111}} / \boldsymbol{I}^{\boldsymbol{obs.}}_{\boldsymbol{444}}}{\boldsymbol{I}^{\boldsymbol{cal.}}_{\boldsymbol{111\_D0_3}} / \boldsymbol{I}^{\boldsymbol{cal.}}_{\boldsymbol{444\_D0_3}}}} \tag{9}$$

The calculation of $I^{\text{cal.}}$ is shown below. LP was calculated by using scattering angle θ measured by XRD,

$$\boldsymbol{LP} = \frac{\mathbf{1} + \mathbf{cos^2}\,\boldsymbol{2\theta}}{\mathbf{cos}\,\boldsymbol{\theta}\,\mathbf{sin^2}\,\boldsymbol{\theta}} \tag{10}$$

Ψ was calculated by following two equations, where the equipment parameter $s2$ was the angular divergence of the detector window and σ was the standard deviation of tilt angles of crystallites determined from the ω-scanned peak width,

$$\begin{aligned} \boldsymbol{a} &= \mathbf{arcsin}\frac{\mathbf{tan}\,\boldsymbol{s2}}{\mathbf{sin}\,\boldsymbol{2\theta}} \\ \boldsymbol{\Psi} &= \int_{\boldsymbol{0}}^{\boldsymbol{a}} \mathbf{exp}\left(-\frac{\boldsymbol{x^2}}{\boldsymbol{\sigma^2}}\right)\boldsymbol{dx} \end{aligned} \tag{11}$$

Structural factor F_{hkl} is calculated as follows, considering the crystal structure,

$$\boldsymbol{F_{hkl} = \sum_{j=1}^{N} f_j \exp\left(-2i\pi\left(hx_j + ky_i + lz_j\right)\right)} \quad (12)$$

where *x,y,z* are the positions of each atoms, and *f* is atomic form factor scattering considering atomic numbers and scattering angle θ.

The temperature parameter *B* was calculated by plotting $\ln\{I^{obs.}{}_{hkl}/(LP \cdot \psi \cdot F^2{}_{hkl})\}$ against $\sin^2\theta/\lambda^2$ using the fundamental diffraction lines.

Based above, $I^{cal.}$ is calculated by equation (8).

5. Atomic force microscope – AFM

Since FeAlSi films are studied for application as the bottom free layer in MTJ multilayers, poor surface flatness can lead to leakage paths in ultra-thin MgO insulating layers. Specifically, to maintain the flatness of the 2-3 nm thick MgO insulating layer, it is desirable for the R_a (average surface roughness) of the FeAlSi bottom free layer to be below 0.3 nm. Additionally, high roughness can cause static magnetic coupling known as orange peel coupling at the multilayer interface [80], so the smaller the roughness, the better. To evaluate the surface roughness of FeAlSi films, an Atomic Force Microscope (AFM) was used. The instrument employed was a SPA-400 by SEIKO INSTRUMENTS, operated in contact mode. This method involves contacting the cantilever with the sample, and the cantilever was Si coated with Al. The scanning area was set to 1.0×1.0 μm², and the scanning speed to 1.0 Hz. Measurements were conducted in 2-3 locations per sample, and the average of the calculated surface roughness (Ra) values was taken.

6. Vibrating sample magnetometer – VSM

For the magnetic property evaluation of FeAlSi films, a Vibrating Sample Magnetometer (VSM) from TOEI was used to measure the magnetization curves. All samples used were on 10 mm square substrates, and the magnetic field resolution was set at 0.5 Oe. However, to observe the soft magnetic reversal of Sendust in detail, the magnetic field resolution near zero field was finely set to 0.16 Oe. In this experiment, the anisotropy field (H_k) of single-crystal FeAlSi was determined from the magnetization curve when a magnetic field was applied in the hard axis direction. Specifically, H_k was defined as the intersection of the linear fitting of the magnetization rotation process in the magnetization curve and the linear part of the saturation magnetization as shown in Figure II-3. However, my experiments include some samples with good soft magnetic property with very low H_k, where the above method becomes poor accurate. In this case, I utilized the method using Ferromagnetic resonance (FMR) to determine the detailed H_k as described in the next section.

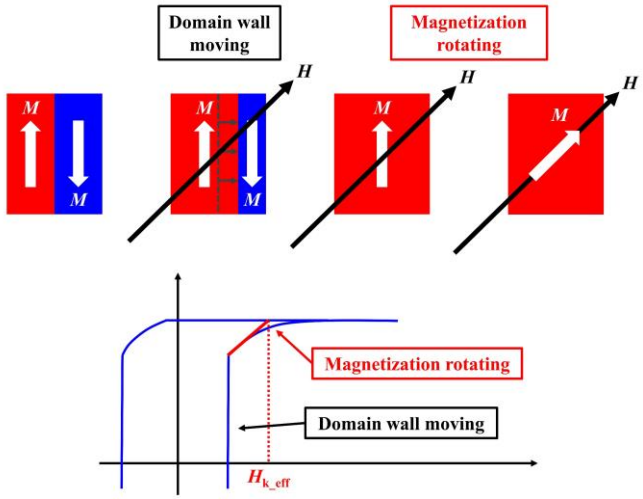

Figure II-3 Schematic diagram of the magnetization process for a single-crystal magnetic thin film with four-fold symmetric crystalline magnetic anisotropy.

7. Ferromagnetic resonance – FMR

FMR was measured to determine the exact magnetocrystalline anisotropy constant K_1. The rotating magnetic field was applied in the in-plane direction of the film (Figure II-4), and K_1 and K_u were calculated from the angular dependence of the resonant field as below, where K_1 is a cubic magnetic anisotropy constant, K_u is a uniaxial magnetic anisotropy constant, ω is the resonance frequency, and γ is a gyromagnetic ratio constant.

$$\frac{\omega}{\gamma} = \frac{1}{M_s}\sqrt{\left[M_s H_{res} + K_1\left(2 - \frac{1 - cos\,4\phi}{2}\right)\right]\left[M_s H_{res} + 2K_u\,cos\,\phi + 2K_1\,cos\,4\phi\right]} \qquad (13)$$

K_1 and K_u represent the four-fold and two-fold in-plane components of the magnetocrystalline anisotropy constant, respectively.

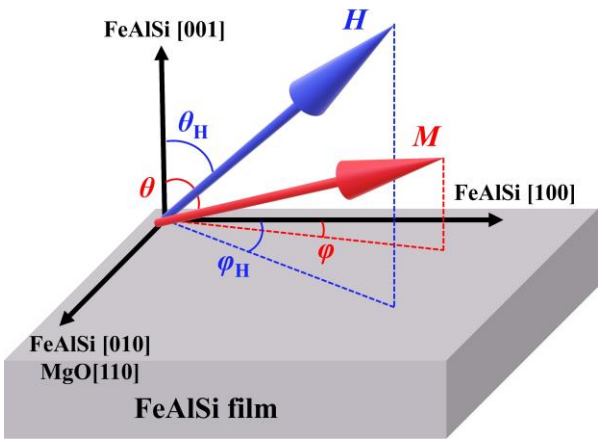

Figure II-4 FMR setup for evaluating magnetic anisotropy of FeAlSi film

Here, I'll show the calculation details for leading eq. (13) accordingly. If the external magnetic field H is in the in-plane direction ($\theta_H = \pi/2$), the energy E can be expressed by the following equation, considering Zeeman energy, in-plane uniaxial anisotropy and four-fold in-plane symmetric anisotropy,

$$E = MH(\sin\theta\cos(\phi_H - \phi)) + K_u \sin^2\phi + \frac{1}{4}K_1(\sin^4\theta\sin^2 2\phi + \sin^2 2\theta) \qquad (14)$$

Therefore, $E_{\theta\theta}$, $E_{\phi\phi}$, $E_{\theta\phi}$, $E_{\phi\theta}$ is calculated respectively as follows, where subscripts denote derivatives.

$$
\begin{aligned}
E_{\theta\theta} &= MH\sin\theta\cos(\phi_H-\phi) + K_1\left((3\sin^2\theta\cos^2\theta-\sin^4\theta)\sin^2 2\phi + 2\cos^2 2\theta - 2\sin^2 2\theta\right)\\
E_{\theta\phi} &= -MH\cos\theta\sin(\phi_H-\phi) + 4K_1\sin^3\theta\cos\theta\sin 2\phi\cos 2\phi\\
E_{\phi\theta} &= -MH\cos\theta\sin(\phi_H-\phi) + 4K_1\sin^3\theta\cos\theta\sin 2\phi\cos 2\phi\\
E_{\phi\phi} &= MH\sin\theta\cos(\phi_H-\phi) + 2K_u(\cos^2\phi-\sin^2\phi) + 2K_1\sin^4\theta\,(2\cos^2 2\phi - 2\sin^2 2\phi)
\end{aligned}
\tag{15}
$$

Furthermore, the above equation can be transformed as follows, assuming that the out-of-plane component of magnetization can be neglected ($\theta = \pi/2$),

$$
\begin{aligned}
E_{\theta\theta} &= MH\cos(\phi_H-\phi) + K_1(-\sin^2 2\phi + 2)\\
E_{\theta\phi} &= E_{\phi\theta} = 0\\
E_{\phi\phi} &= MH\cos(\phi_H-\phi) + 2K_u(\cos^2\phi-\sin^2\phi) + 2K_1(2\cos^2 2\phi - 2\sin^2 2\phi)
\end{aligned}
\tag{16}
$$

The resonance condition is expressed by the following equation, so we obtain the equation (13).

$$
\frac{\omega}{\gamma} = \frac{1}{M_s}\sqrt{E_{\theta\theta}E_{\phi\phi} - E_{\theta\phi}E_{\phi\theta}} \tag{17}
$$

8. Optical lever method

The optical lever method was used to determine the magnetostriction constant of the FeAlSi films[81]. I applied a rotating magnetic field in the in-plane direction of the films and observed the change in the reflection position of the laser beam due to the distortion of the sample caused by the inverse magnetostriction effect. The shift between the sample distortion and the laser reflection position is expressed by equation below, where $\delta l/l$ is the film distortion, d_{laser} is the laser reflection position, E is Young's modulus, t is thickness, p is the spot position, and L is the sensor position.

$$
\frac{\delta l}{l} = \frac{d_{laser}\left(E_{sub.}t_{sub.}^2\right)}{18pLt_{FeAlSi}E_{film}} \tag{18}
$$

Film strain was measured along the FeAlSi [110] direction, and then λ_{111} was calculated with equation below[82], where $a\phi$ is an offset term.

$$
\frac{\delta l}{l}_{110} = \frac{3}{4}\lambda_{111}sin2\phi + \frac{1}{4}\lambda_{100} + a\phi \tag{19}
$$

9. Magneto-optic Kerr effect – MOKE

The prepared samples were observed for magnetic domain patterns using a Kerr effect measurement device (manufactured by Neoark Corporation, model BH-782PI-TUK). White light from an OLYMPUS mercury lamp (U-RFL-T) was irradiated onto the measurement samples. The current was controlled using a programmable AC power supply from NF Circuit Design Block Company, through a control unit (MG CONT UNIT), and a magnetic field was generated by Helmholtz coils. The reflectance in response to the magnetic field was measured using an OLYMPUS objective lens unit (U-CMAD3), and magnetic domain observation was performed.

This apparatus measures the longitudinal Kerr effect and can observe in-plane magnetic domain structures. The external magnetic field was applied in the direction of the hard axis of magnetization of the free layer, and the observation was made. The reference image was captured at an applied field of 50 Oe, and the measured data was saved after automatic adjustment of brightness and contrast.

10. Brillouin Light Scattering – BLS

BLS was conducted following the previous work[83] as shown in Figure II-5, where a laser with a wavelength of λ = 532 nm was projected onto the surface at an angle θ from the surface normal, in a plane perpendicular to the external field H. The in-plane component of the magnon wave vector is oriented along the y-axis, and its wave vector transfer is represented as $k = (4\pi/\lambda) \sin\theta$ [84]. The BLS results are affected by the Dzyaloshinskii-Moriya interaction (DMI) [85–87], which is also the first investigation for FeAlSi films by this study. I conducted two types of BLS measurements: H = 0.2 - 0.6 T with θ = 0°, and θ = 0 - 45° with H = 0.2 T. I can determine A based on those two measurements and the following equations:

$$f_{DE} = \frac{\mu_0 \gamma}{2\pi} \sqrt{H\left[H + H_{k_{eff}}\right] + \left(\frac{M_s t}{2t}\right)^2 (1 - \exp(-2kt))} \pm \frac{2\gamma}{2\pi M_s} Dk \tag{20}$$

$$f_{PSSW} = \frac{\mu_0 \gamma}{2\pi} \sqrt{\left[H + \frac{2At}{\mu_0 M_s t}\left(k^2 + \left(\frac{n\pi}{t}\right)^2\right)\right]\left[H + \frac{2At}{\mu_0 M_s t}\left(k^2 + \left(\frac{n\pi}{t}\right)^2\right) + H_{k_{eff}}\right]} \tag{21}$$

Where, f_{DE} and f_{PSSW} are frequencies of Damon-Eshbach (DE) mode and Perpendicular Standing Spin Wave (PSSW) mode respectively, γ: gyromagnetic ratio, H: external field (in-plane), M_s: saturation magnetization, H_{k_eff}: effective out-of-plane anisotropy field, D: DMI constant. The fitting parameters were $\gamma/2\pi$ (GHz/T), $\mu_0 H_{k\_eff}$ (T), A (pJ/m) and t, where t was included to determine the thickness of FeAlSi exactly. The sample for BLS was also measured by VSM to determine the M_s for the prepared sample.

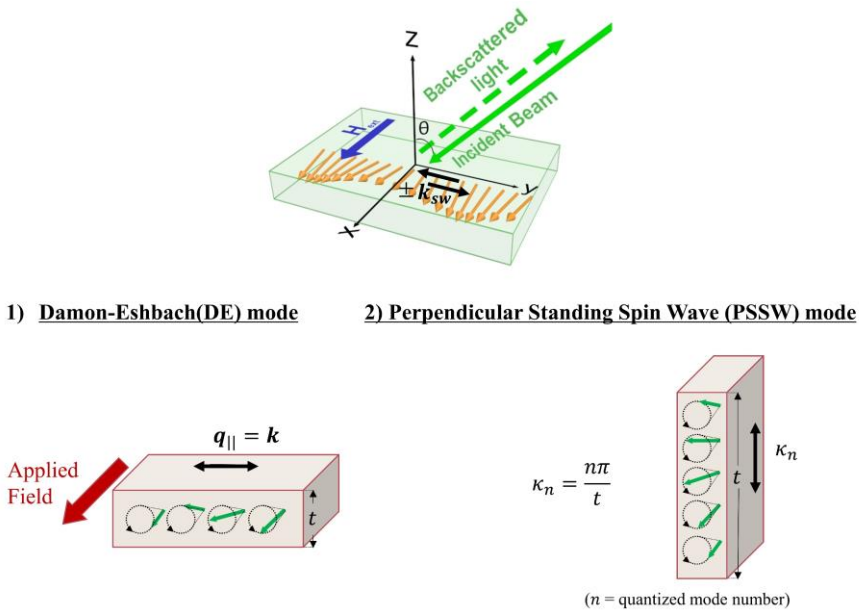

Figure II-5 BLS setup

11. Four probe method

I utilized the MODEL: TKSPS-122H (commonly known as the Semi-Auto Prober), which is capable of automatically controlling the probe position and automatically measuring the magnetoresistance effect of each MTJ using four probe method, with an applicable magnetic field of up to approximately 2000 Oe. For the power supply, a KEYSIGHT Precision Source/Measure Unit (B2900A) was used to apply and measure direct current. The same device was also used as a voltmeter, setting the applied voltage at 10 mV. Additionally, a Helmholtz coil circuit by TOEI Scientific Industrial inc. was used to generate the magnetic field, with a bipolar power supply also from TOEI. The magnetic field strength at the time was calculated from the voltage using a Hall element placed beneath the probe, with an DC voltage/current generator, using MODEL 3001 by ADCMT. Furthermore, a CCD camera was used for aligning the position of the MTJ sensors, and a program corresponding to the mask used in photolithography was designed to automatically control the position and carry out measurements via computer. The applied magnetic field was set at 1500 Oe, with a step of 0.1 Oe.

12. Physical Properties Measurement System – PPMS

I used Physical Property Measurement System (PPMS) by Quantum Design Inc. for the measurements of TMR properties at low temperature. All equipment is controlled through a program written in LabVIEW. To improve the signal-to-noise ratio performance, the signal is pre-processed through a preamplifier (SR560 by NF Corporation) and then inputted into a lock-in amplifier (LI5655 by NF Corporation).

III. Magnetic property of FeAlSi film

1. Sample preparation

As mentioned in introduction, the soft magnetic property of FeAlSi is so sensitive to the composition. Based on this, I prepared samples with five different compositions as summarized in Figure III-1. The composition of prepared FeAlSi thin films measured by inductively coupled plasma (ICP) spectrometry.

The stacking structure to investigate the film properties of FeAlSi is shown in Figure III-2, where FeAlSi is expected to grow on MgO buffer epitaxially.

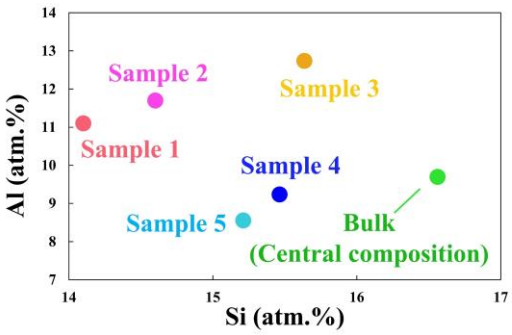

(atm.%)	Al	Si
Sample 1	11.1	14.1
Sample 2	11.7	14.6
Sample 3	12.8	15.6
Sample 4	9.2	15.5
Sample 5	8.6	15.2

Figure III-1 FeAlSi compositions in this study

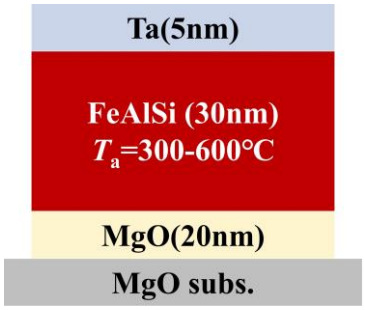

Figure III-2 Stacking structure for film properties investigation.

2. Structural analysis

① Crystal structure

I found that all samples showed similar behaviors, so Figure III-3 show the typical results for Sample 1. (Other results are shown in Figure III-5, Figure III-6.) In Figure III-3 (a), we can clearly observe the FeAlSi peaks, which shows nm-order FeAlSi films were successfully fabricated on MgO in (001)-orientation. In Figure III-3 (b), FeAlSi (111) $D0_3$ peaks are observed in addition to FeAlSi (222) B2 peaks and FeAlSi (444) A2 peaks. I firstly prepared the nm-order FeAlSi with $D0_3$ ordered structure. Figure III-4 shows the ϕ scan for the (111) $D0_3$ peaks, where we can clearly confirm the ideal epitaxial growth of FeAlSi on MgO according to the 45-degree peak shift of FeAlSi compared to MgO.

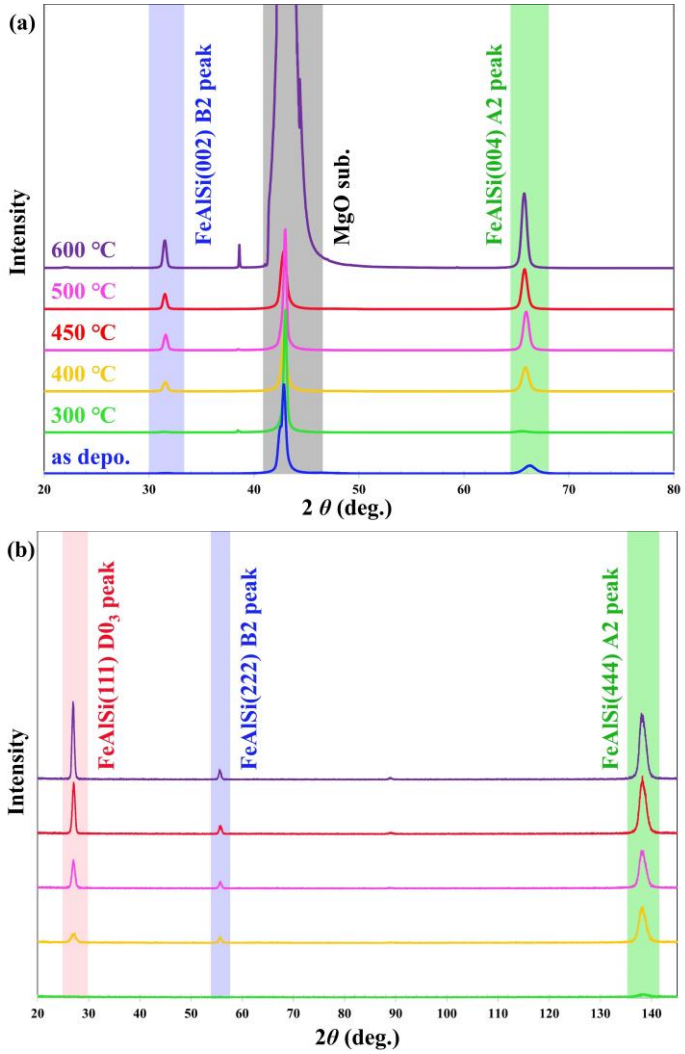

Figure III-3 XRD 2θ-θ scan for (a) (001)-plane and (b) (111)-plane

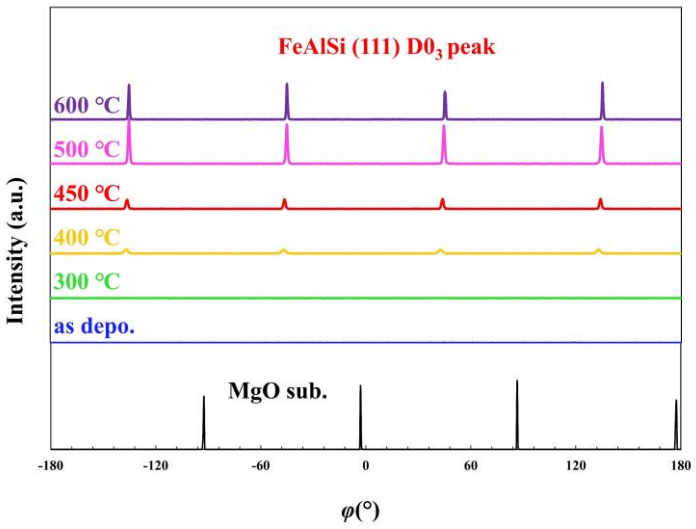

Figure III-4 XRD ϕ scan for (111)- D0$_3$ peak

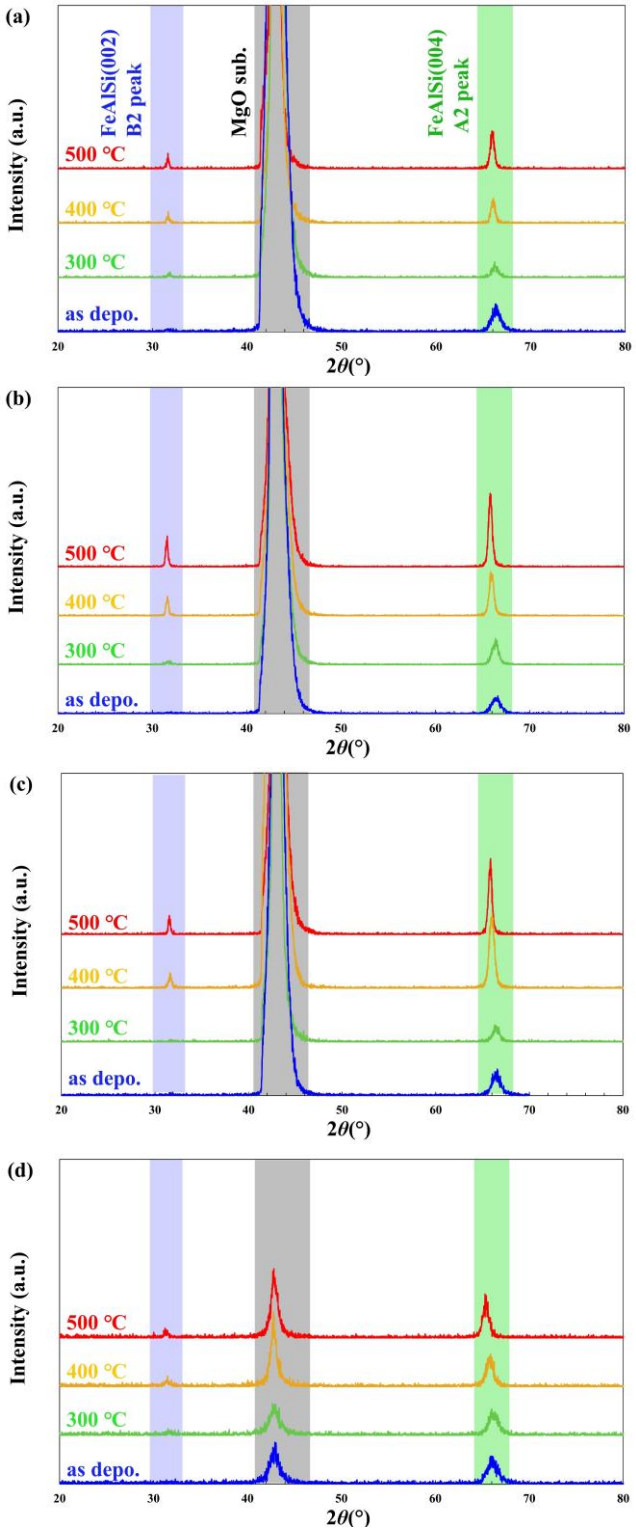

Figure III-5 Other 2θ-θ scan results for (a) Sample 2 (b) Sample 3 (c) Sample 4 (d) Sample 5

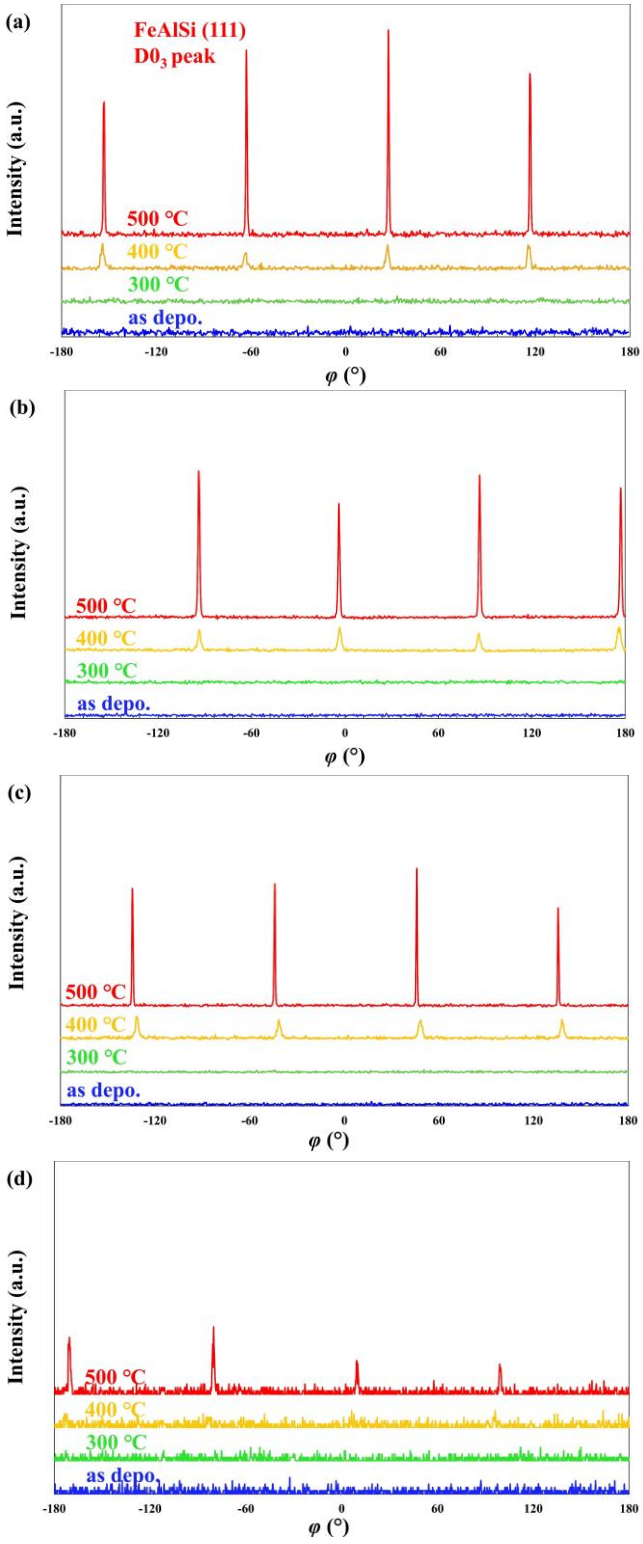

Figure III-6 Other ϕ scan results for (a) Sample 2 (b) Sample 3 (c) Sample 4 (d) Sample 5

② Surface structure

The dependence of R_a on T_a for each composition sample is shown in Figure III-7. For most samples, R_a values were observed below the target value, indicating that the films are sufficiently flat for the application in MTJs. Additionally, AFM images for each composition are shown in Figure III-8. No significant differences were observed due to composition, and it was confirmed that the films were generally flat.

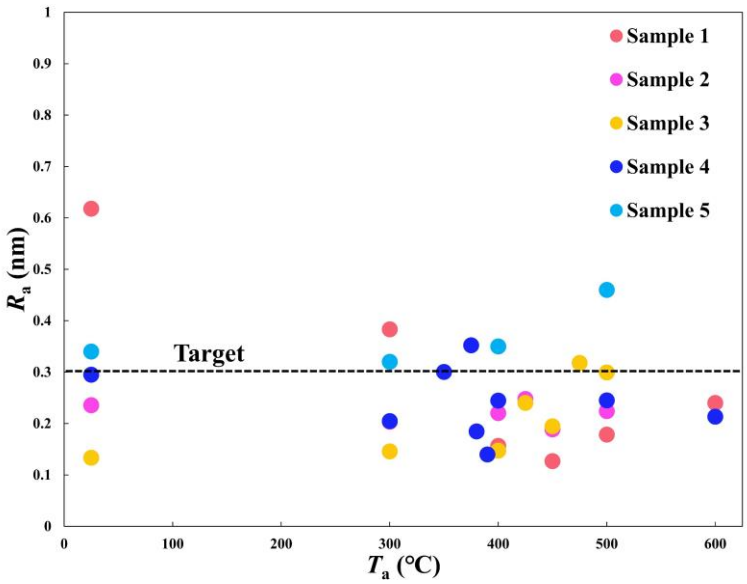

Figure III-7 T_a dependence of R_a for various sample with different compositions

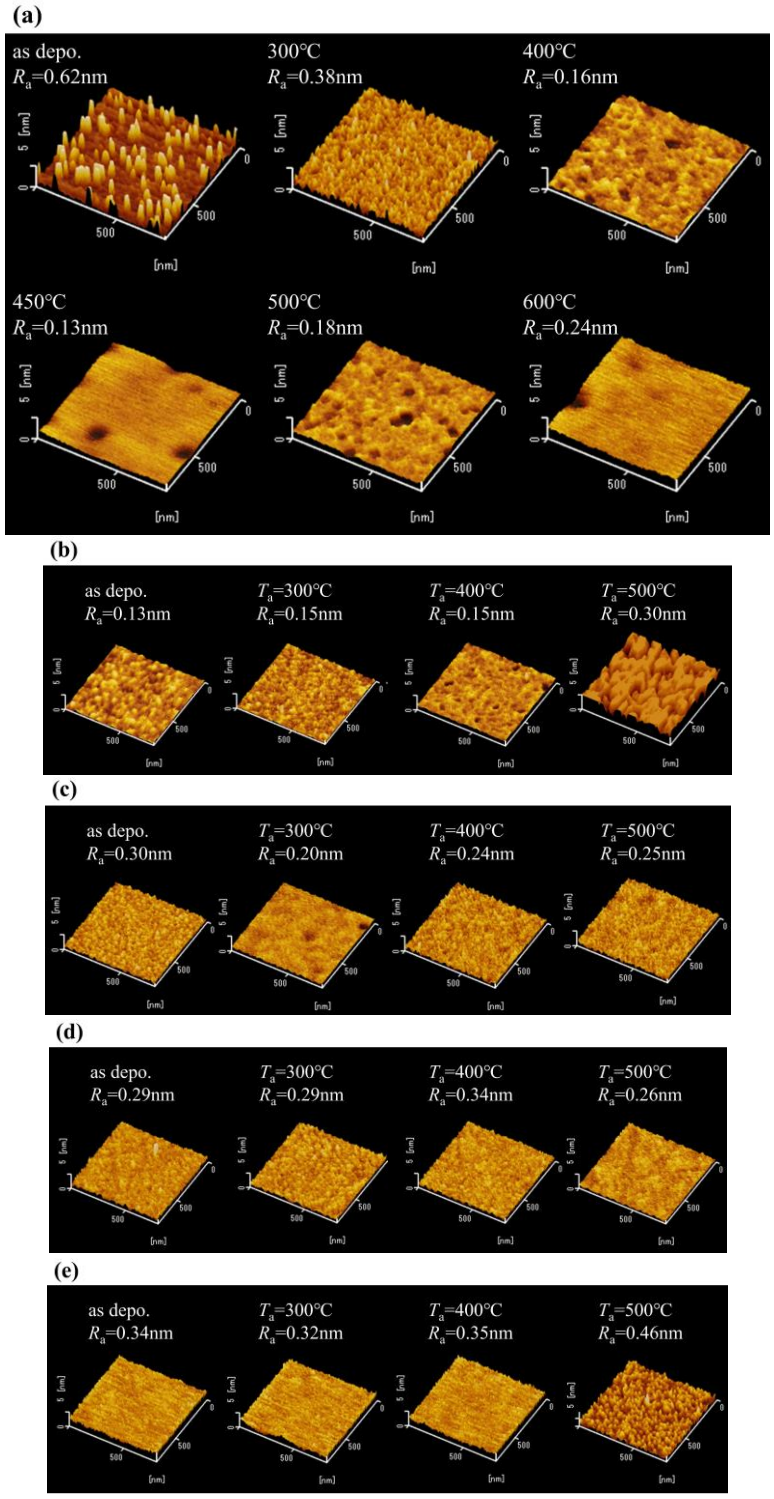

Figure III-8 AFM images of samples with each composition: (a) Sample 1 (b) Sample 2 (c) Sample 3 (d) Sample 4 (e) Sample 5

3. Static magnetic property

① Magnetization curve

Figure III-9 shows the dependence of magnetization curves on the annealing temperature, measured by VSM, with the results for Sample 1 presented as a typical example. (Results for other compositional samples are shown in Figure III-11.) The two-stage behavior of the magnetization curves of the prepared samples is considered to be due to phase separation, which becomes uniform with annealing process. Variations in composition and atomic ordering might have caused the phase separation, where further investigation is needed. A inset of the magnetization curves with a smaller scale has been added, limited to those with small anisotropy.

In Figure III-9, it is important to note that as the annealing temperature increases, the magnetic easy axis changes. Specifically, below 400°C, the [100] direction is the easy axis, while above 500°C, it is the [110] direction. This indicates a change in the sign of the magnetic crystalline anisotropy constant K_1 from positive to negative, with K_1 approaching zero around 450°C. The reversal of the sign of K_1, observed with annealing in Al-rich samples 1, 2 and 3, implies that the composition of Al is crucial to achieve K_1=0 in FeAlSi films. I'll thoroughly discuss this point later. In Al-rich samples, the annealing temperature at which K_1 approaches zero slightly varies between 400 to 450°C, indicating that both the sign of K_1 and the temperature at which it changes are dependent on the film's composition.

Figure III-10 shows the T_a dependence of H_k for all samples of different compositions as estimated from the magnetization curves, where K_1 behavior is described with H_k as below.

$$\boldsymbol{K_1 = \frac{H_k M_s}{2}} \tag{22}$$

It revealed that H_k reaches a minimum around 400-450°C for samples 1, 2, and 3. In contrast, for samples 4 and 5 (films with less Al), no K_1=0 was observed. The lowest H_k value, less than 1Oe, was found in Sample 3, which is comparable to other soft magnetic materials like NiFe or CoFeSiB.

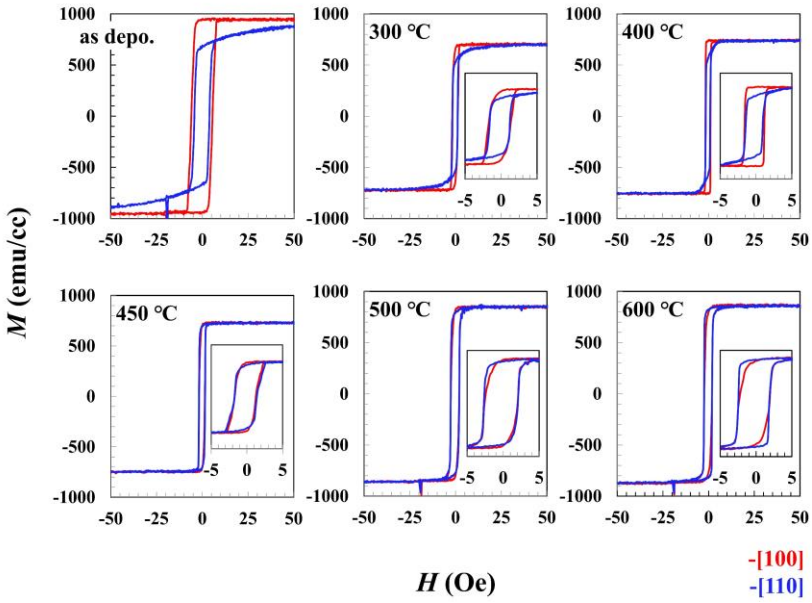

Figure III-9 VSM curve for typical result of Sample 1

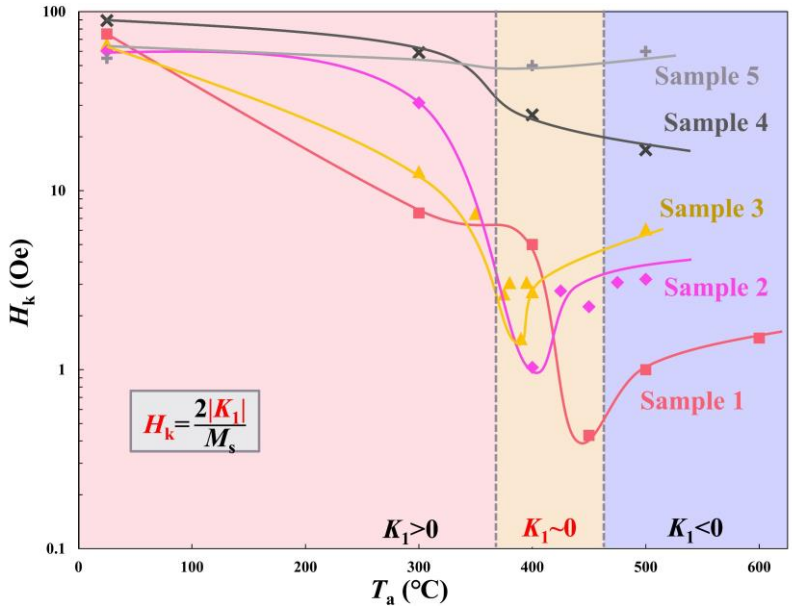

Figure III-10 T_a dependence of H_k for all samples

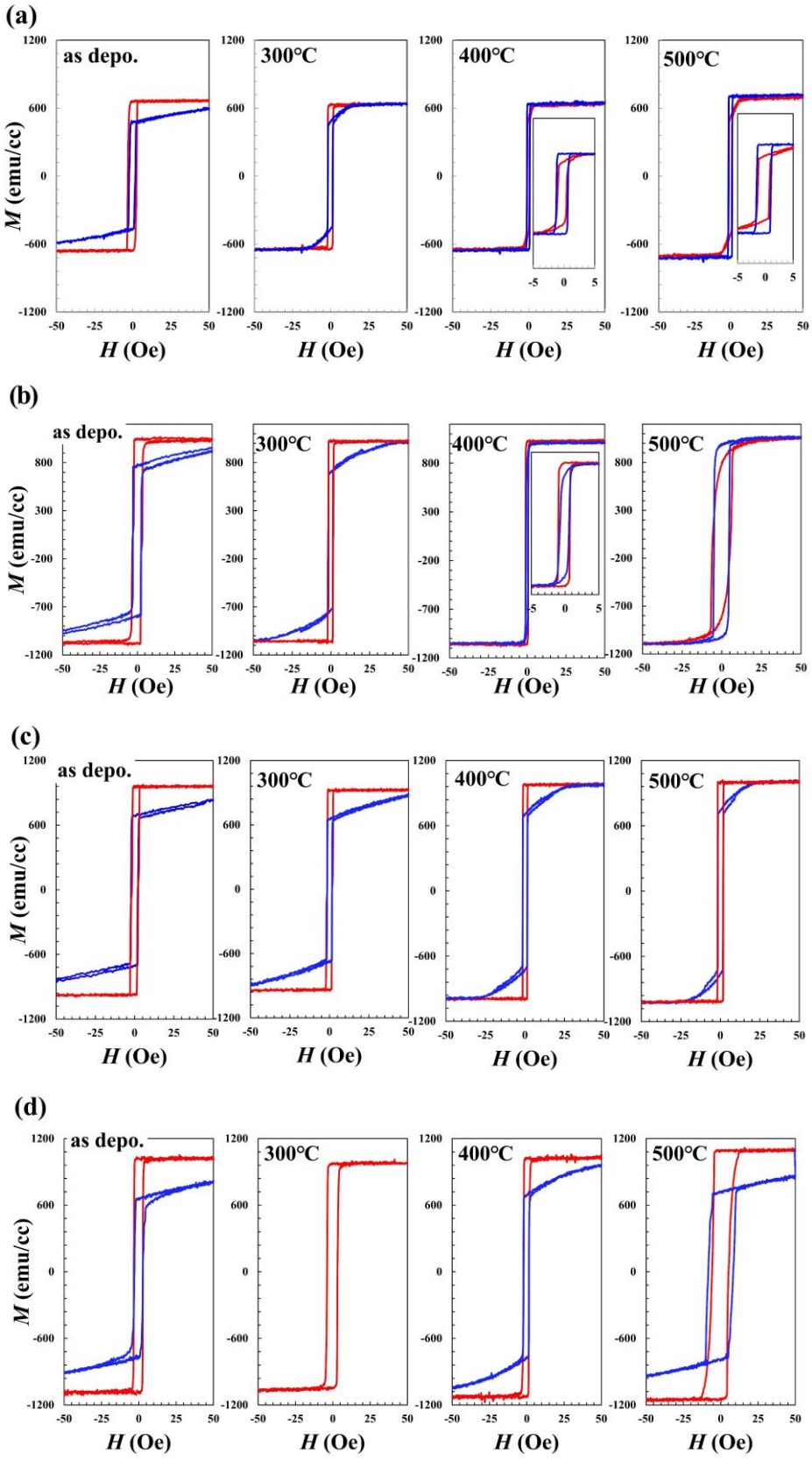

Figure III-11 VSM curve for other samples of Sample 2-5

② Magnetic anisotropy by FMR

Using Sample 1 (T_a = 450°C), which showed optimal soft magnetic properties in VSM measurements, I further clarified the magnetic properties of the FeAlSi film.

Figure III-12 illustrates the in-plane angular dependence of the resonance field in FMR. It was confirmed that the variation in the resonance field is dominated by the four-fold component of the epitaxial thin film, with a very small contribution from the uniaxial component. The fitted parameter values were $K_1 = 1.6\times10^2$ [erg/cc], $K_u = 10$ [erg/cc], and $\omega/\gamma = 88.5$ [Oe]. The observed K_1 value is similar to that of bulk FeAlSi in previous studies[88], indicating that we have successfully fabricated nm-scale FeAlSi films with desirable soft magnetic properties. The precise value of H_k was very small (0.43 Oe), suggesting that the soft magnetic property of the prepared FeAlSi film is superior to that of other typical soft magnetic materials such as NiFe or CoFeSiB.

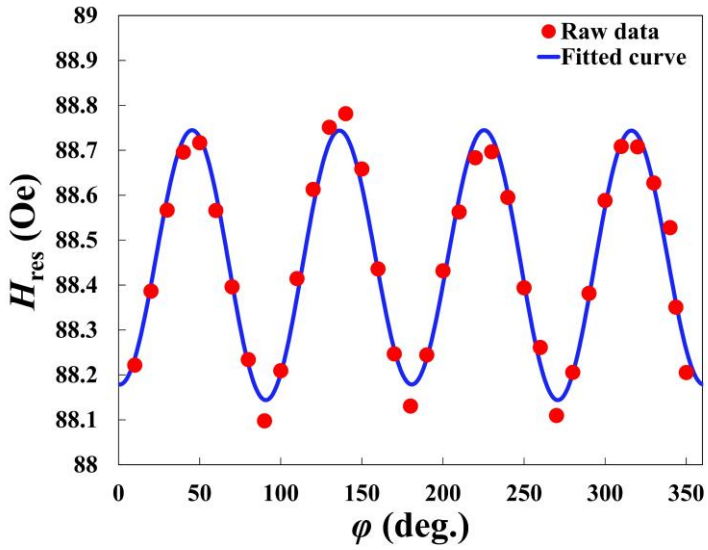

Figure III-12 FMR results for typical result of Sample 1

③ Magnetostriction

I discuss the uniaxial magnetic anisotropy constant K_u previously mentioned in FMR. Uniaxial strain generated in the plane of the epitaxial film during its fabrication may have caused uniaxial magnetic anisotropy as a result of magnetostriction. This hypothesis is plausible, as mentioned in the introduction, where not only K_1 but also magnetostriction is a crucial factor affecting the soft magnetism of FeAlSi. To investigate this, magnetostriction constants and crystal strain were evaluated using the optical lever method and in-plane reciprocal space mapping (RSM), respectively, and the following equation was used to estimate the magnetic anisotropy constant due to magnetostriction, where σ is the strain in the film:

$$\boldsymbol{K_u = \frac{3}{2} E_{FeAlSi} \lambda \sigma} \tag{23}$$

Figure III-13 shows the angular dependence of $\delta l/l_{110}$ measured by the optical lever method. The results for Sample 2 (T_a = 400 °C) are shown as a typical example. The calculated λ_{111} is 3.53×10^{-7}, similar to the value in bulk (10^{-7})[89]. Figure III-14 shows the in-plane RSM results for Sample 2 at T_a = 400 ℃. Epitaxial growth of the FeAlSi film and the in-plane strain calculated from the positions of the (100) and (010) peaks were observed. The 2θ peak positions of the (100) and (010) planes measured by in-plane RSM were 64.965 degrees and 64.957 degrees, respectively, and the lattice constants were determined as a_{100}=5.7355Å and a_{010}=5.7357Å using the following Bragg's equation:

$$\boldsymbol{\frac{2a}{\sqrt{h^2 + k^2 + l^2}} \sin\theta = \lambda} \tag{24}$$

Here, a is the lattice constant, h, k, l are Miller index, and λ is the wavelength of the X-ray.

Next, the film strain was calculated using the following equation, and the calculated value was $\sigma = 2.06 \times 10^{-5}$:

$$\begin{aligned} \boldsymbol{\sigma} &= \boldsymbol{\frac{\Delta a}{a_{110}}} \\ \boldsymbol{\Delta a} &= \boldsymbol{a_{110} - \frac{a_{100} + a_{110}}{2}} \end{aligned} \tag{25}$$

The K_u value calculated using the above equations is 20.3 [erg/cc], which is almost the same as the uniaxial component of magnetic anisotropy constant in FMR. Thus, I conclude that the in-plane uniaxial magnetic anisotropy in FeAlSi films is due to magnetostriction, and its contribution to the total magnetic anisotropy is small. Therefore, the four-fold symmetric magnetic crystalline anisotropy constant K_1 is dominant in the magnetic anisotropy of FeAlSi films.

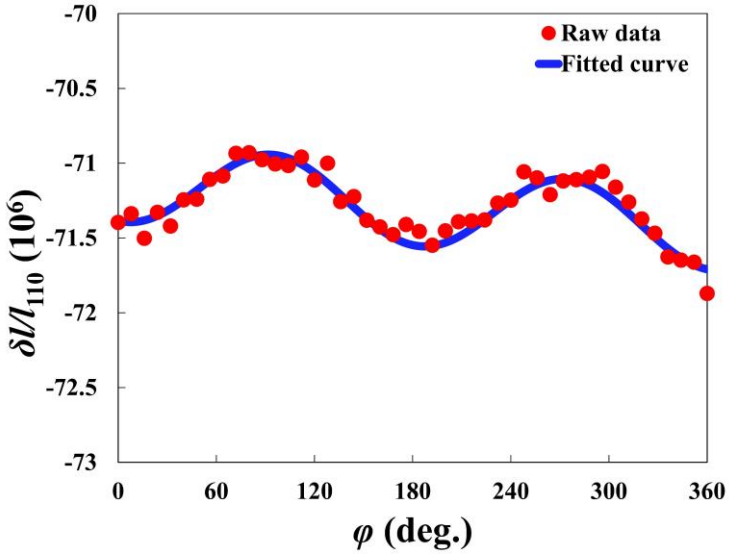

Figure III-13 Optical method result for prepared Sample 2

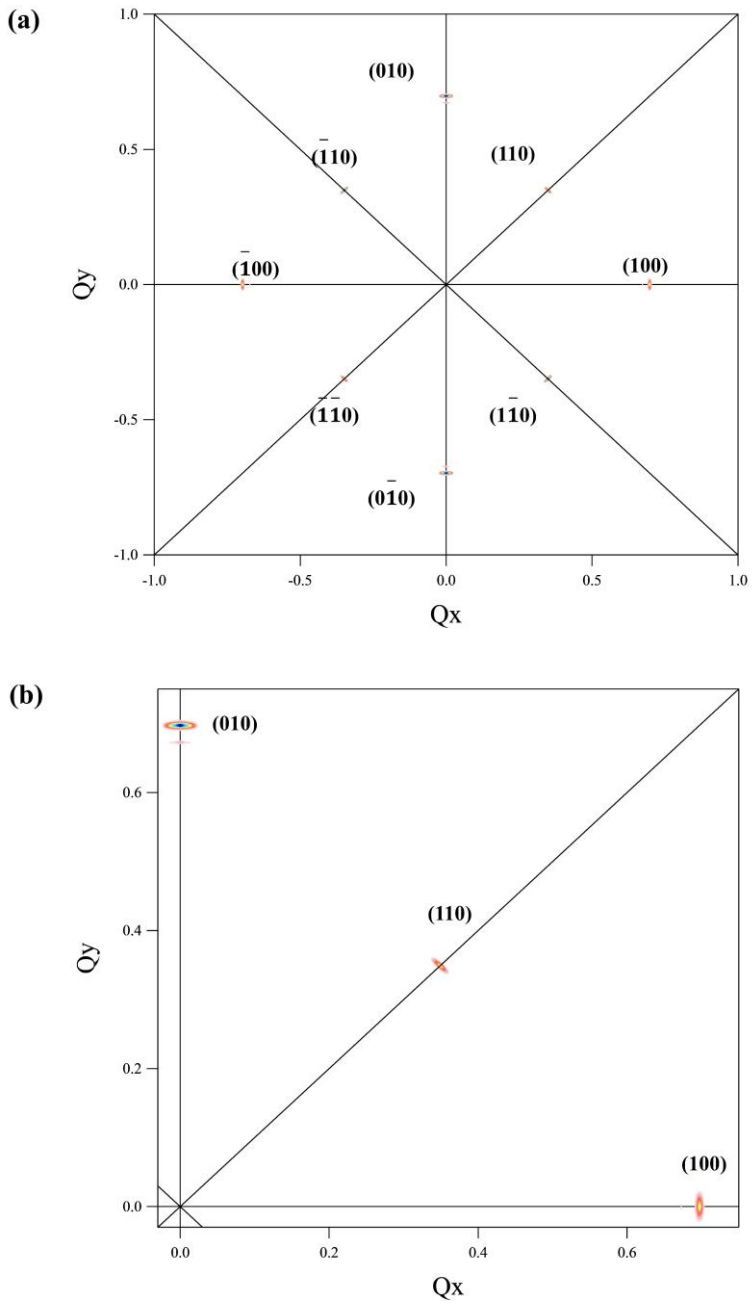

Figure III-14 RSM result for prepared Sample 1

4. Discussion of soft magnetic property

① The origin of soft magnetic property

The reversal of the sign of K_1 was observed only with Al-rich samples 1, 2 and 3, which implies that the composition of Al is crucial to achieve K_1=0 in FeAlSi films. I'll thoroughly discuss this point. In the first place, the soft magnetic property for FeAlSi is achieved with the compatibility of two factors: Sendust central composition and $D0_3$-ordered structure as described in introduction.

First, I conducted the composition analysis, and the result is shown in Figure III-15. The important point is that $K_1 \sim 0$ was only observed in Sample 1, 2 and 3, which is deviated from Sendust central composition. On the other hand, Sample 4 and 5 didn't show the $K_1 \sim 0$, which are close to the Sendust central composition. This result is inconsistent with the previous work of bulk. Next, I investigated the degree of $D0_3$ order (S_{D03}) for samples which showed $K_1 \sim 0$. The behaviors of S_{D03} increase with T_a increase for all samples are almost same. However, the S_{D03} with $K_1 \sim 0$ for all samples are different, and those S_{D03} were also different from bulk of 100%. This result is also inconsistent with introduction that perfect $D0_3$-ordered structure needs to be achieved for soft magnetic property. In summary, the film samples in this study achieved ideal soft magnetic properties despite that the compatibility of Sendust central composition and $D0_3$-ordered structure are not realized. For understanding this reason, I'll introduce the sub-structure model consisting of FeAlSi.

Figure III-17 shows the diagram of sub-structure model for FeAlSi. First, a previous work showed that the soft magnetic properties of FeAlSi can be understood with the mixed structure of $D0_3$-Fe_3Si and $D0_3$-Fe_3Al [88]. Here, these two structures have different signs of K_1, so net-$K_1 \sim 0$ is achieved with the mixing these structures with the ratio of Sendust central composition. Then, I'll extend this idea for the results in this study of film-FeAlSi. Film-FeAlSi also has disordered structures including B2-Fe_3Si, B2-Fe_3Al and A2-FeAlSi, which leads the complication of estimating net-K_1 [88,90]. To simplify this problem, I focused on $D0_3$-Fe_3Al, which is the unique phase with negative K_1 as shown in Table III-1.

Figure III-18 summarized the results of K_1-samples with the relationship between S_{D03} and Al composition (at. %), where I supposed that the rate of $D0_3$-Fe_3Al is qualitatively described as S_{D03} × Al composition (at. %). This diagram clearly shows us the inverse proportions of S_{D03} and Al composition (at. %), which means the soft magnetic property in FeAlSi is achieved with the same rate of $D0_3$-Fe_3Al. This fact can be intuitively understood as that the Al composition in film (including disordered structure) needs to be richer than that of bulk (perfect $D0_3$-ordered structure), considering the Al atoms in disordered structures. Based on this discovery, the Sendust central composition for film is expanded compared to bulk as shown in Figure III-19. In other words, for nm-order FeAlSi films, soft magnetic property can be easily achieved by controlling the film composition and atomic ordering while varying the composition of the sputtering target and the annealing temperature. Further investigation about composition dependence in future works would be useful because the plotted data in my study is obviously insufficient. Our findings should be useful for the application of FeAlSi films with optimal soft magnetic properties to highly sensitive TMR sensors.

I'll move on to the more detailed investigation, which considers all sub-structures. We can estimate each volume fraction as described in Figure III-20, where I used the equation below (w is the composition ratio (at. %)).

$$\begin{aligned} \boldsymbol{K_1} = \boldsymbol{S_{D03}} \times \left[\boldsymbol{K_{1_{Fe_3Al(D0_3)}}} \times \frac{\boldsymbol{w_{Al}}}{\boldsymbol{w_{Al}+w_{Si}}} + \boldsymbol{K_{1_{Fe_3Si(D0_3)}}} \times \frac{\boldsymbol{w_{Si}}}{\boldsymbol{w_{Al}+w_{Si}}} \right] \\ + \boldsymbol{S_{B2}} \times \left[\boldsymbol{K_{1_{Fe_3Al(B2)}}} \times \frac{\boldsymbol{w_{Al}}}{\boldsymbol{w_{Al}+w_{Si}}} + \boldsymbol{K_{1_{Fe_3Si(B2)}}} \times \frac{\boldsymbol{w_{Si}}}{\boldsymbol{w_{Al}+w_{Si}}} \right] \\ + \boldsymbol{S_{A2}} \times \boldsymbol{K_{1_{FeAlSi(A2)}}} \end{aligned} \tag{26}$$

Then, I can lead simulation lines of K_1 behavior as a function of Al concentration shown in Figure III-21, where experimental values are also plotted in the same figure. Here, we can clearly confirm that the $K_1 \sim 0$ points for experiment and simulation (× marks) are consistent. In other words, the behaviors of Al increase with S_{D03} decrease for both experiments and simulations are similar. This fact proves that the sub-structure model is a good method for understanding the soft magnetic properties of FeAlSi alloy.

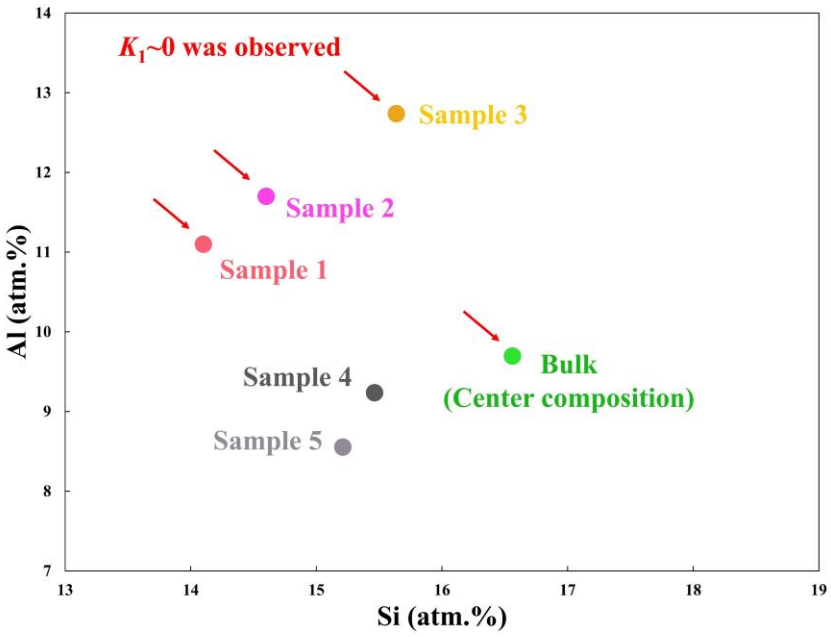

Figure III-15 Composition analysis for all samples

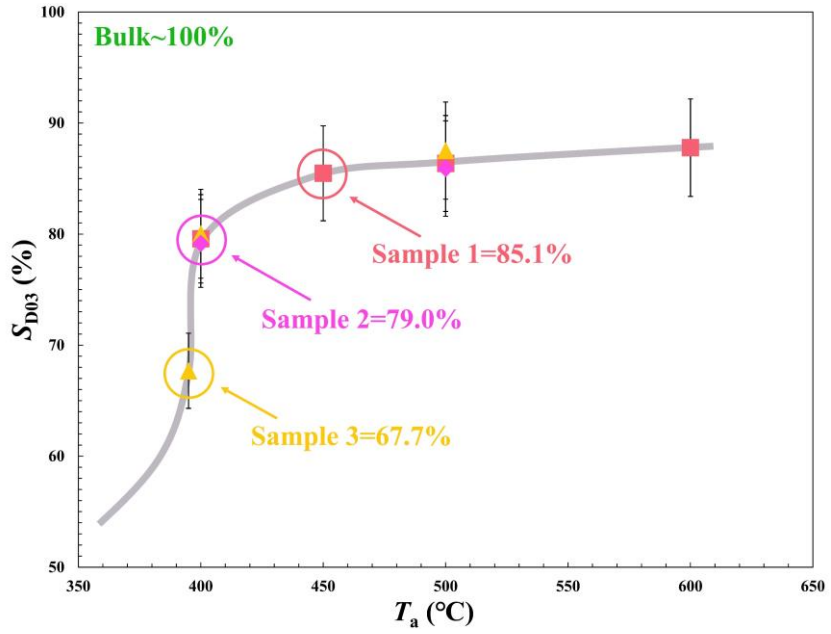

Figure III-16 Degree of $D0_3$ order for Sample 1, 2, 3 and Bulk.

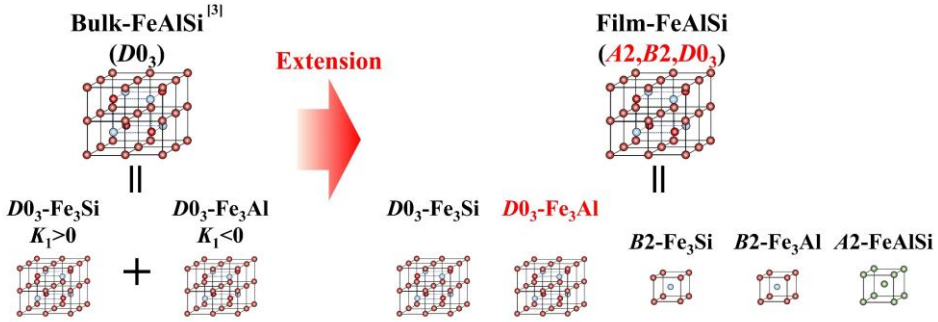

Figure III-17 Sub-structure model consisting of FeAlSi.

Table III-1 K_1 for sub-structures based on previous works.

Structures	$D0_3$-Fe_3Si	$D0_3$-Fe_3Al	B2-Fe_3Si	B2-Fe_3Al	A2-FeAlSi
K_1(10^4erg/cc) @ RT	6	-10	5	9	3.5

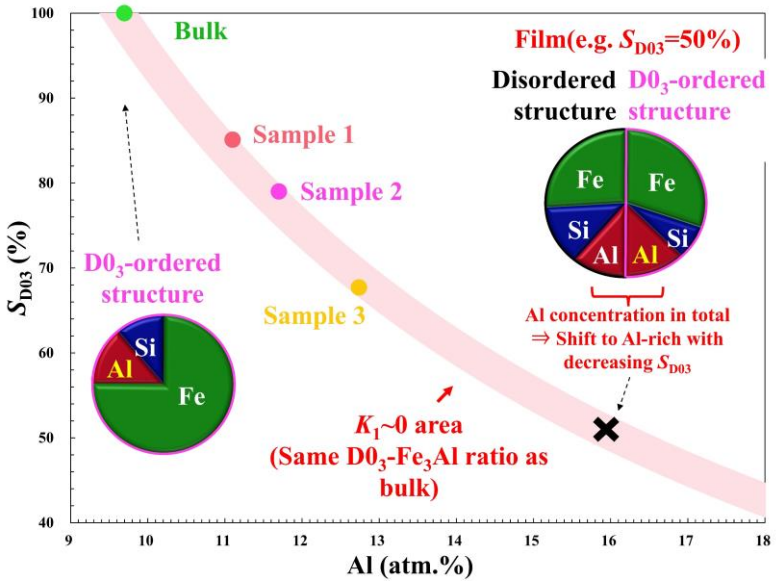

Figure III-18 Mechanism for soft magnetic property of FeAlSi.

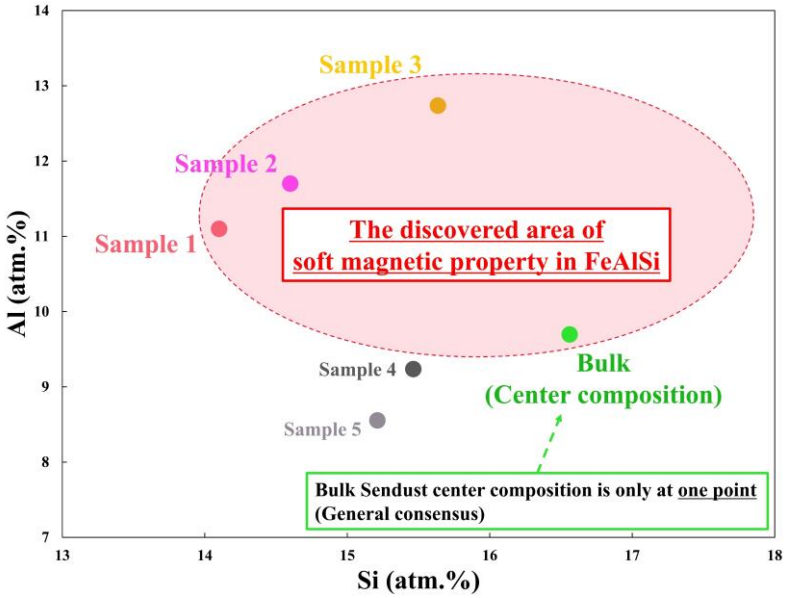

Figure III-19 Expanded composition area of Sendust

	High	S_{D03}		Low
	Bulk	Sample1	Sample2	Sample3
S_{D03}	100%	85.1%	79.0%	67.7%
S_{B2}	100%	89.4%	93.4%	90.3%
$V_{D03} = S_{D03}$	100%	85.1%	79.0%	67.7%
$V_{B2} = S_{B2} - S_{D03}$	0%	4.3%	14.4%	22.6%
$V_{A2} = 100 - S_{B2}$	0%	10.6%	6.6%	9.7%

Figure III-20 Volume estimation using S_{D03} and S_{B2}

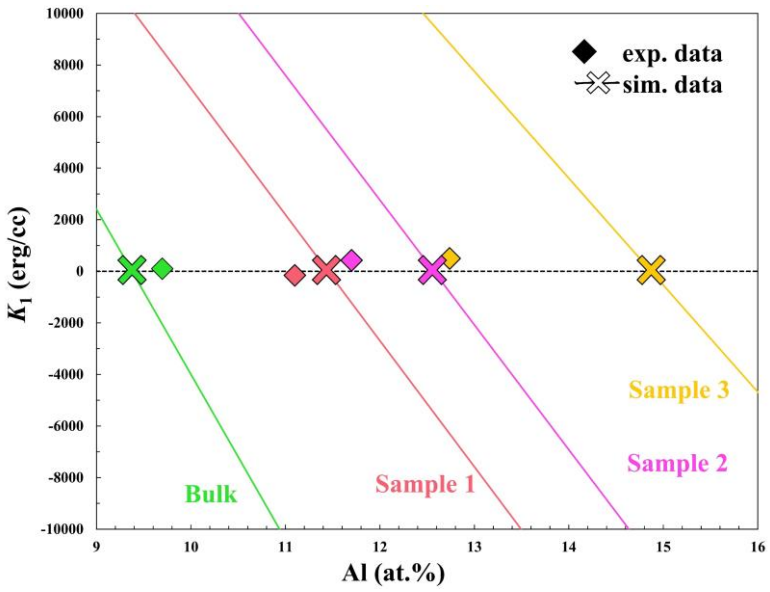

Figure III-21 K_1 comparison between sub-structure estimation and experimental results

② Magnetic domain by MOKE

I've already explained the origin of soft magnetic properties in FeAlSi film, which is mainly affected by magnetocrystalline anisotropy. The important point was that the whole magnetic anisotropy is described by the mixed structure of some kinds of sub-structures.

To understand this discovery more deeply, I conducted MOKE measurement. The left image in Figure III-22 shows the typical MOKE results for Sample 1 annealed at $T_a = 400$ °C ($K_1 > 0$), where the contrasts correspond to the directions of magnetizations. The red and blue notes show that the direction of applying magnetic field is [100] (= easy axis) and [110] (= hard axis), respectively. The behavior of contrasts is shown in the right image of Figure III-22, which has good agreement with the results of VSM. Figure III-23 shows the results with other T_a, where MOKE shows the K_1 sign reversal similar to VSM (extracted from Figure III-9).

Figure III-24 shows the MOKE results for Sample 1 annealed at $T_a = 450$ °C with ideal soft magnetic property in VSM, where applying magnetic field [110]. Interestingly, the MOKE image shows a separation into easy axis-like areas (which means $K_1 < 0$) and hard axis-like areas (which means $K_1 > 0$). As a result of the phase separation, an overall $K_1 \sim 0$ is realized. The separation into different K_1 areas suggests that the composition and atomic ordering are not uniform in whole area of the FeAlSi films. Further detailed analyses are needed for clarifying this point.

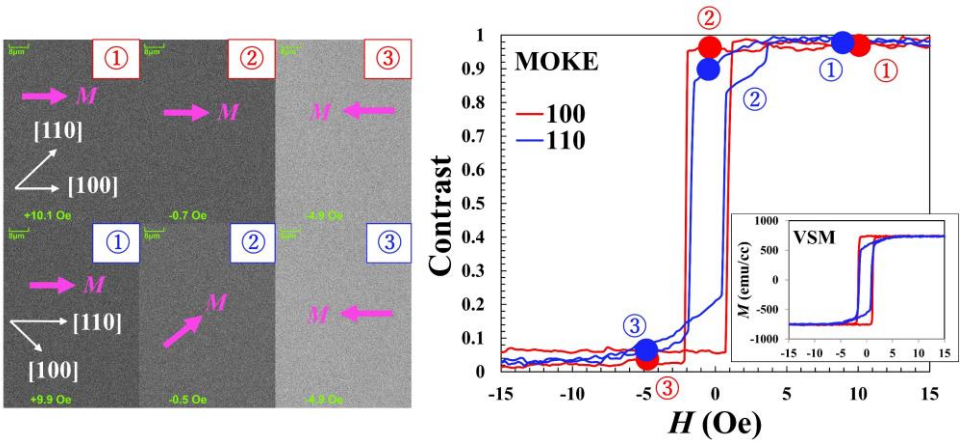

Figure III-22 Typical MOKE image

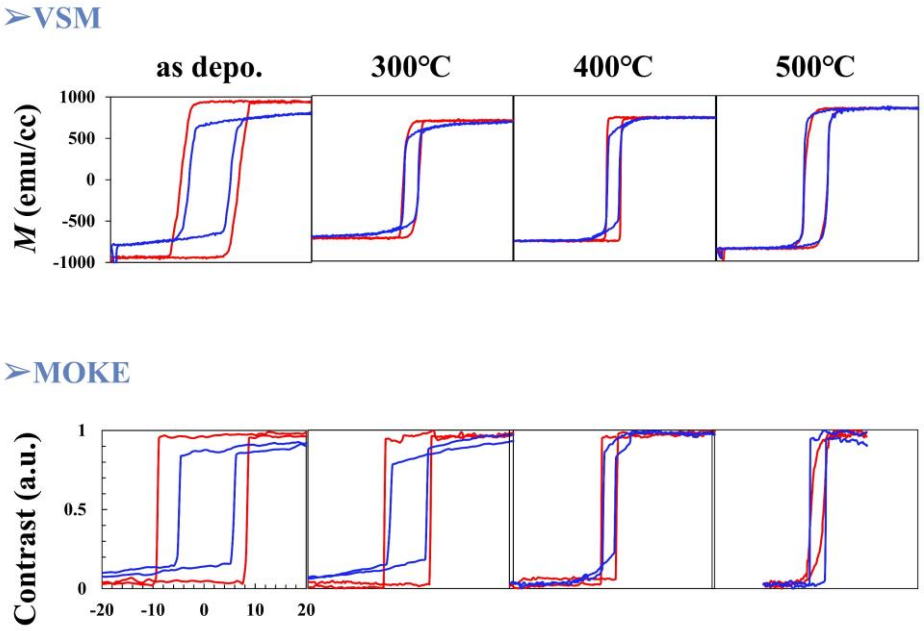

Figure III-23 Magnetization reversal in VSM and MOKE

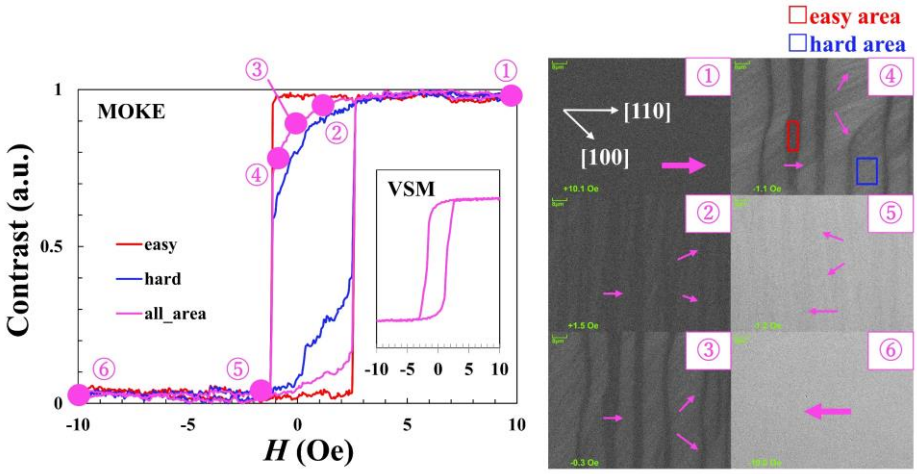

Figure III-24 MOKE and VSM for $K_1 \sim 0$ sample (Sample 1, T_a = 450°C)

5. Dynamic magnetic property – Exchange stiffness constant by BLS

Exchange stiffness constant (A) of FeAlSi film has not been studied previously, and it affects TMR ratio at RT[91]. I adopted BLS, which is promising method for identifying A. The stacking for BLS measurements was as follows: MgO (001)-substrate/MgO(20)/FeAlSi(10) T_a = 400 °C/Ta(5). The composition of FeAlSi was Sample 2. I've already confirmed that the sample showed good soft magnetic property as shown in Figure III-25.

Figure III-26 shows the results of BLS measurements for the prepared FeAlSi film, where I clearly observed the DE and PSSW mode peaks. We can only find the PSSW mode (n=1) because PSSW modes (n≧2) are too weak because the thickness of the sample is too thin (10 nm). Both peaks of DE and PSSW modes increase with higher H in Figure III-26 (a), whereas almost only DE mode peak increase with higher θ (k) in Figure III-26 (b), as theoretically predicted as shown in equations (20) and (21). Figure III-26 (c) shows k dependence of Δf_{DE}, which is the difference between the Stokes (S) peak (negative frequency) and anti-Stokes (AS) peak (positive frequency) defined by below:

$$\Delta f_{DE} = f_{AS} - f_S = \frac{2\gamma}{\pi M_s} Dk \tag{27}$$

I tried the fitting of raw data using this equation. The calculated D is 4.5 ± 1.9 [μJ/m^2], which suggests negligible DMI values because of small value with relatively large error. This result corresponds that we couldn't observe a linear behavior in Figure III-27. Therefore, I conclude that there is no DMI in FeAlSi films.

Since there is no difference between the Stokes peak and the anti-stokes peak, I summarized only the Stokes peaks dependence on H and k in Figure III-28 (a) and (b) respectively. We fitted both DE mode peaks and PSSW mode peaks using the equation (20) and (21) and determined the film thickness and various magnetic constants (Table III-2). We can confirm the reasonable thickness of 9.95 nm comparable to that determined during film growth, which means my fittings are successful. The identified A for FeAlSi is 14.3 (pJ/m), which is the first time determination of A of FeAlSi film.

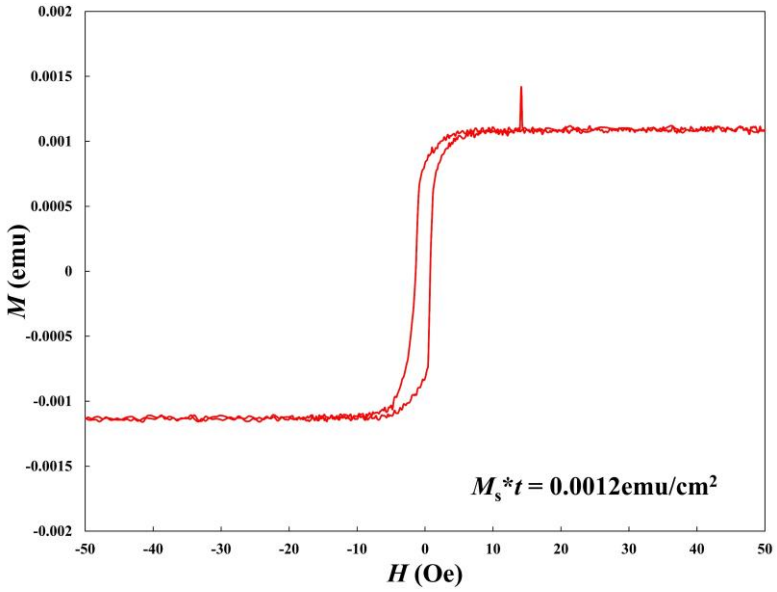

Figure III-25 *M-H* curve for BLS sample

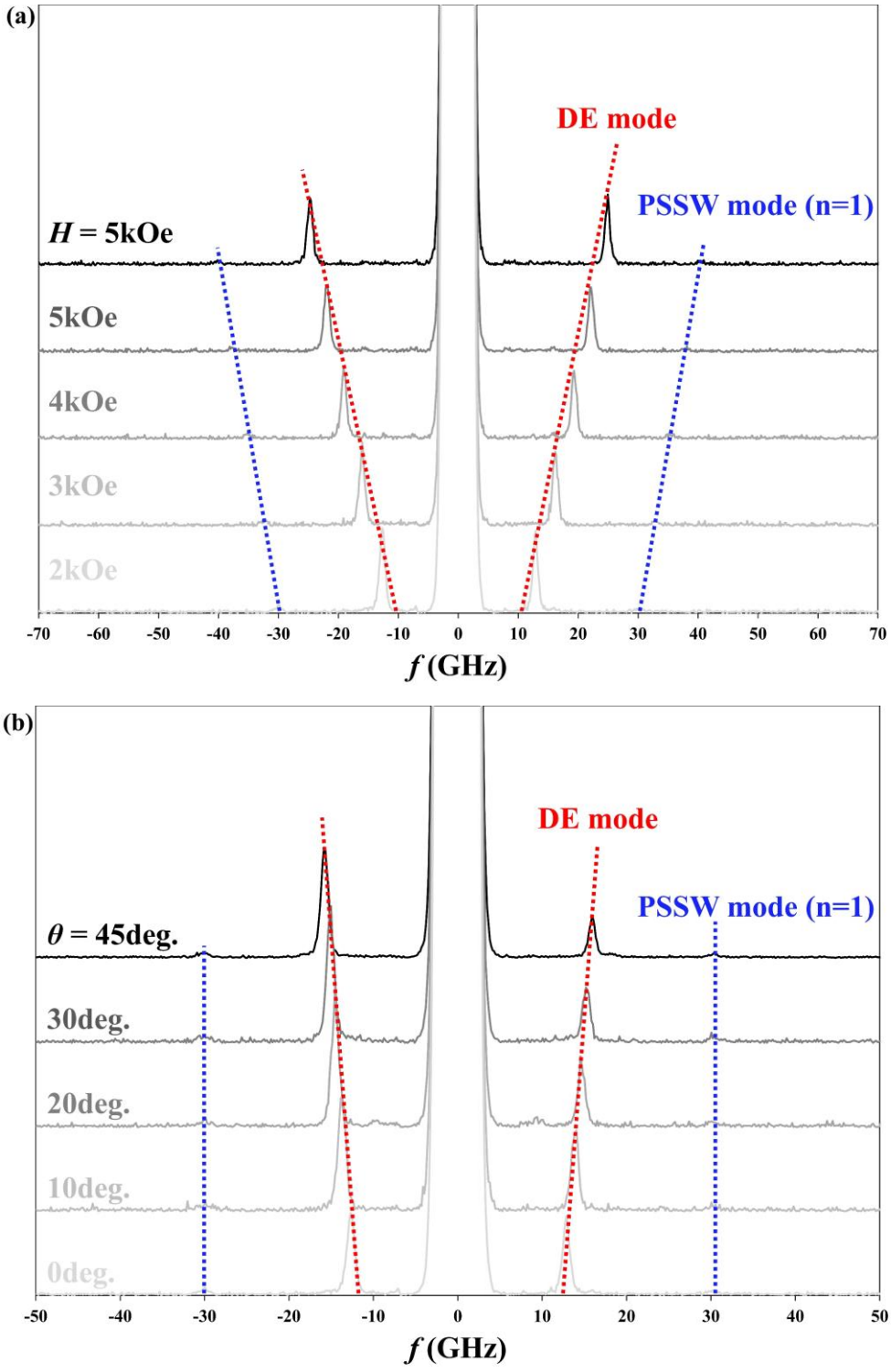

Figure III-26 BLS results of (a) *H* dependence and (b) *k* dependence.

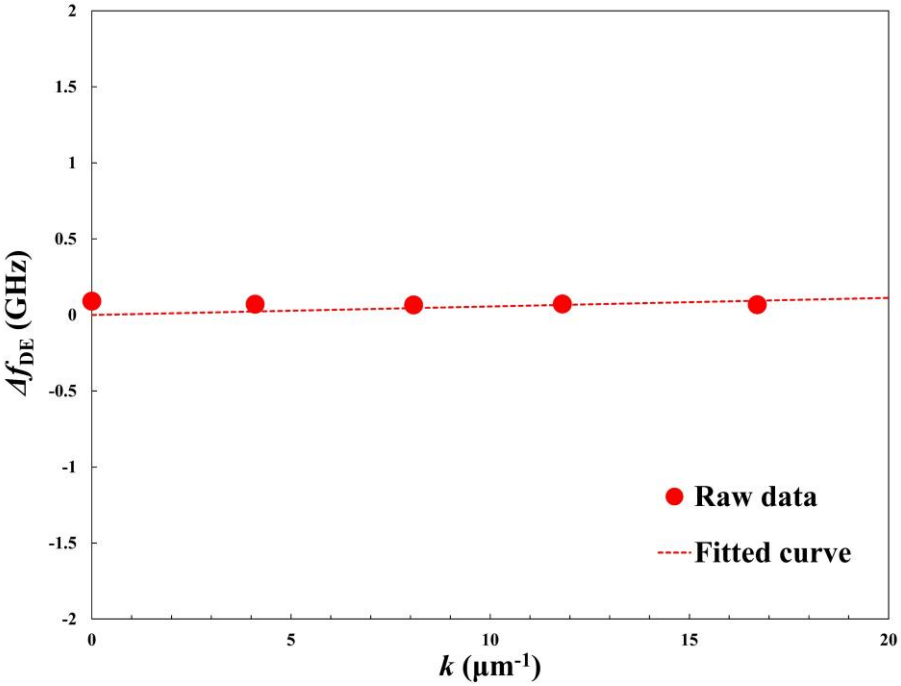

Figure III-27 Evaluation for DMI in FeAlSi films.

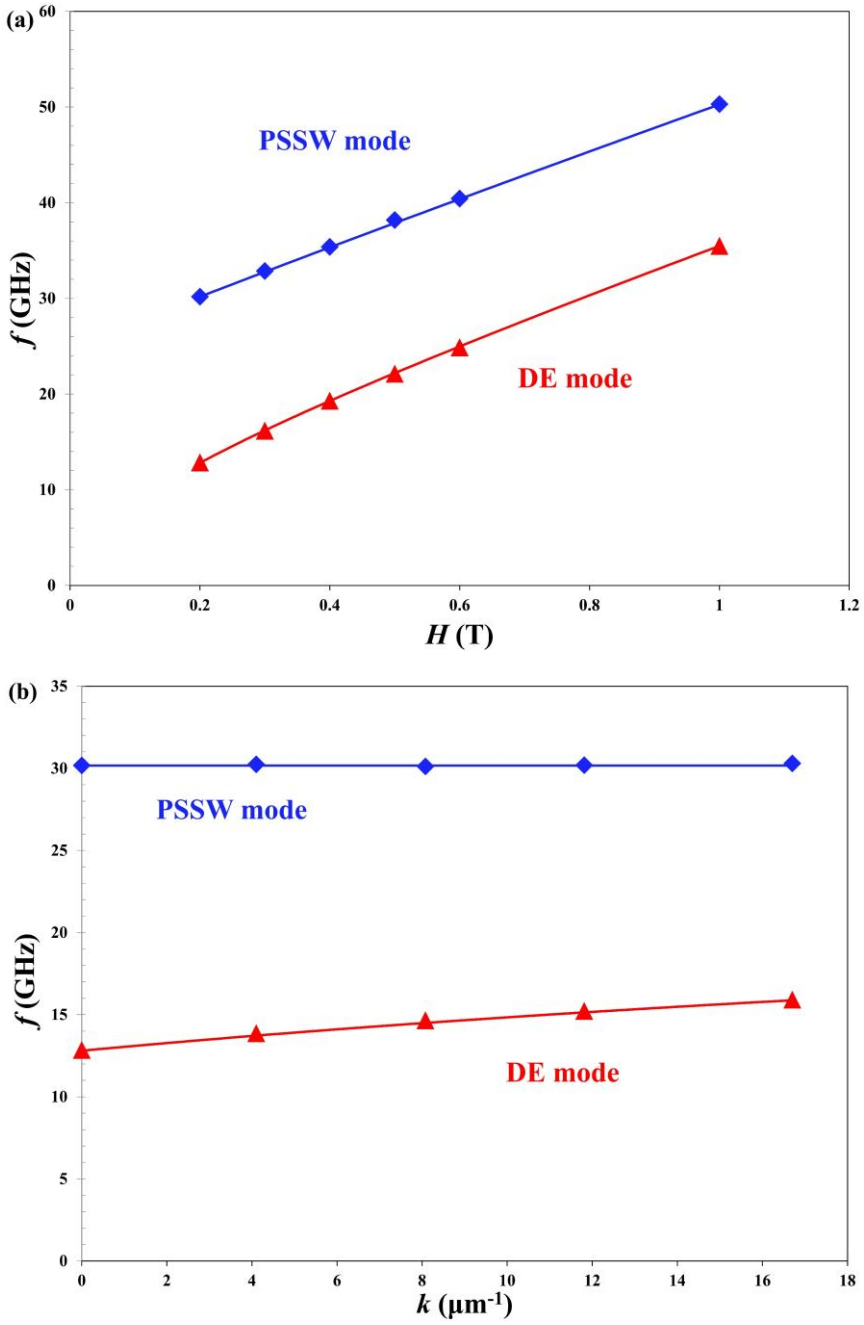

Figure III-28 Peak position and fitting results for BLS.

Table III-2 Fitting results for various magnetic constant for prepared FeAlSi films.

t (nm)	$\frac{\gamma}{2\pi}(GHz/T)$	$\mu_0 H_{k\_eff}(T)$	$A(pJ/m)$
9.95	23.4	1.3	14.3

6. Short summary

- Successfully fabricated nm-FeAlSi thin films with a $D0_3$ structure and observed excellent soft magnetic properties (H_k = 0.43Oe).

- For achieving soft magnetic properties in FeAlSi alloy films, the coexistence of central composition and $D0_3$ structure is not always necessary. The balance between composition and S_{D03} is crucial, and can generally be understood by the ratio of sub-structures composing FeAlSi.

- The ratio of $D0_3$-Fe_3Al has the most significant impact on the overall K_1. When S_{D03} is reduced, adjusting to a richer Al composition can achieve K_1~0. Based on this discovery, the Sendust central composition for film is expanded compared to bulk.

- The origin of in-plane uniaxial magnetic anisotropy in FeAlSi thin films is considered to be due to magnetostriction, but the contribution of magnetostriction to the overall magnetic anisotropy is small compared to the crystalline magnetic anisotropy.

- The determined value of the stiffness constant for FeAlSi was 14.3 (pJ/m), which is similar to that of Fe.

The general consensus has been that the area of soft magnetic property for bulk Sendust is only at one point on the compositional diagram. However, the central composition became extremely wider than previously known based on my discovery. My findings should be useful for applying FeAlSi films with optimal soft magnetic properties to highly sensitive TMR sensors. Inspired by this investigation, the study of Sendust thin films could grow significantly, with potential uses not only in TMR sensors but also in other spintronic devices.

IV. Magnetoresistance property of MTJ using FeAlSi electrode

1. Sample preparation

The FeAlSi composition for MTJ samples is Sample 1, which showed good soft magnetic properties according to the last chapter. The stacking structures for FeAlSi-MTJ and Helicon 3 standard MTJ are shown in Figure IV-1. The FeAlSi layer was annealed inside the sputtering chamber without applying a magnetic field after deposition. The annealing temperature (T_{FeAlSi}) and duration were 400°C and 1 hour, respectively. Additionally, a 50 nm thick FeAlSi thin film was used as the bottom electrode for the MTJ. The fabricated samples were annealed in a vacuum annealing furnace for 1 hour with a 1T magnetic field applied to fix the magnetization of the pinned layer and improve the crystallinity of the MgO barrier.

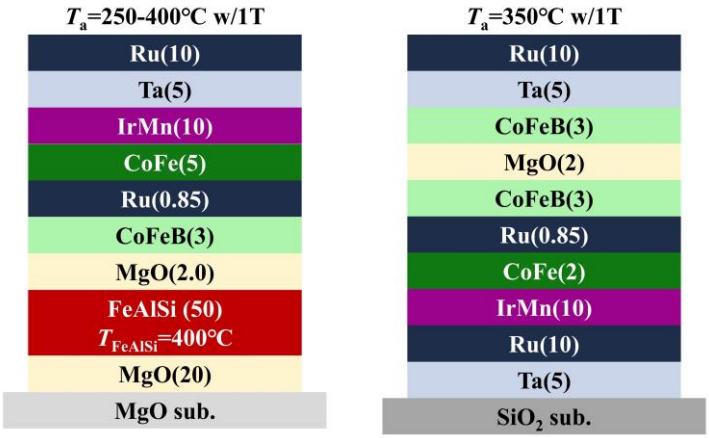

Figure IV-1 Stacking structure of MTJ sample using FeAlSi

2. Tunnel magnetoresistance property

① TMR ratio and RA

Figure IV-2 shows the T_a-dependent magnetoresistance curves of MTJs using FeAlSi free layers with a 10mV bias voltage applied. The applied magnetic field was aligned along the exchange bias of the pinned layer (FeAlSi [110] direction). We observed the TMR effect for the first time at RT in spin-valve-type MTJs with FeAlSi epitaxial electrodes. The TMR ratio was dependent on the annealing temperature, reaching a maximum of 121% at an annealing temperature of 325°C. The high TMR ratio over 100% infers the realization of Δ_1 coherent tunneling through a crystallized MgO barrier, and the observed TMR ratio is comparable to other MTJs for TMR sensors[92–96]. FeAlSi thin films fabricated with the optimal target composition and T_a showed a very low H_k (0.43 Oe), implying a potential sensitivity of ~140%/Oe, which is greater than that of MTJs with amorphous CoFeSiB free layers[9,11]. The TMR effect's T_a dependence is discussed in detail.

Figure IV-3 and Figure IV-4 summarize the T_a dependence of the TMR ratio and resistance-area product (RA). RA values were evaluated by fitting an R versus A^{-1} plot, where R is used as the value of R_{min} in parallel magnetic configurations. An example of the R versus A^{-1} plots for T_a = 325°C is shown in Figure IV-5. The improvement in TMR with increasing T_a is due to enhanced Δ_1 coherent tunneling through the crystallization of the MgO barrier, resulting in a decrease in RA from 250 to 325°C. Deterioration in TMR above 325°C is considered to be due to degradation of the synthetic pinned layer caused by excessive annealing. To clarify this point, I investigated the pinned layer more deeply in the next section.

The magnetoresistance curve of the MTJ showing the highest TMR ratio (T_a = 325°C) exhibited a relatively low switching field of 4 Oe (the inset of Figure IV-2), reflecting the soft magnetic properties of the FeAlSi free layer, but slightly higher than the coercivity observed in the single FeAlSi layer shown in the previous chapter. The increase in the coercivity of the MTJ could be due to differences in the thickness and shape anisotropy of the FeAlSi layer, as the FeAlSi layer was microfabricated into a rectangle of 1200 × 300 μm^2 for use as the bottom electrode. The direction of the magnetic field applied for MR curve measurements is along the magnetic easy axis of shape anisotropy (longitudinal direction of the FeAlSi electrode), resulting in an increased switching field. In future work, it is possible to achieve lower magnetic anisotropy by optimizing the thickness and shape of the FeAlSi bottom electrode.

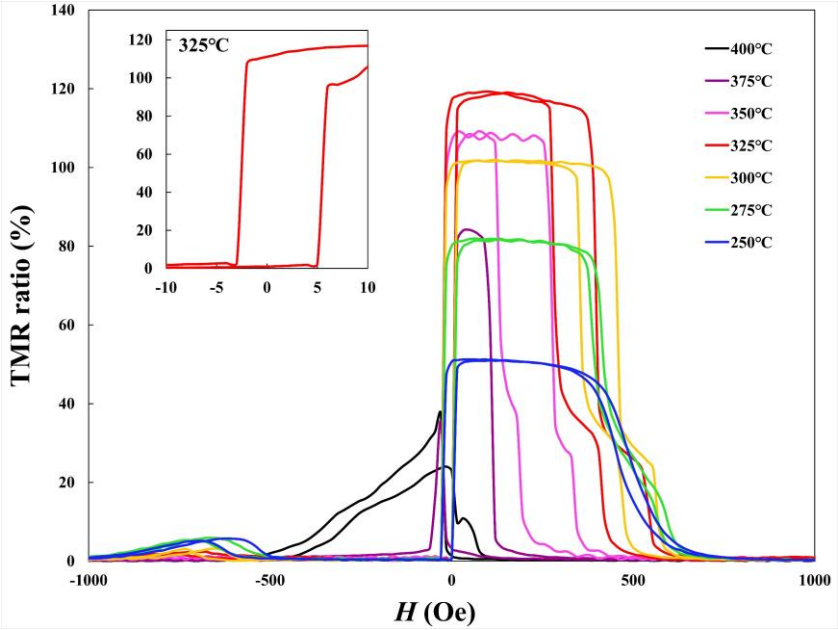

Figure IV-2 TMR curve dependence on T_a for FeAlSi-MTJ (inset): Extended image of T_a = 325 °C sample around zero field

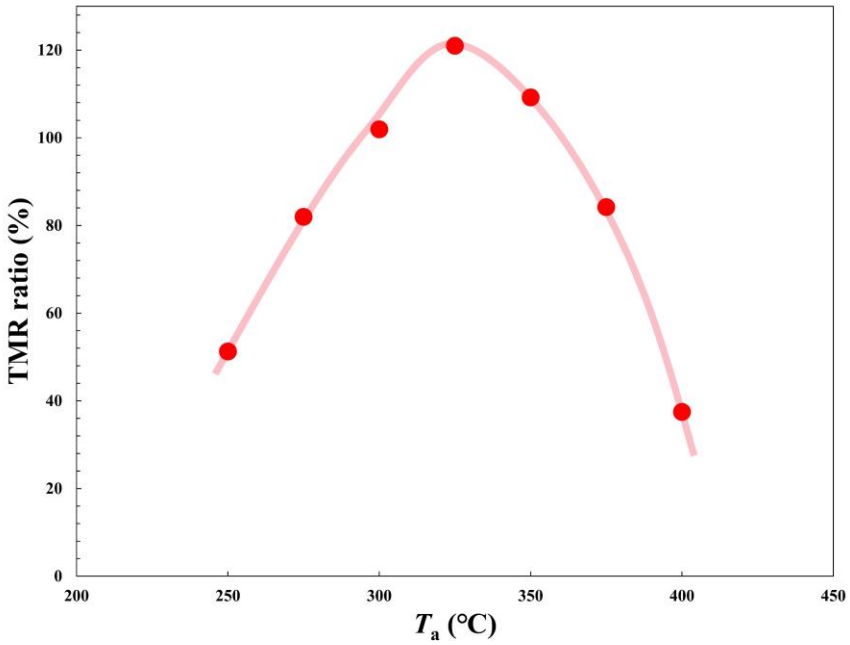

Figure IV-3 TMR ratio vs T_a for samples of FeAlSi free layer

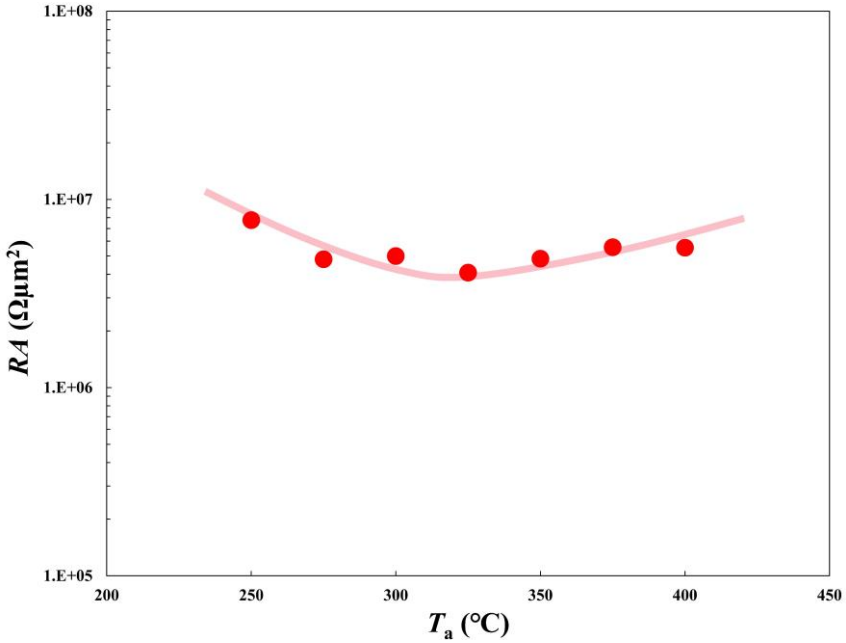

Figure IV-4 *RA* vs T_a

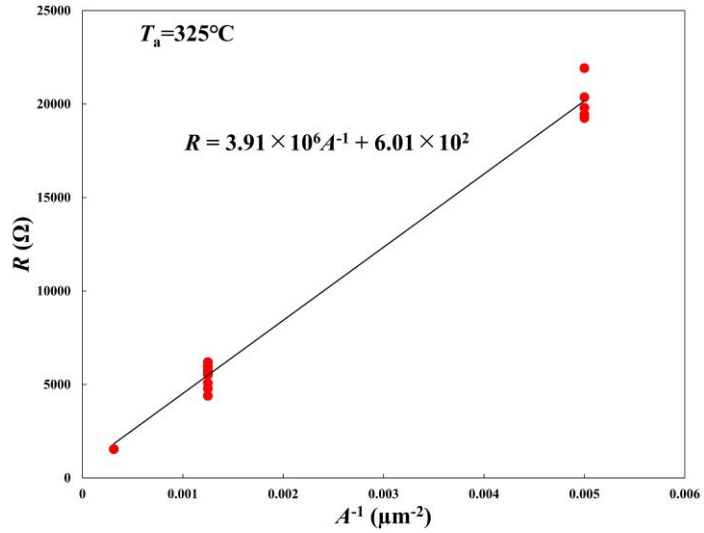

Figure IV-5 A typical example of a plot of *R* vs A^{-1} (T_a=325°C)

② Exchange coupling in pinned layer

Deterioration in TMR above 325°C is supposed to be caused by the degradation of the synthetic pinned layer caused by excessive annealing. I investigated the pinned layer more deeply to clarify this point.

As shown in Figure IV-2, the shift field of the pinned layer decreased above 325°C. Figure IV-6 shows field shift for FeAlSi-MTJ. Ideal anti-parallel coupling is observed at T_a = 325 °C, but the coupling changes to parallel at T_a = 400 °C. To clarify this reason, VSM measurements of MTJ thin films at annealing temperatures T_a = 325 and 400°C were conducted as shown in Figure IV-7. We confirmed that the exchange bias by the CoFe/IrMn interface is almost maintained after annealing at 400°C, but the RKKY synthetic antiferromagnetic coupling mediated by Ru was degraded. Therefore, the main reason for the decrease in shift fields due to over-annealing was diffusion of Ru, not Mn[97,98,99]. To prevent Ru diffusion, we need to thoroughly investigate other Ru thicknesses with RKKY combinations or flatness improvement of MTJ stacking[99]. However, future detailed investigations using Transmission Electron Microscopy (TEM) and Electron Energy Loss Spectroscopy (EELS) are necessary to clarify the mechanism of relatively low stability against the annealing process.

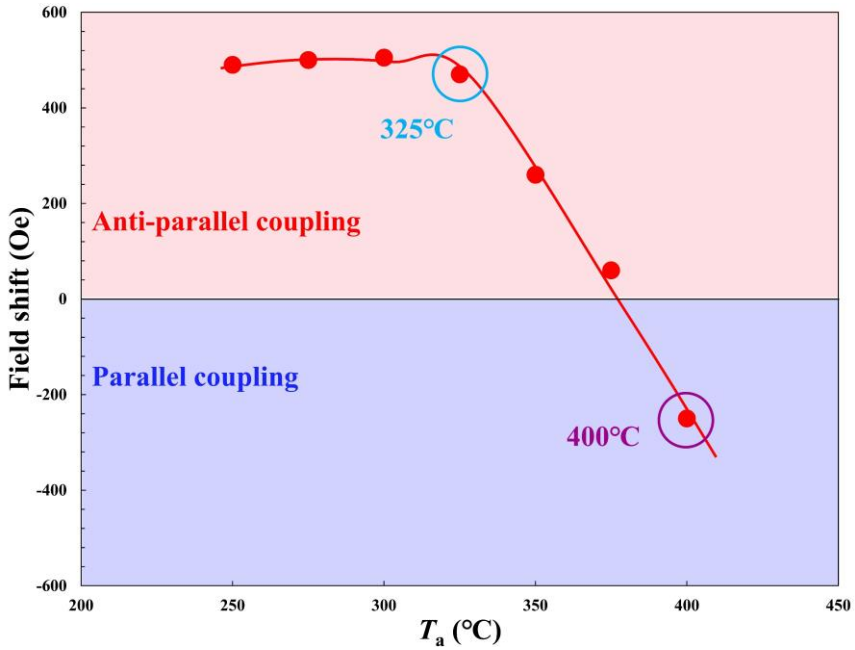

Figure IV-6 Field shift for FeAlSi – MTJ

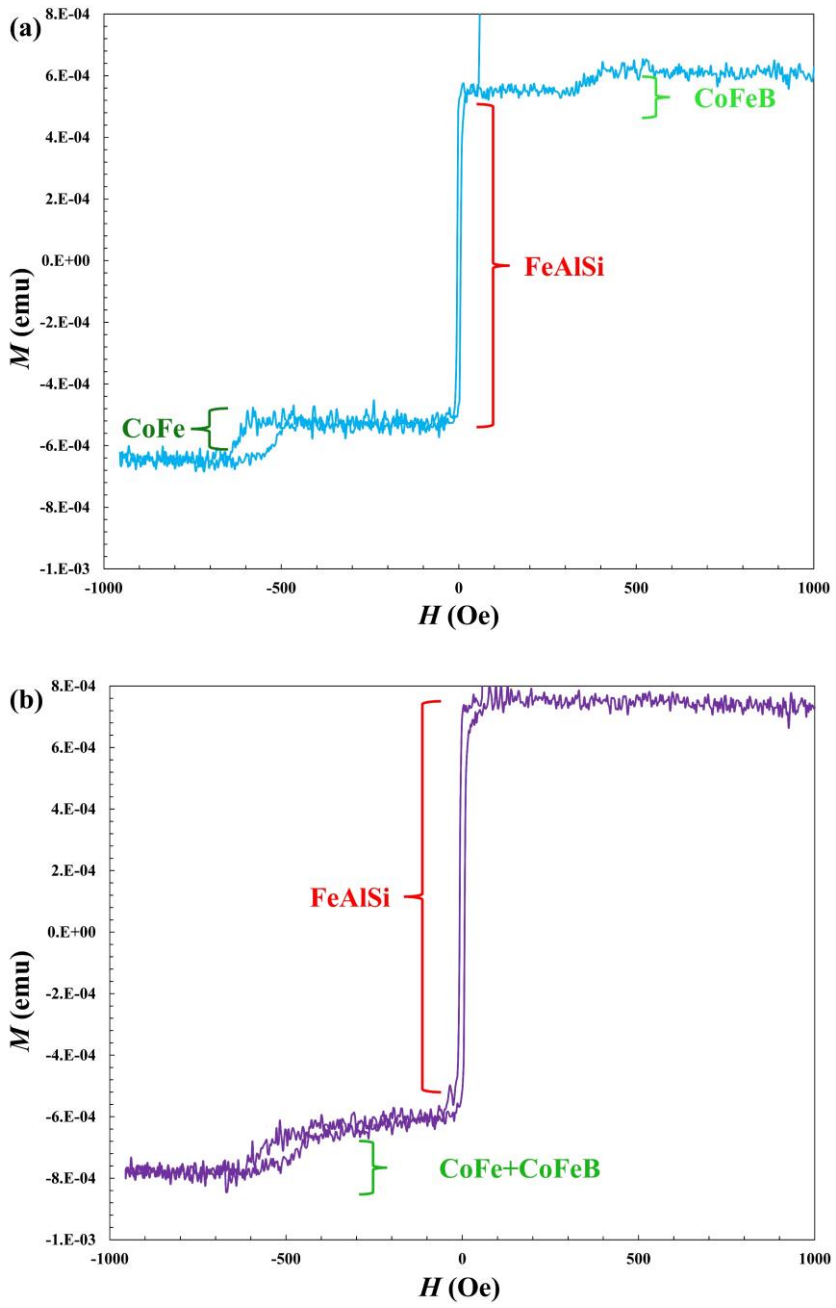

Figure IV-7 VSM result of FeAlSi-MTJ (a) T_a = 325 ℃ (b) T_a = 400 ℃

3. Discussion of TMR property

① Oxidation of FeAlSi/MgO interface

I discuss in detail the interface between the ferromagnetic layer and the insulating layer. In Figure IV-4, the observed RA was in the order of 10^6 Ω μm^2, which was relatively high compared to previous MTJ studies with high TMR ratios[92,93]. This could be due to oxidation at the interface between the FeAlSi bottom layer and the MgO barrier. Figure IV-8 shows a cross-sectional TEM image of an MTJ using a FeAlSi free layer annealed at T_a = 325°C. I observed a very thin layer of bright contrast at the interface between the FeAlSi free layer and the MgO barrier. This contrast implies oxidation of the surface of the FeAlSi layer, which could significantly reduce the TMR ratio[100]. For avoiding this oxidation, Mg insertion between FeAlSi and MgO is effective according to some previous works[101,102], which could further improve the TMR ratio. However, Heusler/MgO interface in a previous work (Figure IV-9) also showed such contrast, where the relatively high TMR ratio was observed. In future works, detailed chemical analysis such as Electron Energy Loss Spectroscopy (EELS) or X-ray Photoelectron Spectroscopy (XPS) would be required to confirm the surface oxidation of the FeAlSi layer.

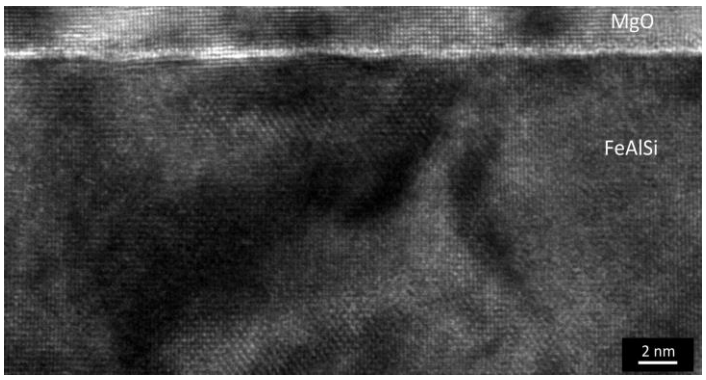

Figure IV-8 TEM of FeAlSi/MgO interface

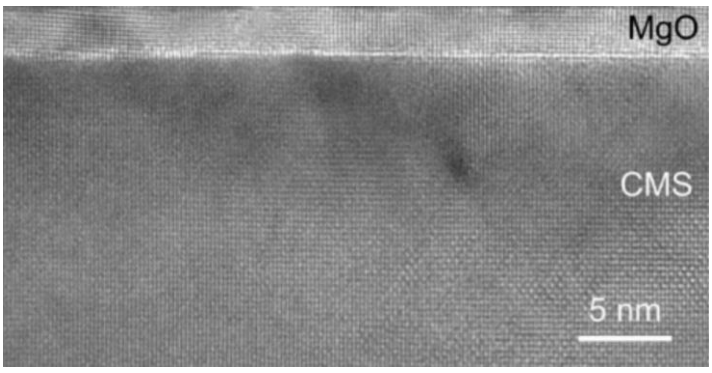

Figure IV-9 TEM of Heusler/MgO interface

② Temperature dependence

Basically, the TMR ratio decreases with the increasing temperature and V_{Bias} increase, and the TMR reduction is mainly caused by magnetic fluctuation in ferromagnetic layers and the large resistance drop in anti-parallel configuration due to the inelastic tunneling effect. The previous works suggested that TMR ratio reduction against temperature and bias voltage is related to magnon excitation in ferromagnetic layers[9,103–106]. The Curie temperature (T_c) of bulk-FeAlSi is previously reported as 733K[107], which is much smaller than that of Fe (1043 K) [108]. As a result, this relatively low T_c can cause the large temperature and V_{Bias} dependences in FeAlSi-MTJs.

Figure IV-10 shows the temperature dependence of magnetoresistance curves for MTJ using the FeAlSi free layer. Figure IV-11 summarizes the temperature dependence of TMR ratio. I confirmed that TMR ratio increased monotonously from 104.8% at 300K to 179.8% at 10K, and the ratio of (TMR ratio at 300K)/ (TMR ratio at 10K) is 0.58. In other previous works of MTJ using Fe electrode[109], the TMR ratio also increase monotonously, from 170% at 300K to 318% at 10K. (TMR ratio at 300K)/ (TMR ratio at 10K) for Fe-MTJ is 0.53, which is almost same as FeAlSi-MTJ in our study. These results show that the temperature dependence of TMR ratio for FeAlSi-MTJ and Fe-MTJ are almost same. On the other hand, (TMR ratio at 300K)/ (TMR ratio at 10K) for Heusler-MTJ in other previous work is much lower than those values (0.31) [110]. This large temperature dependence of TMR ratio is affected by the reduction of spin polarization at the interface of Heusler alloys[110]. These results proved the thermal stability of TMR ratio and spin polarization in FeAlSi-MTJs comparable to Fe-MTJs.

Figure IV-12 shows the temperature dependence of RA for parallel (RA_P) and anti-parallel (RA_{AP}) configurations. I found that the temperature dependence of RA_{AP} is much larger than that of RA_P similar to previous works[13,109,111,112]. The RA_{AP} increase with temperature decrease is considered to be the suppression of spin-flip tunneling caused by magnon excitations at the interface between FeAlSi and MgO[113].

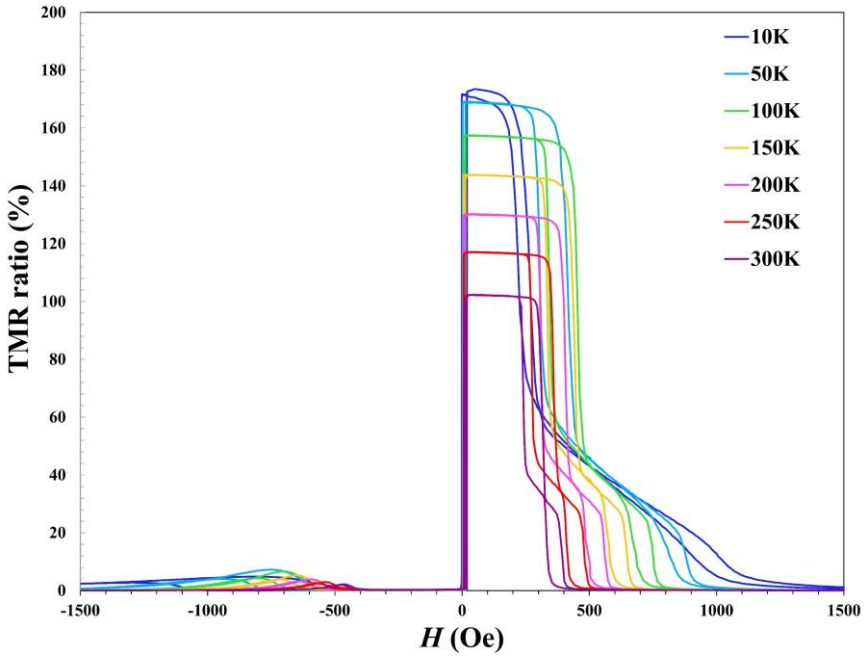

Figure IV-10 TMR curve vs *T* for FeAlSi-MTJ

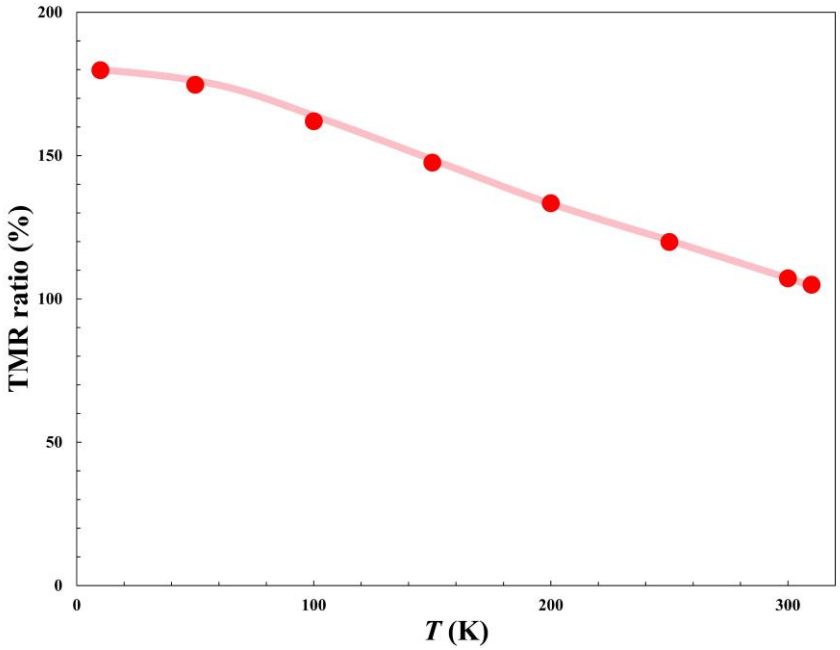

Figure IV-11 TMR ratio vs *T*

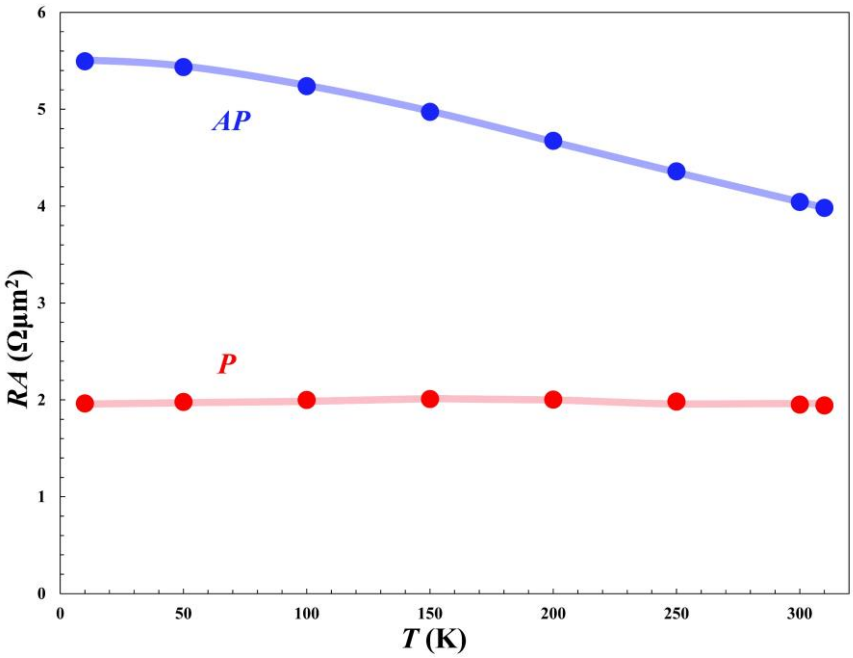

Figure IV-12 *RA* vs *T*

③ Bias voltage dependence of TMR ratio and R_{AP}

Figure IV-13 shows V_{Bias} dependence of TMR ratio evaluated by *dI/dV-V* curves for the parallel and anti-parallel magnetic configurations in FeAlSi-MTJ. The TMR ratio drop with a finite V_{Bias} is considered to be mainly affected by magnon excitation[106]. V_{half}, which is the V_{Bias} where TMR ratio is half of that at V_{Bias} = 0 V, is about 300 mV. This value is the almost same as a previous work for Fe-MTJs[114]. Both temperature and V_{Bias} dependences of TMR effect for the FeAlSi-MTJ and Fe-MTJ are almost same, which indicates the FeAlSi/MgO interface appears to behave similar to that of Fe/MgO interface.

For investigating the magnon excitation at the FeAlSi/MgO interface in detail, I measured conductance curve and IETS for AP state at 1.6 K using PPMS (Figure IV-14, Figure IV-15). I successfully measured the IETS with very low noise, which allow us to observe various clear peaks. The peak around V_{Bias} ~ 80 mV is supposed to be caused by the phonon excitation in the MgO barrier, which is typically observed in some previous works[102,115,116]. The strong peak at V_{Bias} ~ 30 mV is considered to be originating from the magnon excitation[115]. This is supposed to be related to temperature dependence of RA_{AP} in Figure IV-12. In Figure IV-15, this magnon contribution exists up to V_{Bias} = 150 ~ 200 mV, which is comparable to Fe-MTJs (150~200 mV) [117,118] and larger than Heusler-MTJs (< 100 mV) [115]. This voltage is called maximum magnon cutoff energy E_m[119], which is related to T_c as below.

$$E_m = \frac{3k_B T_c}{S+1} \tag{28}$$

Where, S is the spin of a ferromagnet. T_c for FeAlSi is calculated about 1000 K from this equation, which is similar to Fe (1043 K[108]). The evaluated large T_c of FeAlSi comparable to Fe corresponds to the small temperature dependence of TMR ratio and high V_{half}. However, the estimated T_c of 1000 K in FeAlSi-MTJ is obviously higher than a previous report of T_c for FeAlSi (733 K [107]). The first possible reason for high T_c of FeAlSi in this study is that the composition and the atomic ordering of FeAlSi films in this work are different from a previous work[120]. The second possible reason is that the composition of FeAlSi at the interface with MgO barrier is Fe-rich because of diffusion of Si and Al atoms during annealing process.

Here, I summarize exchange stiffness constant A in the chapter 3, Curie temperature T_c, (TMR@300K)/(TMR@10K) and E_m for FeAlSi and Fe in Table IV-1, where all of these values should be correlated as mentioned already. The results for FeAlSi and Fe are similar except for T_c, and this reason for discrepancy of T_c is already mentioned above. Our study also revealed that TMR ratio reduction with finite T and V_{Bias} in FeAlSi-MTJ is significantly lower than that in Heusler-MTJ. The large TMR reduction in Heusler-MTJ is considered to be caused by local A (T_c) reduction at the interface with MgO [31–33], and thus I understand that there is minimal such effect in FeAlSi-MTJ.

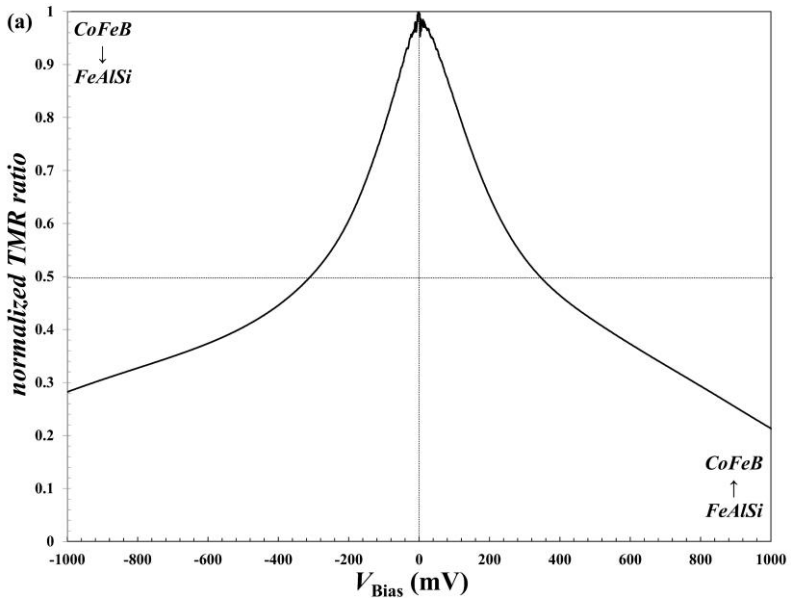

Figure IV-13 TMR ratio vs V_{Bias}

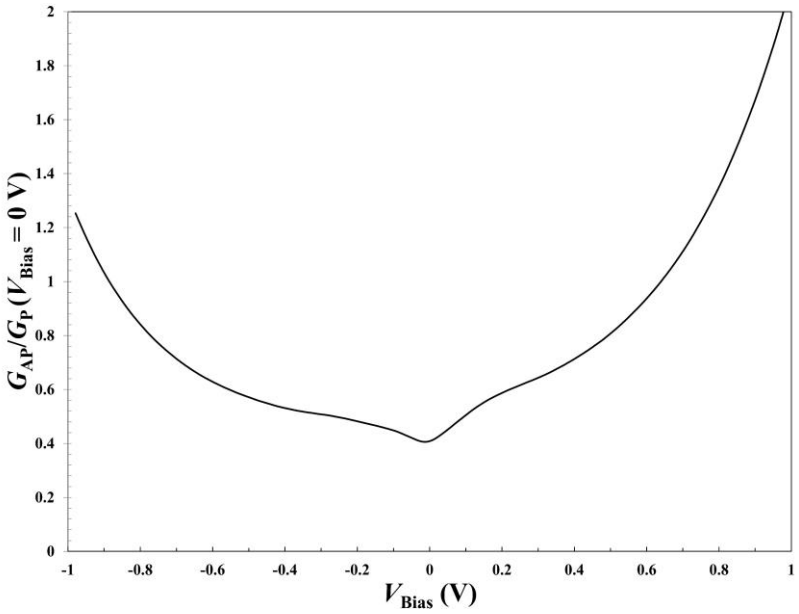

Figure IV-14 G_{AP} vs V_{Bias}

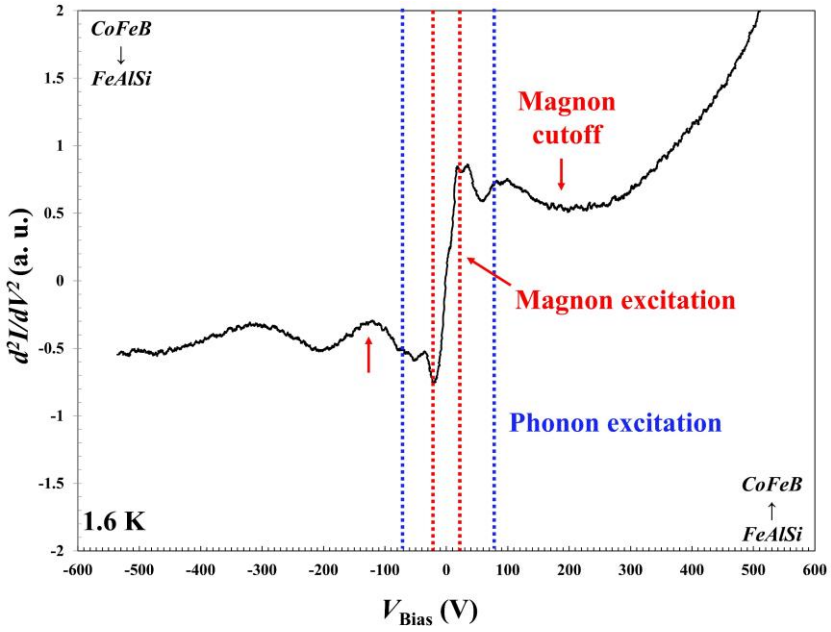

Figure IV-15 Result of IETS in AP state

Table IV-1 The summary of *A* and temperature dependence of TMR ratio for FeAlSi and Fe

Ferromagnetic material	T_c (K)	A(pJ/m)	(TMR@300K)/ (TMR@10K)	E_m (meV)
FeAlSi	733	14.3	0.58	150~200
Fe	1043	18.5	0.53	150~200 [117,118]

④ Bias voltage dependence of R_P

Figure IV-16 (a) shows the G_P dependence on V_{Bias} calculated using the *I-V* curve, where G_P is normalized by the G_P at V_{Bias} = 0 V. In comparison, Figure IV-16 (b) shows the conductance dependence on V_{Bias} for a Helicon 3 standard MTJ normalized by the conductance at V_{Bias} = 0 V. The asymmetric feature in FeAlSi-MTJ is caused by the material difference of top and bottom electrodes. This asymmetric behavior was not observed in the CoFeB/MgO/CoFeB MTJ because top and bottom electrodes are the same ferromagnetic material. For the FeAlSi-MTJ, a conductance peak was observed around V_{Bias} = 0 V, which is clearer than that of the CoFeB/MgO/CoFeB MTJ in Figure IV-16 (b). The zero-bias peak was also observed in previous reports for Fe/MgO/Fe MTJs[118,121], and is thought to be the contribution of the Δ_5 channel in the Fe(001) majority band, where the top of the Δ_5 majority band lies just above fermi energy. When the energy of tunneling electrons overcomes the top of the Δ_5 band due to high V_{Bias}, the conduction channel related to the Δ_5 band quenches[118]. The result for FeAlSi-MTJ indicates that Δ_5 tunneling also occurs due to the similarity of the electronic states of Fe and FeAlSi interface with MgO. There are two hypotheses for the similarity of those two electronic states. The first is that the band structures of FeAlSi and Fe are similar as motivated in introduction. The second is that the FeAlSi interface with MgO becomes Fe rich, which is caused by Al and Si diffusion by annealing process. To clarify this point, detailed chemical analysis such as Electron Energy Loss Spectroscopy (EELS) or X-ray Photoelectron Spectroscopy (XPS) is required in future works.

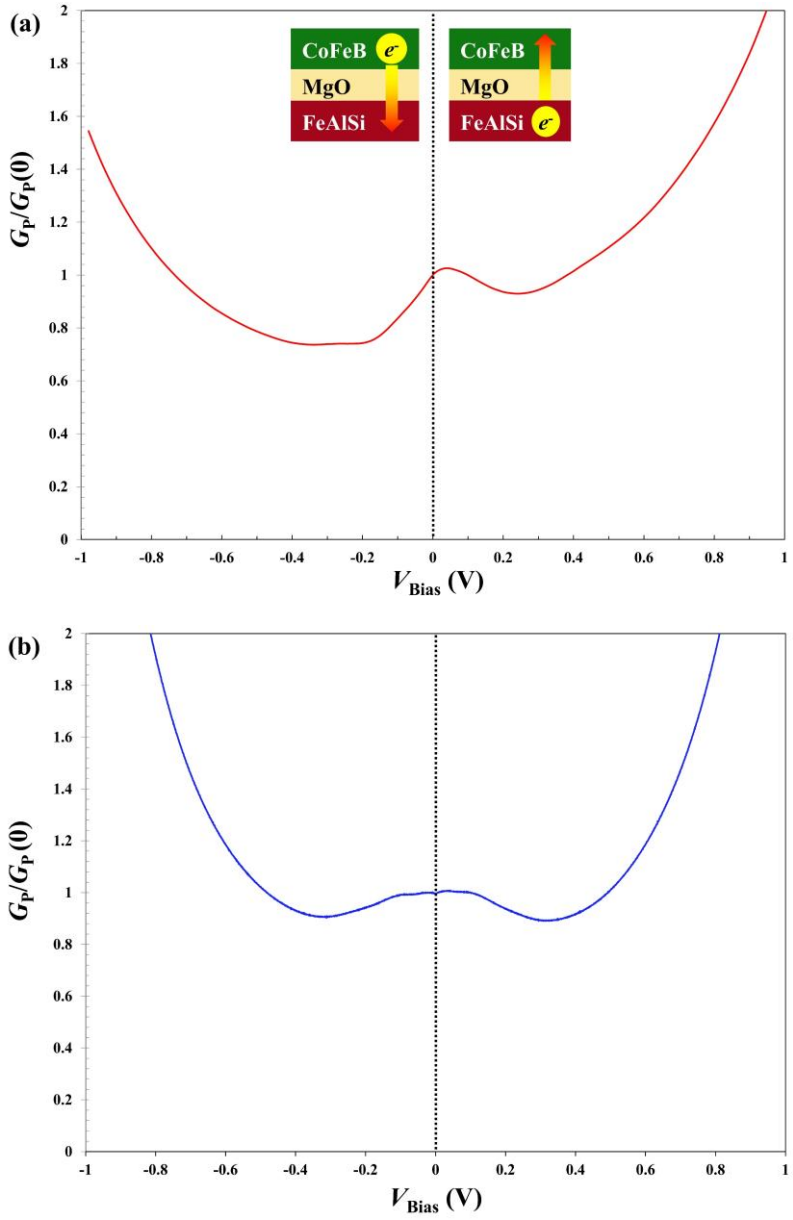

Figure IV-16 Conductance curve on V_{Bias} for FeAlSi-MTJ at 10 K normalized by G_P at V_{Bias} = 0 V. (b) Conductance for Helicon 3 standard MTJ normalized by conductance at V_{Bias} = 0 V

⑤ Tunnel anisotropic magnetoresistance property

To more thoroughly investigate the TMR characteristics of FeAlSi-MTJs, we measured the V_{bias}-dependence of Tunnel Anisotropic Magnetoresistance (TAMR) and compared it with typical Fe/MgO/Fe MTJs. The TAMR effect differs from the conventional TMR effect. When the magnetizations in MTJs are in parallel configuration along in-plane or out-of-plane directions induced by a strong magnetic field, the resistance changes according to the direction of magnetization. The TAMR ratio is defined using the conductance in in-plane configuration (G_{IP}) and out-of-plane configuration (G_{OP}) as follows:

$$\textbf{TAMR ratio}=\frac{\boldsymbol{G_{IP}}-\boldsymbol{G_{OP}}}{\boldsymbol{G_{OP}}}\times\textbf{100 (\%)} \tag{29}$$

The origin of TAMR is thought to be the Interface Resonant States (IRS) introduced by band calculations at the interface considering spin-orbit coupling with MgO and is related to tunneling through hotspots[10,122–126]. Previous studies investigated the V_{bias}-dependent TAMR in Fe/MgO/Fe MTJs, observing a TAMR ratio of 1.1% originating from IRS. I conducted measurements of V_{bias}-dependent TAMR in FeAlSi-MTJs and compared them with Fe-MTJs.

In Figure IV-17, a difference between G_{IP} and G_{OP} at low V_{bias} is observed, which I believe is due to TAMR effect stemming from IRS. Figure IV-18 shows the V_{bias}-dependence of the TAMR ratio. A high TAMR ratio of 1.0% at V_{bias} = +0.12 V is observed, comparable to the 1.1% observed in Fe/MgO/Fe junctions at V_{bias} = ±0.25 V[118]. Additionally, the negative TAMR peak at V_{bias} = +0.4 V is similar to that observed in previous studies at V_{bias} = -0.3V[118]. Previous studies theoretically predicted and experimentally verified that IRS enhances the TAMR effect[125,126]. Currently, the reason for the difference in V_{bias} where the TAMR peak is observed is not clear, but the high TAMR effect in FeAlSi-MTJs is speculated to be due to tunneling via IRS, similar to Fe-MTJs.

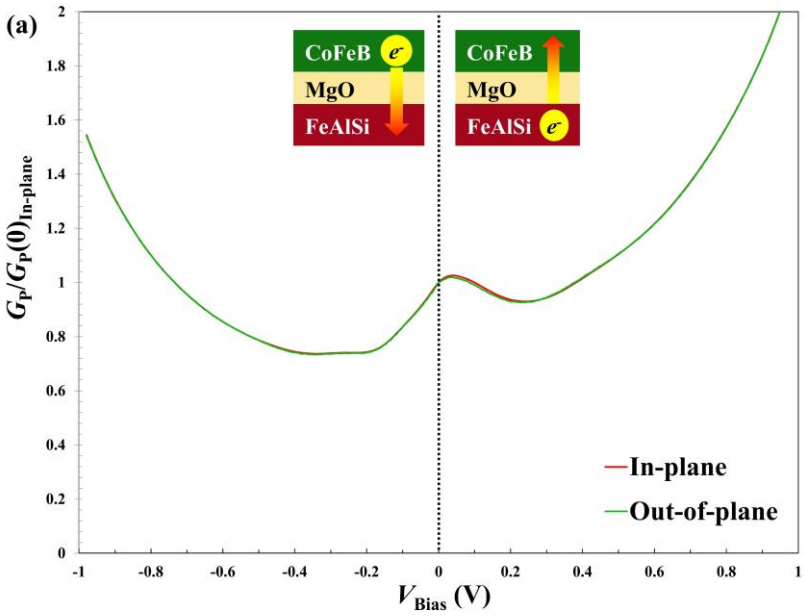

Figure IV-17 Conductance curve on V_{Bias} for prepared MTJs at 10 K. G_{IP} and G_{OP} for FeAlSi-MTJ normalized by G_{IP} at V_{Bias} = 0 V.

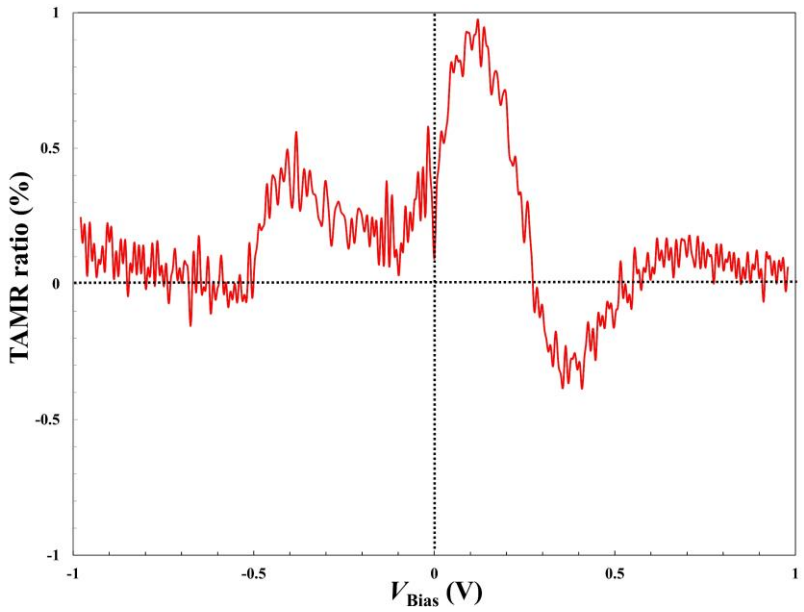

Figure IV-18 TAMR ratio dependence on V_{Bias} for FeAlSi-MTJ

4. Short summary

- Successfully observed room temperature TMR effect in MTJs using FeAlSi electrodes (TMR ratio = 121%).

- At 10K, the reduction in R_{AP} due to inelastic tunneling processes was suppressed, enhancing the TMR ratio to up to 180%.

- It was found that the temperature and bias voltage dependence of the TMR effect in FeAlSi-MTJs are almost the same as those in MTJs with Fe free layers.

- IETS measurements conducted at low temperatures confirmed a relatively large cutoff energy for magnon excitations at the FeAlSi and MgO interface.

- Results from the conductance curve at 10K confirmed zero-bias conduction of Δ_5 electrons similar to Fe, suggesting a similarity in band dispersion between Fe and FeAlSi interface with MgO.

- In FeAlSi-MTJs, a high TAMR ratio (=1%) comparable to Fe-MTJs was observed, indicating the presence of Interface Resonant States (IRS) at the FeAlSi/MgO interface similar to those at the Fe/MgO interface.

Based on the discoveries above, I found that FeAlSi is considered to have the potential to show higher TMR ratio at RT comparable to Fe because of some similar behavior of FeAlSi/MgO-MTJ and Fe/MgO-MTJ (band dispersion, magnetic fluctuation at the interface). Here, the cause of the relatively low TMR ratio in my study has been investigated: FeAlSi/MgO interface oxidation and degradation of pinned layer with Ru diffusion. For avoiding this oxidation, Mg insertion between FeAlSi and MgO is effective. To prevent Ru diffusion, the optimization of Ru thicknesses with RKKY combinations or flatness improvement of MTJ stacking are beneficial. Therefore, FeAlSi has the big possibility to show higher TMR ratio by attempting these approaches in future works.

V. Summary

In this study, I firstly investigated FeAlSi film for the application of TMR sensor.

The key discoveries are two points below.

- **Successfully fabricated nm-order FeAlSi film with ideal soft magnetic property. The observed H_k was 0.43Oe, which is lower than conventional free layer materials.**

  Nanometer-order FeAlSi epitaxial films with partial $D0_3$ ordered structure were grown on MgO substrates, resulting in ideal soft magnetic properties. In certain FeAlSi compositions, it was found that the sign of the magnetocrystalline anisotropy constant K_1 changes as the annealing temperature increases. This is caused by a change in the volume balance of the ordered phases with the annealing process and the point at which K_1=0 shifts to the Al-rich concentration as the degree of $D0_3$-ordering decreases. Based on this discovery, the Sendust central composition for film is expanded compared to bulk. K_1 was accurately measured by FMR under optimal conditions, yielding a value of 1.6×10^2 (erg/cc), which is comparable to that of bulk. The uniaxial component of magnetostriction-induced magnetic anisotropy was small, with the quadrupolar component due to magnetocrystalline anisotropy being dominant.

- **Firstly observed high TMR ratio (> 100%) with MTJ using FeAlSi electrode. The confirmed TMR ratio was 121%, which is comparable to other MTJs.**

  MTJs with (001)-oriented $D0_3$-FeAlSi epitaxial thin films were fabricated and characterized. A TMR ratio of 121% was observed, and a relatively low switching field reflecting the soft magnetism of FeAlSi was also confirmed. TMR ratio at LT was 180%, where thermal stability is comparable to Fe-MTJ. The band structure of FeAlSi interface with MgO is considered to be similar to Fe based on Δ_5 tunneling and high TAMR. The relatively low TMR ratio is considered to be attributed to the film quality of the MTJ (interface oxidation, crystallinity, stacking flatness, etc.). Therefore, FeAlSi holds significant potential for demonstrating a higher TMR ratio by addressing these issues in future researches.

Based on these findings, I conclude that FeAlSi has good potential sensitivity as a new free layer material as shown in Figure V-1, which is better than the conventional material of CoFeSiB. We should note that the potential sensitivity of FeAlSi is calculated by each value of TMR ratio and H_k in my study, which means there is the other challenge of linear response of sensor with maintaining the high TMR ratio and low H_k. To achieve this, it's supposed that we need further study of induced anisotropy of FeAlSi film or (011)-oriented FeAlSi film (in-plane rectangle).

As mentioned above, FeAlSi can potentially achieve the several times higher TMR ratio by improving the film quality of MTJ. Therefore, FeAlSi has the prospect to realize a high-sensitive TMR sensor with the comparable performance to SQUID. Additionally, Fe/MgO-based MTJs potentially shows the TMR ratio over 600% according to the most recent work[127], which indicates that FeAlSi-MTJ is expected to show further higher TMR ratio and sensor sensitivity.

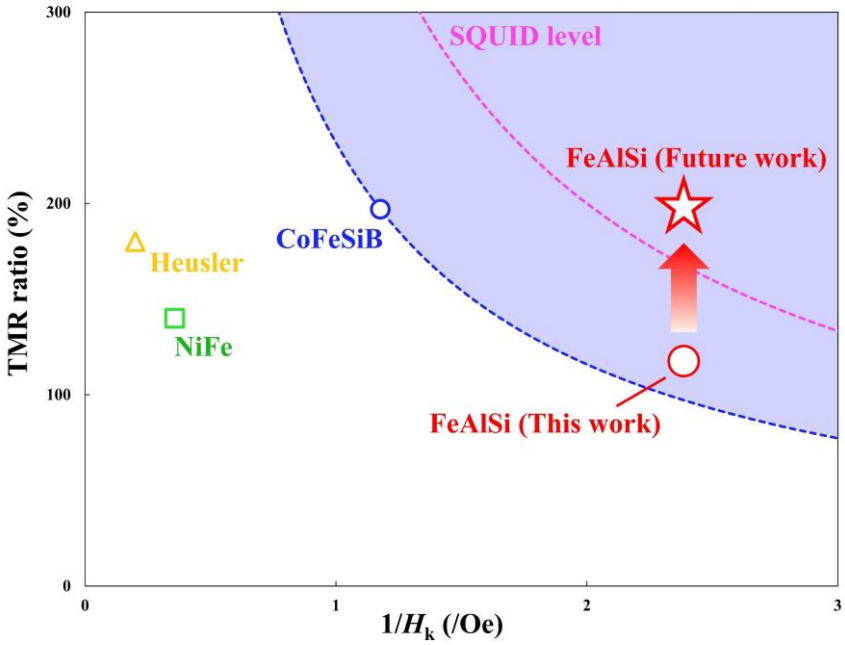

Figure V-1 My achievement and future goal

This study has discovered a method for fabricating Sendust films exhibiting soft magnetic properties and over 100% TMR ratio, thereby significantly increasing the potential for Sendust alloys to gain renewed attention not only as bulk soft magnetic materials but also as cutting-edge quantum device materials. The emergence of such new materials holds the potential to dramatically enhance the performance of quantum devices. It is expected that this research will lead to a significant leap in the sensitivity of TMR sensors. Furthermore, this research may initiate the application and development of Sendust films in quantum devices beyond TMR sensors, with the expectation of widespread expansion of research in Sendust films.

VI. Publications & Talks

Publications

1. **S. Akamatsu**, M. Oogane, M. Tsunoda and Y. Ando, “Fabrication of softmagnetic FeAlSi thin films with nm-order thickness for the free layer of magnetic tunnel junction based sensors”, AIP Adv. 10, 0 15302 (2020).
2. **S. Akamatsu**, M. Oogane, Z. Jin, M. Tsunoda and Y. Ando, "Tunnel magnetoresistance in magnetic tunnel junctions with FeAlSi electrode." AIP Adv. 11.4 045027 (2021)
3. **S. Akamatsu**, M. Oogane, M. Tsunoda and Y. Ando,“Guidelines for attaining optimal soft magnetic properties in FeAlSi films”, Appl. Phys. Lett. 120, 242406 (2022).
4. **S. Akamatsu**, M. Oogane, M. Tsunoda and Y. Ando, “Magnetic tunnel junctions using epitaxially grown FeAlSi electrode with soft magnetic property”, AIP Adv. 12, 075021 (2022),**(Editor’s pick**.
5. **S. Akamatsu**, T. Nakano, Muftah Al-Mahdawi, W. Yupeng, M. Tsunoda, Y. Ando, and M. Oogane, “Tunnel anisotropic magnetoresistance in magnetic tunnel junctions using FeAlSi”, AIP Adv., *13*(2), 025005 (2023).
6. **S. Akamatsu**, B. H. Lee, Y. Hou, M. Tsunoda, M. Oogane, G. S. D. Beach, and J. S Moodera, “Temperature and bias voltage dependences of magnetic tunnel junction with FeAlSi electrode”, APL Materials 12, 021101 (2024)

Talks at National Conferences

1. ○**S. Akamatsu**, M. Oogane, M. Tsunoda and Y. Ando,“Fabrication of Sendust thin films for application to magnetic tunnel junction sensors”, 64th Annual Conference on Magnetism and Magnetic Materials, DW-04, Las Vegas, November 2019 (Poster)
2. ○**S. Akamatsu**, M. Oogane, M. Tsunoda and Y. Ando,“FeAlSi thin films with low magnetic anisotropy for the free layer of magnetic tunnel junction based sensors", 65th Annual Conference on Magnetism and Magnetic Materials, F3-06, November 2020 (Poster).
3. ○**S. Akamatsu**, M. Oogane, M. Tsunoda and Y. Ando, “Systematic investigation to obtain FeAlSi films with excellent soft magnetic properties”, 24th International Colloquium on Magnetic Films and Surfaces, Poster1-59, Okinawa Japan, July 2022 (Poster).
4. ○**S. Akamatsu**, M. Oogane, M. Tsunoda and Y. Ando,“Characterization of the TMR properties in MTJs with FeAlSi epitaxial free layer”, 24th International Colloquium on Magnetic Films and Surfaces, Poster1-60, Okinawa Japan, July 2022 (Poster).
5. ○**S. Akamatsu**, T. Nakano, M. Tsunoda, Y. Ando and M. Oogane, “Systematic investigation of FeAlSi epitaxial films with excellent soft magnetic property”, 67th Annual Conference on Magnetism and Magnetic Materials, JOC-04, Minneapolis MN, November 2022 (Oral).
6. ○**S Akamatsu**, T Nakano, M Tsunoda, Y Ando and M Oogane, “Investigation of electronic structure of FeAlSi epitaxial films with soft magnetic property for MTJ based-sensor applications.”, 67th Annual Conference on Magnetism and Magnetic Materials, DOA-07, Minneapolis MN, November 2022 (Poster).
7. ○**S. Akamatsu**, T. Nakano, M. Tsunoda, Y. Ando , M. Oogane, “FeAlSi alloy films with ultra-soft magnetic properties for highly sensitive TMR sensors”, The 6th Symposium for the Core Research Clusters for Materials Science and Spintronics, S1 Recent progress of magnetic tunnel junction and its applications, Online, October 2022 (**Invited Talk**).
8. ○**S. Akamatsu**, B. H. Lee, Y. Hou, M. Oogane, G S. D. Beach, and J. S Moodera, “Properties of ideal soft magnetic material, FeAlSi films for ultra-sensing spintronics device application”, 68th Annual Conference on Magnetism and Magnetic Materials, JOC-04, Dallas TX, November 2023 (Oral).

Talks at Domestic Conferences or Symposiums

1. ○**赤松 昇馬**, 大兼 幹彦, 角田 匡清, 安藤 康夫, “強磁性トンネル接合磁気センサ用 FeSiAl 薄膜の作製”,第 80 回応用物理学会秋季学術講演会, 18p-PB1-64, 札幌, 9 月 2019 年(ポスター, 査読あり).
2. ○**赤松 昇馬**,大兼 幹彦,角田 匡清,安藤 康夫,“強磁性トンネル接合センサ用 FeSiAl 薄膜の作製”,第 74 回応用物理学会東北支部学術講演会,3pA08,郡山,12 月 2019 年(日本語口頭,査読あり).
3. ○**赤松 昇馬**, 大兼 幹彦, 角田 匡清, 安藤 康夫, “(001)配向 FeAlSi 電極を用いた MTJ 素子の作製”, 第 67 回応用物理学会春季学術講演会, 14p-PA1-42, 東京, 3 月 2020 年(ポスター, 査読あり).
4. ○**赤松 昇馬**,大兼 幹彦,角田 匡清, 安藤 康夫,“D03-FeAlSi エピタキシャル電極を用いた MTJ 素子の作製”,第 44 回日本磁気学会学術講演会, 15pC-8,12 月 2020 年(口頭,査読ありオンライン開催).
5. ○**赤松 昇馬**,大兼 幹彦,角田 匡清,安藤 康夫,“$D0_3$-FeAlSi 電極を用いたエピタキシャル MTJ 素子の作製”,第 75 回応用物理学会東北支部学術講演会, 3aA09, 12 月 2020 年(口頭, 査読あり, オンライン開催).
6. ○**S. Akamatsu**, T. Nakano, M. Tsunoda, M. Oogane, Y. Ando,“Fabrication of MTJs using D03-FeAlSi epitaxial film”, 第 82 回応用物理学会秋季学術講演会, 12a-S302-7, オンライン開催, 9 月 2021 年(英語口頭, 査読あり).
7. ○**S. Akamatsu**, T. Nakano, M. Tsunoda, M. Oogane, Y. Ando,“Investigation for TMR properties of MTJs using FeAlSi epitaxial films”, 第 69 回応用物理学会春季学術講演会, 25a-E201-5, 東京,3 月 2022 年(英語口頭, 査読あり).
8. ○**赤松 昇馬**,大兼 幹彦,角田 匡清, 安藤 康夫, “組成および原子規則度制御による軟磁性 FeAlSi 薄膜実現のための指針”, 第 44 回日本磁気学会学術講演会, 08pC-9,長野, 9 月 2022 年(日本語口頭, 査読あり)(**桜井講演賞**).
9. ○**S. Akamatsu**, T. Nakano, M. Tsunoda, Y. Ando, M. Oogane,“TMR properties in MTJs with epitaxial FeAlSi free layer”, 第 80 回応用物理学会秋季学術講演会, 20a-B101-5, 仙台, 9 月 2022 年(英語口頭, 査読あり).

   他：英語口頭 2 件、英語ポスター1 件、日本語口頭 1 件、日本語ポスター1 件、 (いずれも査読なし)

Patents

大兼 幹彦、**赤松 昇馬**、安藤 康夫、熊谷静似、”FeAlSi 合金薄膜および FeAlSi 合金薄膜の製造方法、ならびに、磁気センサおよび磁気センサの製造方法”、4 月 2022 年

Others

1. 「グローバル工学奨励賞 2015」 「グローバル工学奨励賞 2016」, 2016, 2017 年 4 月
2. 「平成 30 年度東北大学総長賞」 2019 年 3 月
3. 「東北大発の磁性材料“センダスト合金”, 発見から 90 年目で再び脚光～超高感度磁気センサへの応用に期待～」、東北大学プレスリリース、2022 年 6 月
4. 日本磁気学会技術情報サービス第 200 号、2022 年 8 月
5. 「東北大、センダストの軟磁気特性発現機構の謎を解明し原子規則度の制御によって広い組成範囲で軟磁気特性を実現」、日本経済新聞電子版、2022 年 6 月
6. 「日本磁気学会第 46 回学術講演会 令和 4 年度学生講演賞（桜井講演賞）」 2022 年 11 月
7. 「第 26 回応用物理研究奨励賞」 2023 年 3 月
8. 「第 36 回先端技術大賞 文部科学大臣賞（最優秀賞）」 2023 年 7 月
9. 「令和 5 年度東北大学総長賞」 2024 年 3 月

VII. References

[1] 安藤康夫, “スピントロニクス技術とデバイス開発,” 応用物理 83(3), 184–193 (2014).

[2] W. Thomson, “XIX. On the electro-dynamic qualities of metals:—Effects of magnetization on the electric conductivity of nickel and of iron,” Proc. R. Soc. Lond. 8(0), 546–550 (1857).

[3] I.A. Campbell, A. Fert, and O. Jaoul, “The spontaneous resistivity anisotropy in Ni-based alloys,” J. Phys. C: Solid State Phys. 3(1S), S95 (1970).

[4] T. McGuire, and R. Potter, “Anisotropic magnetoresistance in ferromagnetic 3d alloys,” IEEE Trans. Magn. 11(4), 1018–1038 (1975).

[5] M.N. Baibich, J.M. Broto, A. Fert, Nguyen Van Dau F, F. Petroff, P. Etienne, G. Creuzet, A. Friederich, and J. Chazelas, “Giant magnetoresistance of (001)Fe/(001)Cr magnetic superlattices,” Phys. Rev. Lett. 61(21), 2472–2475 (1988).

[6] G. Binasch, P. Grünberg, F. Saurenbach, and W. Zinn, “Enhanced magnetoresistance in layered magnetic structures with antiferromagnetic interlayer exchange,” Phys. Rev. B Condens. Matter 39(7), 4828–4830 (1989).

[7] M. Julliere, “Tunneling between ferromagnetic films,” Phys. Lett. A 54(3), 225–226 (1975).

[8] T. Miyazaki, and N. Tezuka, “Giant magnetic tunneling effect in Fe/Al_2O_3/Fe junction,” J. Magn. Magn. Mater. 139(3), L231–L234 (1995).

[9] J.S. Moodera, L.R. Kinder, T.M. Wong, and R. Meservey, “Large magnetoresistance at room temperature in ferromagnetic thin film tunnel junctions,” Phys. Rev. Lett. 74(16), 3273–3276 (1995).

[10] W.H. Butler, X.-G. Zhang, T.C. Schulthess, and J.M. MacLaren, “Spin-dependent tunneling conductance of Fe/MgO/Fe sandwiches,” Phys. Rev. B Condens. Matter 63(5), 054416 (2001).

[11] S. Yuasa, A. Fukushima, T. Nagahama, K. Ando, and Y. Suzuki, “High tunnel magnetoresistance at room temperature in fully epitaxial Fe/MgO/Fe tunnel junctions due to coherent spin-polarized tunneling,” Jpn. J. Appl. Phys. 43(4B), L588 (2004).

[12] S. Yuasa, T. Nagahama, A. Fukushima, Y. Suzuki, and K. Ando, “Giant room-temperature magnetoresistance in single-crystal Fe/MgO/Fe magnetic tunnel junctions,” Nat. Mater. 3(12), 868–871 (2004).

[13] S.S.P. Parkin, C. Kaiser, A. Panchula, P.M. Rice, B. Hughes, M. Samant, and S.-H. Yang, “Giant tunnelling magnetoresistance at room temperature with MgO (100) tunnel barriers,” Nat. Mater. 3(12), 862–867 (2004).

[14] D.D. Djayaprawira, K. Tsunekawa, M. Nagai, H. Maehara, S. Yamagata, N. Watanabe, S. Yuasa, Y. Suzuki, and K. Ando, “230% room-temperature magnetoresistance in CoFeB/ MgO/ CoFeB magnetic tunnel junctions,” Appl. Phys. Lett. 86(9), 092502 (2005).

[15] S. Yuasa, Y. Suzuki, T. Katayama, and K. Ando, “Characterization of growth and crystallization processes in CoFeB⁄MgO⁄CoFeB magnetic tunnel junction structure by reflective high-energy electron

diffraction," Appl. Phys. Lett. 87(24), 242503 (2005).
[16] S. Ikeda, J. Hayakawa, Y. Ashizawa, Y.M. Lee, K. Miura, H. Hasegawa, M. Tsunoda, F. Matsukura, and H. Ohno, "Tunnel magnetoresistance of 604% at 300 K by suppression of Ta diffusion in Co Fe B/ Mg O/ Co Fe B pseudo-spin-valves annealed at high temperature," Appl. Phys. Lett. 93(8), 082508 (2008).
[17] C. Zheng, K. Zhu, S. Cardoso de Freitas, J.-Y. Chang, J.E. Davies, P. Eames, P.P. Freitas, O. Kazakova, C. Kim, C.-W. Leung, S.-H. Liou, A. Ognev, S.N. Piramanayagam, P. Ripka, A. Samardak, K.-H. Shin, S.-Y. Tong, M.-J. Tung, S.X. Wang, S. Xue, X. Yin, and P.W.T. Pong, "Magnetoresistive Sensor Development Roadmap (Non-Recording Applications)," IEEE Trans. Magn. 55(4), 1–30 (4/2019).
[18] P.P. Freitas, R. Ferreira, and S. Cardoso, "Spintronic Sensors," Proc. IEEE Inst. Electr. Electron. Eng. 104(10), 1894–1918 (2016).
[19] 愛知製鋼, "MI sensor by 愛知製鋼," (https://www.aichi-steel.co.jp/smart/mi/mi-technology.html).
[20] 彰剛菅野, 日本生体磁気学会誌 28, 68 (2015).
[21] 好廿日出, 電子情報通信学会技術研究報告 114, 49 (2015).
[22] K. Nishi, Y. Ito, and T. Kobayashi, "High-sensitivity multi-channel probe beam detector towards MEG measurements of small animals with an optically pumped K-Rb hybrid magnetometer," Opt. Express 26(2), 1988–1996 (2018).
[23] Y. Matsuzaki, Phys. Rev. A 94, 52330 (2016).
[24] T. Takiya, and T. Uchiyama, "Development of active shielding-type MI gradiometer and application for magnetocardiography," IEEE Trans. Magn. 53(11), 1–4 (2017).
[25] H. Karo, and I. Sasada, "Magnetocardiogram measured by fundamental mode orthogonal fluxgate array," J. Appl. Phys. 117(17), (2015).
[26]"MAGNETICS business & technology," (2019 1. 22).
[27]"MULTI DIMENTION" (https://www.dowaytech.com/en/).
[28]"AKM," (https://www.akm.com/akm/jp/product/detail/0059/).
[29]"TDK," (https://product.tdk.com/ja/techlibrary/developing/bio-sensor/index.html).
[30] 久世直洋, 博士学位論文, 京都大学大学院, 2002.
[31] F. Primdahl, "The fluxgate mechanism, part I: The gating curves of parallel and orthogonal fluxgates," IEEE Trans. Magn. 6(2), 376–383 (1970).
[32] D. Gordon, and R. Brown, "Recent advances in fluxgate magnetometry," IEEE Trans. Magn. 8(1), 76–82 (1972).
[33] K. Mohri, and Y. Honkura, "Amorphous wire and CMOS IC based magneto-impedance sensors—Origin, topics, and future," Sens. Lett., (2007).
[34] K. Mohri, T. Uchiyama, L.P. Shen, C.M. Cai, L.V. Panina, Y. Honkura, and M. Yamamoto,

“Amorphous wire and CMOS IC-based sensitive micromagnetic sensors utilizing magnetoimpedance (MI) and stress-impedance (SI) effects,” IEEE Trans. Magn. 38(5), 3063–3068 (2002).

[35] T. Uchiyama, S. Nakayama, K. Mohri, and K. Bushida, “Biomagnetic field detection using very high sensitivity magnetoimpedance sensors for medical applications,” Phys. Status Solidi 206(4), 639–643 (2009).

[36] L.V. Panina, K. Mohri, T. Uchiyama, M. Noda, and K. Bushida, “Giant magneto-impedance in Co-rich amorphous wires and films,” IEEE Trans. Magn. 31(2), 1249–1260 (1995).

[37] 原宏, and 栗城真也, “脳磁気科学—SQUID 計測と医学応用,” 株式会社オーム社, 東京, (1997).

[38] 原宏編, “SQUID 計測と医学応用,” 脳磁気科学, (1997).

[39] S. Khan, and D. Cohen, “Note: Magnetic noise from the inner wall of a magnetically shielded room,” Rev. Sci. Instrum. 84(5), 056101 (2013).

[40] J.C. Allred, R.N. Lyman, T.W. Kornack, and M.V. Romalis, “High-sensitivity atomic magnetometer unaffected by spin-exchange relaxation,” Phys. Rev. Lett. 89(13), 130801 (2002).

[41] I.K. Kominis, T.W. Kornack, J.C. Allred, and M.V. Romalis, “A subfemtotesla multichannel atomic magnetometer,” Nature 422(6932), 596–599 (2003).

[42] Y. Matsuzaki, T. Shimo-Oka, H. Tanaka, Y. Tokura, K. Semba, and N. Mizuochi, “Hybrid quantum magnetic-field sensor with an electron spin and a nuclear spin in diamond,” Phys. Rev. A 94(5), 052330 (2016).

[43] W.H. Meiklejohn, and C.P. Bean, “New Magnetic Anisotropy,” Phys. Rev. 102(5), 1413–1414 (1956).

[44] 藤原耕輔, 博士学位論文, 東北大学大学院, 2013.

[45] NeurotechJP, (https://neurotechjp.com).

[46] Neuralink:Home, (https://neuralink.com/).

[47] A. Kanno, N. Nakasato, M. Oogane, K. Fujiwara, T. Nakano, T. Arimoto, H. Matsuzaki, and Y. Ando, “Scalp attached tangential magnetoencephalography using tunnel magneto-resistive sensors,” Sci. Rep. 12(1), 6106 (2022).

[48] 川西健次, 近角聰信, and 櫻井良文, “磁気工学ハンドブック,” (1998).

[49] W.F. Egelhoff Jr, V.E. Höink, J.W. Lau, W.F. Shen, B.D. Schrag, and G. Xiao, “Magnetic tunnel junctions with large tunneling magnetoresistance and small saturation fields,” J. Appl. Phys. 107(9), 09C705 (2010).

[50] K. Tsunekawa, D.D. Djayaprawira, M. Nagai, H. Maehara, S. Yamagata, and N. Watanabe, “Digest of the IEEE International Magnetics Conference,” IEEE, New York, 1223–1224 (2005).

[51] K. Fujiwara, M. Oogane, S. Yokota, T. Nishikawa, H. Naganuma, and Y. Ando, “Fabrication of magnetic tunnel junctions with a bottom synthetic antiferro-coupled free layers for high sensitive magnetic field sensor devices,” J. Appl. Phys. 111(7), 07C710 (2012).

[52] S.S.P. Parkin, “Systematic variation of the strength and oscillation period of indirect magnetic exchange coupling through the 3d, 4d, and 5d transition metals,” Phys. Rev. Lett. 67(25), 3598–3601 (1991).
[53] 大樹加藤, 幹彦大兼, 耕輔藤原, 純一城野, 博永沼, 弘之桂田, and 康夫安藤, “生体磁場センサ応用に向けた強磁性トンネル接合の作製と評価,” 生体医工学 53(Supplement), S187_02-S187_02 (2015).
[54] F. Heusler, “Über magnetische manganlegierungen,” Verh. Dtsch. Phys. Ges. 5, 219 (1903).
[55] S. Ishida, S. Fujii, S. Kashiwagi, and S. Asano, “Search for Half-Metallic Compounds in Co2MnZ (Z=IIIb, IVb, Vb Element),” J. Phys. Soc. Jpn. 64(6), 2152–2157 (1995).
[56] Y. Sakuraba, a. M. Hattori, M. Oogane, Y. Ando, H. Kato, A. Sakuma, T. Miyazaki, and H. Kubota, “Giant tunneling magnetoresistance in Co_2MnSi/ Al-O/ Co_2MnSi magnetic tunnel junctions,” Appl. Phys. Lett. 88(19), 192508 (2006).
[57] T. Marukame, T. Ishikawa, K.-I. Matsuda, T. Uemura, and M. Yamamoto, “High tunnel magnetoresistance in fully epitaxial magnetic tunnel junctions with a full-Heusler alloy $Co_2Cr_{0.6}Fe_{0.4}Al$ thin film,” Appl. Phys. Lett. 88(26), 262503 (2006).
[58] T. Kubota, S. Tsunegi, M. Oogane, S. Mizukami, T. Miyazaki, H. Naganuma, and Y. Ando, “Half-metallicity and Gilbert damping constant in $Co_2Fe_xMn_{1-x}Si$ Heusler alloys depending on the film composition,” Appl. Phys. Lett. 94(12), 122504 (2009).
[59] 佐藤丈、窪田崇秀、大兼幹彦、永沼博、安藤康夫, “低保磁力ホイスラー合金の作製,” 第70回 秋季 応用物理学会口頭発表(10p-ZE-4), (2009).
[60] 工藤奈々, 修士学位論文, 東北大学大学院工学研究科応用物理学専攻, 2020.
[61] M. Takahashi, “最近の鉄系薄膜磁気ヘッド材料—センダスト合金例として—,” Ouyou Butsuri 56(10), 1289−1306 (1987).
[62] T. Shirai, “センダストスパッタ膜積層ヘッドのコア損失” Proceedings of the National Convention of the Television Association of Japan 22, 159−160 (1986).
[63] N. Okamoto and Y. Miyoshi, “Sputterd High Bs FeA1Si films for MIG Heads,” J. Jpn. Soc. Powder Powder Metall. 40(9), 886–889 (1993).
[64] P.M. Dodd, R. Atkinson, P. Papakonstantinou, M.S. Araghi, and H.S. Gamble, “Correlation between crystalline structure and soft magnetic properties in sputtered sendust films,” Journal of Applied Physics 81(8), 4104–4106 (1997).
[65] T. Muramatsu, M. Michijima, M. Kadono, and T. Fujine, “The magnetic properties and external stress for Fe-Al-Si evaporated films,” J. Magn. Soc. Jpn. 19(5), 879–879 (1995).
[66] T. Muramatsu, and M. Kadono, “Grain diameter and coercivity of FeAlSi films,” JOURNAL-MAGNETICS SOCIETY OF JAPAN 19, 952–957 (1995).
[67] Nago K., “Structure Dependence of Magnetic Properties of Fe-Al-Si (Sendust) Alloy Films,” J. Magn. Soc. Jpn. 12(5), 597–601 (1988).

[68] H. Masumoto, T. Yamamoto,“新合金 「センダスト」 及び Fe-Si-Al 系合金の磁氣的並に電氣的性質に就て,”J. Jpn. Inst. Met. 1(3), 127−135 (1937).
[69] S. Chikazumi,“磁性体ハンドブック,”P390 (Asakura Shotenn, 1975), (1975).
[70] 達治山本,“高透磁率合金センダストの発見とその歩み,”日本応用磁気学会誌 3(3), 71−74 (1979).
[71] T. Wakiyama, M. Takahashi, S. Nishimaki, and J. Shimoda, “Magnetic properties of Fe-Si-Al single crystals,” IEEE Trans. Magn. 17(6), 3147–3150 (1981).
[72] A.S. Zaimovsky, and I.P. Selissky, “On the cause of high permeability of alloys Fe-Si-Al (Sendust),” J. Phys. 4, 563–565 (1941).
[73] M. Takahashi, S. Suwabe, T. Narita and T.Wakiyama,“Fe-Si-Al スパッタ薄膜の磁気特性,”J. Jpn. Inst. Met., (1986).
[74] Watanabe K., Shinohara T., and Sato M., “NMR Study of Sendust and Alperm,” J.Japan Inst.Metals 57(3), 320–324 (1993).
[75] D. Kato, M. Oogane, K. Fujiwara, T. Nishikawa, H. Naganuma, and Y. Ando, “Fabrication of Magnetic Tunnel Junctions with Amorphous CoFeSiB Ferromagnetic Electrode for Magnetic Field Sensor Devices,” Appl. Phys. Express 6(10), 103004 (2013).
[76] N. Kudo, M. Oogane, M. Tsunoda, and Y. Ando, “Polycrystalline $Co_2Fe_{0.4}Mn_{0.6}Si$ Heusler alloy thin films with high B2 ordering and small magnetic anisotropy for magnetic tunnel junction based sensors,” AIP Adv. 9(12), 125036 (2019).
[77] K. Kabara, M. Tsunoda, and S. Kokado, “Annealing effects on nitrogen site ordering and anisotropic magnetoresistance in pseudo-single-crystal γ′ -Fe4N films,”Appl. Phys. Express 7(6), 063003 (2014).
[78] C. Cuong, and M. Kurita, “Absorption Factor and Influence of LPA Factor on Stress and Diffraction Line Width in X-Ray Stress Measurement with and without Restriction of X-Ray Diffraction Area,” Experimental Mechanics 4(1), 37–43 (2004).
[79] R.C. Reynolds, “The Lorentz-polarization factor and preferred orientation in oriented clay aggregates,” Clays Clay Miner. 34(4), 359–367 (1986).
[80] W.F. Egelhoff, P.W.T. Pong, J. Unguris, R.D. McMichael, E.R. Nowak, A.S. Edelstein, J.E. Burnette, and G.A. Fischer, “Critical challenges for picoTesla magnetic-tunnel-junction sensors,” Sens. Actuators A Phys. 155(2), 217–225 (2009).
[81] Y. Endo, T. Sakai, T. Miyazaki, and Y. Shimada, “Effect of Film Thickness on the High Frequency Magnetic Properties of Polycrystalline Fe–Ga Films,” IEEE Trans. Magn. 53(11), 1–5 (2017).
[82] S. Iida, *Magnetic Measurement, Physical Measurement Technology No.3* (Asakura Shoten, P109, 1967).
[83] B.H. Lee, T. Fakhrul, C.A. Ross, and G.S.D. Beach, “Large Anomalous Frequency Shift in Perpendicular Standing Spin Wave Modes in BiYIG Films Induced by Thin Metallic Overlayers,”

Phys. Rev. Lett. 130(12), 126703 (2023).
[84] T. Sebastian, K. Schultheiss, B. Obry, B. Hillebrands, and H. Schultheiss, “Micro-focused Brillouin light scattering: imaging spin waves at the nanoscale,” Frontiers in Physics 3, (2015).
[85] S. Ding, A. Ross, R. Lebrun, S. Becker, K. Lee, I. Boventer, S. Das, Y. Kurokawa, S. Gupta, J. Yang, G. Jakob, and M. Kläui, “Interfacial Dzyaloshinskii-Moriya interaction and chiral magnetic textures in a ferrimagnetic insulator,” Phys. Rev. B Condens. Matter 100(10), 100406 (2019).
[86] A.J. Lee, A.S. Ahmed, J. Flores, S. Guo, B. Wang, N. Bagués, D.W. McComb, and F. Yang, “Probing the Source of the Interfacial Dzyaloshinskii-Moriya Interaction Responsible for the Topological Hall Effect in Metal$Tm_3Fe_5O_{12}$ Systems,” Phys. Rev. Lett. 124(10), 107201 (2020).
[87] L. Caretta, E. Rosenberg, F. Büttner, T. Fakhrul, P. Gargiani, M. Valvidares, Z. Chen, P. Reddy, D.A. Muller, C.A. Ross, and G.S.D. Beach, “Interfacial Dzyaloshinskii-Moriya interaction arising from rare-earth orbital magnetism in insulating magnetic oxides,” Nat. Commun. 11(1), 1090 (2020).
[88] M. Takahashi, H. Arai, T. Tanaka and T. Wakiyama,“センダスト合金単結晶の規則構造と結晶磁気異方性,”J. Jpn. Inst. Met. 10(2), 221−224 (1986).
[89] M. Takahashi, S. Suwabe, T. Narita, and T. Wakiyama, “Magnetic Properties of Fe-Si-Al Sputtered Films,” IEEE Translation Journal on Magnetics in Japan 2(10), 905–911 (1987).
[90] M. Goto, T. Kamimori,“2p-D-16 Fe-Si 合金の結晶磁気異方性,”Proceedings of the Spring Sectional Meeting 1982(3), 198 (1982).
[91] T. Kubota, J. Hamrle, Y. Sakuraba, and O. Gaier, “Structure, exchange stiffness, and magnetic anisotropy of Co2MnAlxSi1− x Heusler compounds,” Journal of Applied, (2009).
[92] M. Oogane, K. Fujiwara, A. Kanno, T. Nakano, H. Wagatsuma, T. Arimoto, S. Mizukami, S. Kumagai, H. Matsuzaki, N. Nakasato, and Y. Ando, “Sub-pT magnetic field detection by tunnel magneto-resistive sensors,” Appl. Phys. Express 14(12), 123002 (2021).
[93] E. Paz, S. Serrano-Guisan, R. Ferreira, and P.P. Freitas, “Room temperature direct detection of low frequency magnetic fields in the 100 $pT/Hz^{0.5}$ range using large arrays of magnetic tunnel junctions,” J. Appl. Phys. 115(17), 17E501 (2014).
[94] Z. Lei, S. Yan, Z. Cao, Z. Guo, P. Song, Y. Qiang, J. Wang, W. Zhao, and Q. Leng, “High TMR for both in-plane and perpendicular magnetic field justified by CoFeB free layer thickness for 3-D MTJ sensors,” AIP Adv. 9(8), 085127 (2019).
[95] E. Paz, R. Ferreira, and P.P. Freitas, “Linearization of Magnetic Sensors With a Weakly Pinned Free-Layer MTJ Stack Using a Three-Step Annealing Process,” IEEE Trans. Magn. 52(7), 1–4 (2016).
[96] X. Han, Y. Zhang, Y. Wang, L. Huang, Q. Ma, H. Liu, C. Wan, J. Feng, L. Yin, G. Yu, and Others, “High-Sensitivity Tunnel Magnetoresistance Sensors Based on Double Indirect and Direct Exchange Coupling Effect,” Chin. Physics Lett. 38(12), 128501 (2021).
[97] S. Cardoso, P.P. Freitas, C. de Jesus, P. Wei, and J.C. Soares, “Spin-tunnel-junction thermal stability and interface interdiffusion above 300 °C,” Appl. Phys. Lett. 76(5), 610–612 (2000).

[98] P.V. Paluskar, C.H. Kant, J.T. Kohlhepp, A.T. Filip, H.J.M. Swagten, B. Koopmans, and W.J.M. de Jonge, “Mn diffusion and the thermal stability of tunneling spin polarization,” J. Appl. Phys. 97(10), 10C925 (2005).
[99] I.-J. Shin, B.-C. Min, J.P. Hong, and K.-H. Shin, “Effects of Ru diffusion in exchange-biased MgO magnetic tunnel junctions prepared by in situ annealing,” Appl. Phys. Lett. 95(22), 222501 (2009).
[100] C. Heiliger, P. Zahn, and I. Mertig, “Influence of interface oxidation on the TMR ratio of Fe/MgO/Fe tunnel junctions,” J. Magn. Magn. Mater. 316(2), 478–480 (9/2007).
[101] Y.-L. Lou, Y.-M. Zhang, H. Guo, D.-Q. Xu, and Y.-M. Zhang, “Effects of Fe-oxide and Mg layer insertion on tunneling magnetoresistance properties of CoFeB/MgO/CoFeB magnetic tunnel junctions,” Chin. Physics Lett. 33(11), 118501 (2016).
[102] G.X. Miao, K.B. Chetry, A. Gupta, and W.H. Butler, “Inelastic tunneling spectroscopy of magnetic tunnel junctions based on CoFeB/MgO/CoFeB with Mg insertion layer,” Journal of Applied, (2006).
[103] M. Ležaić, P. Mavropoulos, and S. Blügel, “First-principles prediction of high Curie temperature for ferromagnetic bcc-Co and bcc-FeCo alloys and its relevance to tunneling magnetoresistance,” Appl. Phys. Lett., (2007).
[104] C.H. Shang, J. Nowak, R. Jansen, and J.S. Moodera, “Temperature dependence of magnetoresistance and surface magnetization in ferromagnetic tunnel junctions,” Phys. Rev. B Condens. Matter 58(6), R2917–R2920 (1998).
[105] R.J.M. van de Veerdonk, J.S. Moodera, and W.J.M. de Jonge, “Characterization of magnetic tunnel junctions using IETS,” J. Magn. Magn. Mater. 198–199, 152–154 (1999).
[106] J.S. Moodera, J. Nowak, and R.J.M. van de Veerdonk, “Interface Magnetism and Spin Wave Scattering in Ferromagnet-Insulator-Ferromagnet Tunnel Junctions,” Phys. Rev. Lett. 80(13), 2941–2944 (1998).
[107] W. Wang, T. Ma, and M. Yan, “Microstructure and magnetic properties of nanocrystalline Co-doped Sendust alloys prepared by melt spinning,” J. Alloys Compd. 459(1), 447–451 (2008).
[108] C. Kittel, and P. McEuen, *Introduction to Solid State Physics* (Wiley, 2018).
[109] S.G. Wang, R.C.C. Ward, G.X. Du, X.F. Han, C. Wang, and A. Kohn, “Temperature dependence of giant tunnel magnetoresistance in epitaxial Fe/MgO/Fe magnetic tunnel junctions,” Phys. Rev. B Condens. Matter 78(18), 180411 (2008).
[110] S. Tsunegi, Y. Sakuraba, M. Oogane, K. Takanashi, and Y. Ando, “Large tunnel magnetoresistance in magnetic tunnel junctions using a Co2MnSi Heusler alloy electrode and a MgO barrier,” Appl. Phys. Lett. 93(11), 112506 (2008).
[111] J. Hayakawa, S. Ikeda, Y.M. Lee, F. Matsukura, and H. Ohno, “Effect of high annealing temperature on giant tunnel magnetoresistance ratio of CoFeB/MgO/CoFeB magnetic tunnel junctions,” ArXiv [Cond-Mat.Mtrl-Sci], (2006).
[112] S. Yuasa, A. Fukushima, H. Kubota, Y. Suzuki, and K. Ando, “Giant tunneling magnetoresistance

up to 410% at room temperature in fully epitaxial Co/ MgO/ Co magnetic tunnel junctions with bcc Co (001) electrodes," Appl. Phys. Lett. 89(4), (2006).

[113] S. Zhang, P.M. Levy, A.C. Marley, and S.S.P. Parkin, "Quenching of Magnetoresistance by Hot Electrons in Magnetic Tunnel Junctions," Phys. Rev. Lett. 79(19), 3744–3747 (1997).

[114] G.X. Miao, Y.J. Park, J.S. Moodera, M. Seibt, G. Eilers, and M. Münzenberg, "Disturbance of tunneling coherence by oxygen vacancy in epitaxial Fe/MgO/Fe magnetic tunnel junctions," Phys. Rev. Lett. 100(24), 246803 (2008).

[115] V. Drewello, D. Ebke, M. Schäfers, Z. Kugler, G. Reiss, and A. Thomas, "Magnon excitation and temperature dependent transport properties in magnetic tunnel junctions with Heusler compound electrodes," J. Appl. Phys. 111(7), (2012).

[116] P.A. Thiry, M. Liehr, J.J. Pireaux, and R. Caudano, "Infrared optical constants of insulators determined by high-resolution electron-energy-loss spectroscopy," Phys. Rev. B Condens. Matter 29(8), 4824–4826 (1984).

[117] S.G. Wang, R.C.C. Ward, T. Hesjedal, X.G. Zhang, C. Wang, A. Kohn, Q.L. Ma, J. Zhang, H.F. Liu, and X.F. Han, "Interface characterization of epitaxial Fe/MgO/Fe magnetic tunnel junctions," J. Nanosci. Nanotechnol. 12(2), 1006–1023 (2012).

[118] Y. Lu, H.-X. Yang, C. Tiusan, M. Hehn, M. Chshiev, A. Duluard, B. Kierren, G. Lengaigne, D. Lacour, C. Bellouard, and F. Montaigne, "Spin-orbit coupling effect by minority interface resonance states in single-crystal magnetic tunnel junctions," Phys. Rev. B Condens. Matter 86(18), 184420 (2012).

[119] Y. Ando, J. Murai, H. Kubota, and T. Miyazaki, "Magnon-assisted inelastic excitation spectra of a ferromagnetic tunnel junction," J. Appl. Phys. 87(9), 5209–5211 (2000).

[120] S. Akamatsu, M. Oogane, M. Tsunoda, and Y. Ando, "Guidelines for attaining optimal soft magnetic properties in FeAlSi films," Appl. Phys. Lett. 120(24), 242406 (2022).

[121] T. Scheike, Q. Xiang, Z. Wen, H. Sukegawa, T. Ohkubo, K. Hono, and S. Mitani, "Exceeding 400% tunnel magnetoresistance at room temperature in epitaxial Fe/MgO/Fe(001) spin-valve-type magnetic tunnel junctions," Appl. Phys. Lett. 118(4), 042411 (2021).

[122] S. Yuasa, and D.D. Djayaprawira, "Giant tunnel magnetoresistance in magnetic tunnel junctions with a crystalline MgO (001) barrier," J. Phys. D Appl. Phys. 40(21), R337 (2007).

[123] I. Rungger, O. Mryasov, and S. Sanvito, "Resonant electronic states andI−Vcurves of Fe/MgO/Fe(100) tunnel junctions," Phys. Rev. B Condens. Matter Mater. Phys. 79(9), (2009).

[124] L. Gao, X. Jiang, S.-H. Yang, J.D. Burton, E.Y. Tsymbal, and S.S.P. Parkin, "Bias voltage dependence of tunneling anisotropic magnetoresistance in magnetic tunnel junctions with MgO and Al2O3 tunnel barriers," Phys. Rev. Lett. 99(22), 226602 (2007).

[125] A.N. Chantis, K.D. Belashchenko, E.Y. Tsymbal, and M. van Schilfgaarde, "Tunneling anisotropic magnetoresistance driven by resonant surface states: first-principles calculations on an Fe(001)

surface," Phys. Rev. Lett. 98(4), 046601 (2007).
[126] M.N. Khan, J. Henk, and P. Bruno, "Anisotropic magnetoresistance in Fe/MgO/Fe tunnel junctions," J. Phys. Condens. Matter 20(15), 155208 (2008).
[127] T. Scheike, Z. Wen, H. Sukegawa, and S. Mitani, "631% room temperature tunnel magnetoresistance with large oscillation effect in CoFe/MgO/CoFe (001) junctions," Appl. Phys. Lett., (2023).

VIII. Acknowledgement – 謝辞

本研究テーマを与えてくださり，またその遂行にあたり，懇切丁寧な御指導，御鞭撻，御討論を賜りました東北大学大学院工学研究科応用物理学専攻先端スピントロニクス医療応用工学共同研究講座　安藤康夫教授に篤く御礼申し上げます.

本研究を遂行するにあたり審査員として，また常日頃より多くのご助言，懇切丁寧なご指導を賜り，研究を進めるにあたり多大なる御協力を頂きました東北大学大学院工学研究科応用物理学専攻　大兼幹彦教授に心より感謝いたします.

本研究を遂行するにあたり，日頃より有益なご助言，ご教示を頂きました東北大学大学院工学研究科グリーン未来創造機構グリーンクロステック研究センター　角田匡清教授に心より御礼申し上げます.

本論文をまとめるにあたり，審査員としてご助言を賜りました東北大学多元物質科学研究所　岡本聡教授ならびに同大学院工学研究科応用物理学専攻の諸先生方に心より御礼申し上げます.

本研究の一環としての海外研修におきまして、指導教員として日頃から丁寧に御指導頂き、有意義な議論をさせて頂きましたマサチューセッツ工科大学 Plasma Science & Fusion Center の Jagadeesh S Moodera 教授ならびに Moodera Research Group 及び Beach Group の皆様に深く感謝致します。

本研究を遂行するにあたり、共同研究として試料の評価に関してご協力頂きました　大阪公立大学大学院工学研究科電子物理系専攻　仕幸英治教授ならびに研究グループの皆様、ケンブリッジ大学 Microelectronics Group の Chiara Ciccarelli 教授ならびに研究グループの皆様、大学院工学研究科電気エネルギーシステム専攻　遠藤恭教授に深く感謝申し上げます。

本研究を進めるにあたり，貴重なご指導を賜りました東北大学大学院工学研究科応用物理学専攻　佐久間昭正学術研究員に心より御礼申し上げます.

本研究を進めるにあたり，日頃より多くのご助言，有意義な御討論を賜りました大兼研究室中野貴文助教，金珍虎元助教，アルマダウィミフタ元助教，張超亮助教に心より御礼申し上げます.

本研究を遂行するにあたり，日頃から懇切丁寧なご助言，実験環境の整備などについてご協力頂きましたスピンセンシングファクトリー藤原耕輔統括部長に心より感謝いたします．

本研究を遂行するにあたり，実験装置等の整備につきましてご尽力を頂きました杉山和弘学術研究員に深く感謝したします．

本研究を進めるにあたり，実験装置のメンテナンスに多大なるご協力をいただきました株式会社アルバックテクノ高橋功様に深く感謝いたします．

常日頃から多くのご協力を頂き，研究生活において大変お世話になりました大兼研究室職員及び秘書の皆様，在籍する学生の皆様，また日頃から丁寧なご指導を頂いた OB，OG の皆様に深く感謝いたします．

最後に，現在まで，日常生活を含め様々な場面で支えて頂いた家族・友人の皆様に深く感謝いたします．